RHEOLOGICAL PROPERTIES, STOCHASTIC CHARACTERISTICS, AND SECOND LAW VIOLATIONS OF ATOMIC FLUIDS IN COUETTE FLOW

BY

BHARATH VENKATESH RAGHAVAN

DISSERTATION

Submitted in partial fulfillment of the requirements
for the degree of Doctor of Philosophy in Theoretical and Applied Mechanics
in the Graduate College of the
University of Illinois at Urbana-Champaign, 2020

Urbana, Illinois

Doctoral Committee:

Professor Martin Ostoja-Starzewski, Chair
Associate Professor Leonardo Patricio Chamorro Chavez
Teaching Associate Professor Leon Liebenberg
Associate Professor Andre Schleife

Abstract

Fluids treated as a discrete collection of particles rather than as a continuum, exhibit exotic properties under shear at sub-continuum scales. For instance, at a critical strain-rate the fluid becomes non-Newtonian owing to an ordering transition and the thermodynamic entropy production can be negative on small length and time scales due to the probabilistic nature of the system observables. Therefore, a complete characterization and study of fluid behavior is accomplished through the interplay between statistical and continuum mechanics. Molecular dynamics (MD) is naturally suited to provide insight into the behavior of such systems. It has been widely used to probe the behavior of a wide variety of systems on very small length and time scales. This research focuses on understanding the rheological nature, in particular, shear-thinning of atomic fluids to obtain a general constitutive relationship between shear-stress and strain-rate. We studied the statistical characteristics of the fluid properties to gain insight into the structural features that result in non-Newtonian behavior, the system's tendency to violate the second law of thermodynamics, and the latter's consequences for continuum theories.

Using non-equilibrium molecular dynamics (NEMD) simulations, we study the shear-stress under steady-state conditions and its dependency on fluid properties (temperature and density) and applied shear-strain rate. The term *strain-rate*, more common in the physics literature, is used here in place of *deformation rate*. We propose a rheological equation of state that fits observed system responses exceptionally well and captures the extreme shear-thinning effect. This model arises naturally from the Boltzmann equation and kinetic theory and gives rise to a viscosity model similar to the well-established Cross model, but absent empirical parameters. The model possesses an inherent scaling parameter that unifies the rheological properties of the Lennard-Jones (LJ) fluid.

Additionally, the probabilistic nature of the shear stress and the system's tendency to violate the second law of thermodynamics is investigated by observing negative shear-stress increments. We draw conclusions on the implications these phenomena have on continuum theories adapted to atomic fluids such as flow

stability. Building on these models, we aim to understand the transitions to turbulence and flow instability in atomic fluids. Via the Poincaré inequality, we generalize a classical continuum methodology to atomic fluids and obtain a fluid dependent lower bound on the critical Reynolds number.

To Emmaline, Sandhya, Amma, Appa, Janeen, and Bill
for their eternal love and everlasting support

Acknowledgements

This dissertation is the culmination of almost 6 years of research. As I reflect on this tremendous journey, I have realized that this work could not have been accomplished without the immense support and guidance I have received from all the people who have touched my life during my doctoral studies. For if I could, all their names would appear on the front page of this compilation (work). It is my hope that this acknowledgment suffices in articulating my eternal gratitude to them and shedding light on their significant contributions.

First and foremost, I would like to thank my PhD advisor, Dr. Martin Ostoja-Starzewski for his exceptional guidance and support. Apart from being my mentor, I consider him a great friend who stood by me in my most vulnerable of times. He enabled me to persevere through the tribulations of this journey by always being a source of timely wisdom and everlasting encouragement.

To my final defense committee members, Dr. Liebenberg, Dr. Chavez, and Dr. Schleife, I would like to extend my gratitude for their constructive comments that helped me shape my magnum opus into a final product that I can forever be proud of. I would also like to thank Kathy Smith of the MechSE department for patiently tolerating my barrage of emails and guiding me through all the necessary administrative processes. Her support was instrumental to having a seamless doctoral experience at MechSE and the U of I.

On a more personal note, this dissertation would not have manifested in the way it has had it not been for those loved ones who stood by me through thick and thin. I would like to thank my parents for their immense support and encouragement during this journey. They have always been a source of strength and fortitude during my most troubled days. To my sister, who always pulled me out of the lowest of moods and lifted my spirits with her wit and jest, I will always be indebted to you. And, to my in-laws who tolerated my often reclusive and eccentric behavior whenever I withdrew to a quiet corner of their house to meet approaching deadlines, I thank you both from the bottom of my heart for welcoming me into your home and taking pride in my undertaking.

Finally, I would like to profusely thank my wife, Emmaline, for her unwavering faith in me even when my own faltered. She is my guiding light and inspiration who always managed to keep me together and strengthen my resolve no matter the circumstance. There are no words that will do justice to the gratitude I owe her. This dissertation is as much hers as it is mine.

Table of Contents

List of Tables

List of Figures

Chapter 1
Introduction

1.1 Motivation

The surge in interest in MEMS (Micro Electro-Mechanical Systems) and NEMS (Nano Electro-Mechanical Systems) devices has correspondingly led to the widespread use of multiscale methods in the computational study of a wide variety of engineering systems. As scientists and engineers strive to miniaturize conventional machines and integrate them with novel technologies, they have come to realize that this scaling process is not straightforward. There are numerous instances in which the behavior of materials and systems in the microscale are vastly different from their conventional macroscale counterparts that obey the laws and tenets of classical continuum mechanics. Additionally, the scaling down process results in a more involved analysis since the assumptions made in classical continuum mechanical models are invalidated. As a result, a more synergistic approach utilizing tools from different realms of engineering and the physical sciences is required for analyzing small-scale systems.

This research focuses on the nature of fluids under shear – Couette flow, and their departure from continuum scale behavior. Couette flow is a widely studied and well-documented classical problem in fluid dynamics with the existence of an analytical result. The simplicity of the system makes it a suitable candidate for studying the effects of miniaturization on the bulk system response and exemplifying the differences between continuum and sub-continuum systems of similar geometries (see Fig. 1). At the molecular level classical (continuum) fluid dynamic models [i.e., the Navier-Stokes (NS) equations] often break down due to their inability to account for the discrete nature of the fluid [1] and thus its observable properties. In such cases, one should resort to molecular dynamics (MD) simulations to account for the discrete nature of the fluid and capture their microscale responses to external fields.

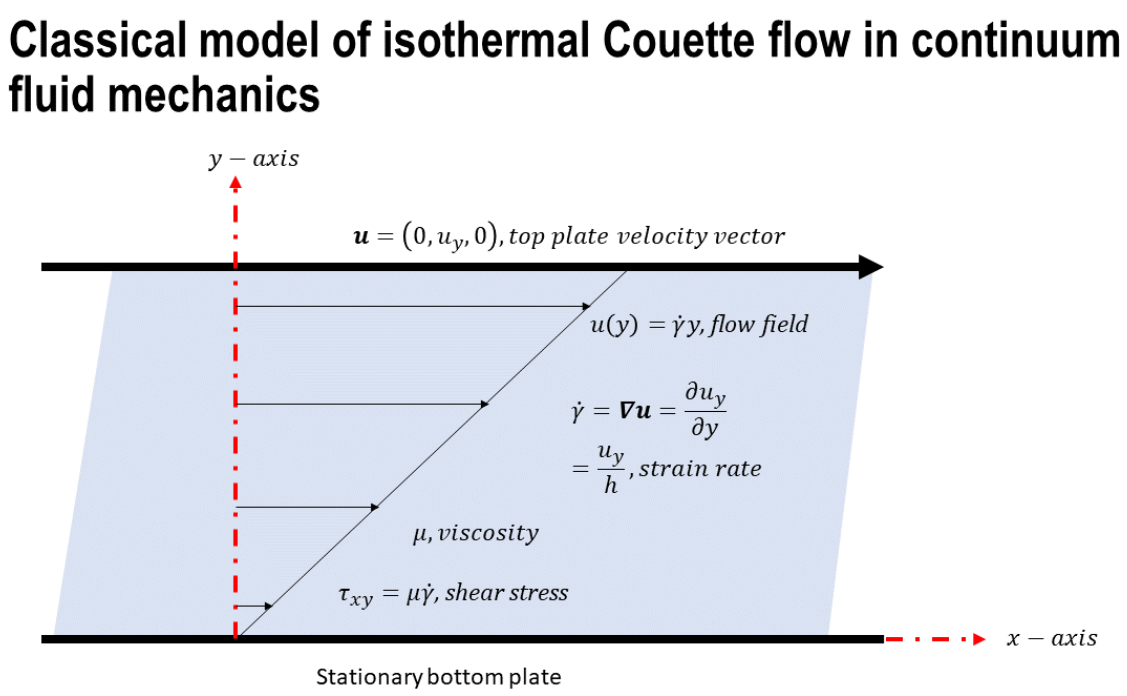

(a)

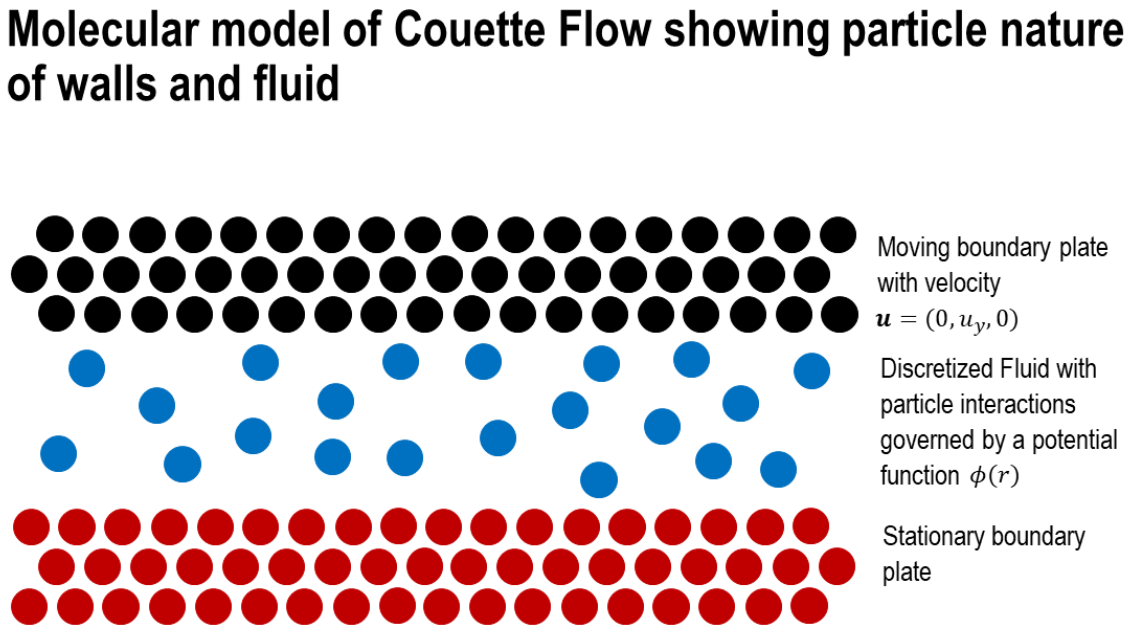

(b)

Fig. 1: (a) Continuum and (b) microscale models of Couette flow showing boundary plates and fluid as a collection of discrete particles

1.2 Background and Scope

Non-equilibrium molecular dynamics (NEMD) and in particular the SLLOD algorithm are useful techniques for studying the rheological properties of molecular fluids. Shear-thinning has been widely observed in molecular fluids under SLLOD dynamics. Ref. [2] used macro-rheological equations to model the viscosity of a Lennard-Jones (LJ) fluid undergoing SLLOD dynamics. Additionally, Ref. [3] studied the structural features of the flow that result in shear-thinning such as the shear-rigidity modulus and the structural anisotropy of the flow; the author investigated the transition from an amorphous liquid to a string phase that induces shear-thinning. This non-Newtonian behavior is counter-intuitive considering the fluid is initially homogeneous and isotropic. Further scrutiny indicates that the anisotropy usually associated with shear thinning is induced in the fluid at sufficiently large strain rates as the molecules tend to realign themselves into string-like structures [4], [5], [6], [7]. This leads to a dramatic drop in shear stress between fluid layers, subsequently resulting in a drop in viscosity. It was found that the viscosity was proportional to $\dot{\gamma}^{0.5}$ in the nonlinear regime of the flow [8], [9] and via mode-coupling analysis [10]. Additionally, experimental verification has been presented for shear-thinning in NEMD simulations where the authors fitted experimental and simulation results for the viscosity of squalane to a single Carreau equation [11].

NEMD has seen widespread applicability in determining the rheological properties of alkanes [12], [13], [14], [15], polymer melts [16], and colloidal suspensions [17]. These studies have extensively investigated the nonlinear shear-thinning regime and the structural features at the onset of shear-thinning. A framework of using Monte Carlo simulations and NEMD simulations using the SLLOD equations to study the non-Newtonian shear viscosities of simple liquids under shear has been proposed [18]. The results from Monte Carlo simulations and MD simulations are consistent. This theory was extended by removing the limitation of requiring isothermal conditions [19] and was subsequently used to extensively study the rheological properties of the LJ fluid. Applying the

generalized Boltzmann equation, a nonlinear expression for the viscosity of the LJ fluid similar to the Ree-Eyring formula, but absent empirical parameters, was derived. It was discovered that the scaled shear viscosities at various state-points collapsed onto a single curve given by this expression, alluding to the existence of a universal scaling function for all temperatures and densities [19].

The classical Navier-Stokes (NS) equations for Couette flow consider a linear dependence between shear stress and deformation rate. As a consequence, in studies covering the transition to turbulence, there are instances where transition occurs at a lower Reynolds number compared to that predicted by linear stability analyses [20]. This is believed to be due to a drop in internal friction between fluid layers that result in shear-thinning. Conversely, it has been found that the onset of turbulence can be delayed in Couette flow experiments by dissolving a small amount of polymer molecules in water without altering their Newtonian nature [21].

Shear thinning and the associated ordering in the flow direction have important consequences for flow stability. The concept of stability is important in studying the transition to turbulence. It addresses two important questions: At what critical flow rate does the flow become unstable, and what is the nature of this flow after this critical flow rate. Mathematically, answers to these problems are sought from analyses of the NS equations via linear stability analyses. However, traditional linear stability analysis as outlined above has not agreed with laboratory experiments. For Poiseuille flow, the analysis predicts [22], [23] $Re_{cr} \approx 5772$, but in the laboratory the transition to turbulence occurs around $Re_{cr} \approx 1{,}000$. For planar Couette flow, the analysis predicts [24] stability at all $Re (Re_{cr} = \infty)$ but the transition occurs in the laboratory [25], [26] around $Re_{cr} \approx 360$. The problem arises because the optimal perturbations to the steady-state flows are superpositions of perturbation eigenmodes and not a single eigenmode [27]. Consequently, nonlinear contributions may lead to transient growth in the perturbations that result in the onset of turbulence at subcritical Reynolds numbers. Under stochastic forcing of the dynamical equations, the lack of normality of the eigenmodes leads to an amplification of the variance of the perturbations despite the exponential stability

of all the normal modes. This is due to the transfer of energy from the mean flow to the perturbation flow field [28].

A ubiquitous feature at the onset of turbulence is the formation of stream-wise vortices aligned with the flow direction. The vortices do not match any single eigenmode derived from the linearized NS equation; however, they do match the optimal perturbations composed of a superposition of eigenmodes which generate the largest growth in the kinetic energy density of perturbations [28], [29], [30]. In contrast to Squire's theorem [31], these vortices are three-dimensional perturbations. It would be prudent to study the nature of these perturbations and the nonlinear contributions that lead to the subcritical onset of turbulence in simple atomic fluids under shear.

Simple atomic fluids have been studied using non-equilibrium molecular dynamics (NEMD). These simulations typically use SLLOD dynamics where fictitious forces are added to the equations of motion [8] along with Lees–Edwards boundary conditions [32] to generate the desired shear gradient. In an early study of the stability of simple atomic fluids, Loose and Hess [33], [34] formulated a stability theory to predict the critical shear rate at which steady-state planar Couette flow of an amorphous (no long-range spatial order) atomic fluid ceases to be stable. This theory is similar to the traditional linear stability analysis of the NS equation except that the linear constitutive thermodynamic relationship between the pressure and strain rate tensors is no longer assumed to be true. This critical strain-rate is characterized by the onset of shear-thinning and the strain-rate dependent structural re-ordering of fluid particles in the direction of the flow (i.e. the 'string'-phase). In this regime, steady-state Couette flow of an amorphous fluid is no longer possible. It is instead now accompanied by a reduction in viscosity and a change in the slope of the stress-deformation rate response [35]. With modern advances in simulation capabilities and algorithms such as MD, instability and transition phenomena are being studied on increasingly smaller length and timescales, such as to simulate the Rayleigh-Taylor instability in nanoscale systems [36], near-wall turbulence in Couette flow [37], and diffusion in microgravity [38].

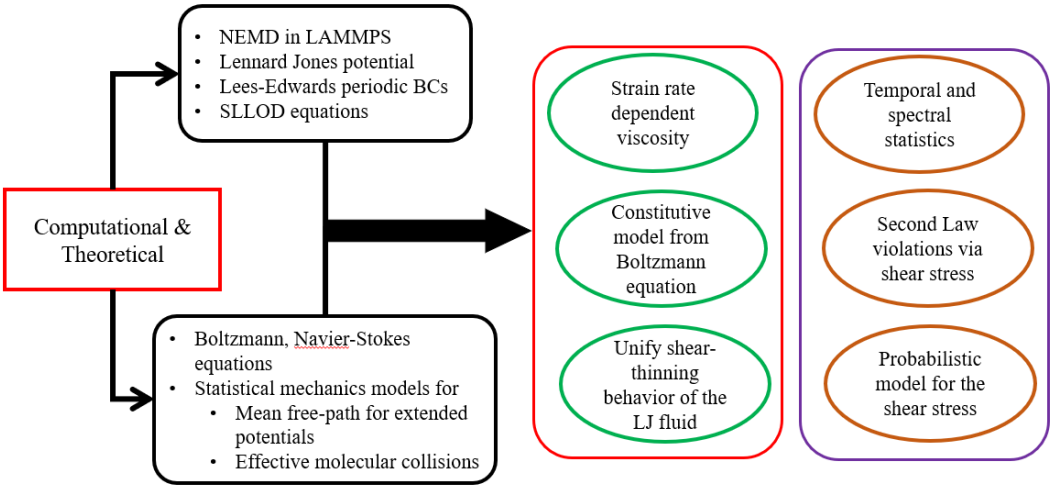

Fig. 2: Research methodology illustrating the analytical and computational methods employed in this research

Interestingly, from a thermodynamic perspective, such systems have also been observed to violate the second law of thermodynamics, which only holds true in the long-time limit, or large volume limit, or in a statistically average sense [39], [40]. In contradistinction to deterministic continuum mechanics, in sub-continuum systems, owing to the probabilistic nature of the shear stress, there is a finite probability of negative shear stress increments which signify negative entropy production. For these reasons, it is useful to understand and capture the temporal and structural mechanisms that lead to this observed behavior. Such models would be beneficial as inputs for more advanced fluid dynamics simulations.

It will be shown that shear stress plays a central role in the stability of atomic fluids under shear. It is the stochastic forcing term in the dynamical equation for the kinetic energy of perturbations [41], and arises naturally from the fluctuation theorem (FT) [40] and the dissipation function [40], [42]. The latter is a central concept in microscale theories and continuum thermomechanics and facilitates unifying phenomena in these two distinct length scales [43]. The FT explicitly allows for stochastic fluctuations in the shear stress that allow for instantaneous violations [39], [44], [45], [46], [47] of the classical Clausius-Duhem inequality of entropy production in the very small-scale limit. It demonstrates that despite the exponential stability of the perturbations, the stochastic contribution from the

shear-stress can contribute to subcritical transient amplification of their kinetic energy.

1.3 Research Methodology

In order to obtain suitable insight into sub-continuum fluid behavior, we employ a combination of analytical and computational tools. The research methodology is summarized in the schematic in Fig. 2. Throughout the development of the ideas in this dissertation, we make all the assumptions of Couette flow analogous to those made in the classical continuum analysis of the system. To obtain a microscopic flow-field consistent with macroscopic observations of Couette flow we implement the SLLOD algorithm with Lees-Edwards periodic boundary conditions. The entire simulation is carried out in LAMMPS (Large-scale Atomic/Molecular Massively Parallel Simulator) [53].

1.4 Research Objectives

The purpose of this dissertation is to outline methods for investigating the rheological (i.e. non-Newtonian) and stochastic (random) fluctuations that arise in sub-continuum shear flows despite the fluid being homogeneous and isotropic. We implement NEMD (non-equilibrium molecular dynamics) simulations using the DOLLS tensor Hamiltonian and Lees-Edwards periodic boundary conditions (explained in detail in Chapter 2) to derive insights regarding the fluid's shear flow response. The themes being studied in this dissertation fall into three categories:

1. *Fluid properties:* An interesting phenomenon of sub-continuum flows simulated via NEMD is the fluid's non-Newtonian response under shear. Our goal is to investigate the shear stress response and mathematically formulate the fluid's viscosity by reconciling simulated observations with statistical mechanics theory.
2. *Stochastic Fluctuations:* Treating the fluid as a discrete collection of particles, governed by the Lennard-Jones interaction potential (further details provided in Chapter 2), inherently results in random fluctuations

superimposed on the bulk flow trajectory. We investigate the nature of these fluctuations and characterize their statistical properties. We study their effects on fluid structure and discuss the statistical features that arise during a transition from the Newtonian to non-Newtonian flow regimes.

3. *Flow Stability:* Stability analysis is a critical tool in understanding flow response to perturbations and transitions from laminar flow to turbulence. We extend the classical notion of stability to microscopic flows by reconciling continuum (i.e. the Navier-Stokes Equations) and statistical physics theories. We derive an analogous Reynolds-Orr equation for microscale flows to quantify the critical Reynold's number at which flow instability sets in, that manifest as a structural transformation in the fluid.

1.5 Dissertation Organization

This dissertation is organized into six chapters. Chapter 2 describes the computational model and its implementation. First, we provide an overview of the atomic interaction potential and the governing dynamics. We describe the boundary conditions and the structure of the simulation domain. Finally, we describe the appropriate modifications necessary to the fundamental dynamics based on the simulation conditions.

Chapter 3 describes the mathematical basis and computational observations confirming the non-Newtonian nature of the Lennard-Jones fluid. We study the shear-stress under steady-state conditions and its dependency on fluid density and applied shear-strain rate. Via the Boltzmann equation, a strain-rate dependent model for the shear stress that accurately captures the stress-deformation response of the fluid for the range of strain-rates under consideration is derived. Additionally, we obtain a model for the viscosity naturally from the constitutive relation for the shear stress, which is absent in empirical parameters. The model for the viscosity also possesses a scaling property that facilitates unifying the response of the LJ fluid across a range of state-points.

Chapter 4 delves into the stochastic characteristics of the LJ fluid and its tendency to violate the second law of thermodynamics. In particular, we pay close

attention to shear stress. We draw a connection between local density contrast and temporal fluctuations in shear stress, which arise naturally through the equivalence between the dissipation function and entropy production according to the fluctuation theorem. We focus on the shear stress and the spatio-temporal density fluctuations and study the autocorrelations and spectral densities of the shear stress. The bispectral density of the shear stress is used to measure the degree of departure from a Gaussian model and the degree of nonlinearity induced in the system owing to the applied strain rate. More evidence is provided by the probability density function of the shear stress. We use the information theory to account for the departure from Gaussian statistics and to develop a more general probability distribution function that captures this broad range of effects. By accounting for negative shear stress increments, we show how this distribution preserves the violations of the second law of thermodynamics observed in planar Couette flow of atomic fluids, and also how it captures the non-Gaussian nature of the system by allowing for non-zero higher moments. We also demonstrate how the temperature affects the band-width of the shear-stress and how the density affects its power spectral density, thus determining the conditions under which the shear-stress acts as a narrow-band or wide-band random process. We show that changes in the statistical characteristics of the parameters of interest occur at a critical strain rate at which an ordering transition occurs in the fluid causing shear thinning and affecting its stability. A critical strain rate of this kind is also predicted by the Loose-Hess stability criterion.

Building on the results of Chapters 3 and 4, Chapter 5 investigates the stability of the LJ fluid. The stability of fluid flow is an important concept that aids in the study of transition regimes. One such mechanism to study flow stability is via the Poincaré inequality which, for deterministic continuum systems, is used to arrive at a stability criterion by providing an upper bound on the exponential decay of perturbations. However, at sub-continuum scales fluids under shear no longer behave in a manner consistent with the postulates of conventional continuum mechanics. Along with velocity perturbations, density perturbations are another factor which govern the subcritical transitions to turbulence. Specifically, under

stochastic forcing, these subcritical transitions are caused by energy transfer from the mean flow field to the perturbation field. Using the fluctuation theorem (FT) and the dissipation function, we generalize this classical continuum concept to sheared atomic fluids by ascribing a natural description to the nature of stochastic perturbations, i.e. fluctuations in shear stress, thus providing a reconciliation of kinetic theory and the Navier-Stokes (NS) equations. We obtain a fluid dependent estimate for the critical Reynolds number, investigate the nature of these disturbances and conditions necessary for the onset of turbulence at subcritical Reynolds numbers, and provide a framework by which one may generalize classical continuum theories to the microscale.

The key results are summarized and concluding remarks made along with a brief discussion of future work directions in Chapter 6.

Chapter 2

Computational Model

The goal in selecting the appropriate computational model is to obtain a microscopic description of Couette flow that is consistent with the isothermal continuum model. This necessitates preserving the linear velocity profile characteristic of Couette flow in continuum fluid dynamics when simulating its atomic counterpart. The NEMD (non-equilibrium molecular dynamics) model implemented in this dissertation satisfies those specific needs by utilizing the appropriate governing dynamics, boundary conditions, and thermostatting mechanism to preserve the linear velocity profile and institute isothermal conditions. We describe the exact methodology in greater detail below.

2.1 NEMD Simulation Methodology

The problem with simulating homogeneous flows driven by boundaries in real physical systems (e.g., Couette or elongational flows) is that a microscopic simulation explicitly including the walls invariably induces density inhomogeneities into the fluid [48]. This profound shortcoming gave rise to NEMD, which currently is well established as an accurate method for simulating homogeneous shear flows. Two well-known algorithms in this category are the DOLLS and SLLOD algorithms. These produce a microscopic description consistent with macroscopic observations. The first of the homogeneous NEMD algorithms was based on the DOLLS Hamiltonian proposed in [49]

$$H_{dolls}(\boldsymbol{r}^N, \boldsymbol{p}^N, t) = \phi(\boldsymbol{r}^N) + \sum_i \frac{\boldsymbol{p}_i^2}{2m_i} + \sum_i \boldsymbol{r}_i . \nabla \boldsymbol{u} . \boldsymbol{p}_i \Theta(t) \qquad (2.1)$$

where $\phi(r)$ is the system potential energy due to pair-wise interactions between N atoms, $\boldsymbol{r}_i$ and $\boldsymbol{p}_i$ are the laboratory position and momentum of atom i, m_i is the mass of atom i, $\nabla \boldsymbol{u}$ is the gradient of the streaming velocity $\boldsymbol{u}$ of the fluid. Furthermore, we enforce the condition that the flow begins at $t = 0$ as indicated by

$\Theta(t)$ which is the Heaviside step function. This Hamiltonian generates the DOLLS equations of motion

$$\dot{\boldsymbol{r}}_i = \frac{\boldsymbol{p}_i}{m_i} + \boldsymbol{r}_i.\nabla\boldsymbol{u} \tag{2.2a}$$

$$\dot{\boldsymbol{p}}_i = \boldsymbol{F}_i^{\phi} - \nabla\boldsymbol{u}.\boldsymbol{p}_i \tag{2.2b}$$

where $\mathbf{F}_i^{\phi}$ is the interatomic force on atom i due to all the other atoms. However, a modification proposed in [50], [51], and [52] to account for linear and nonlinear system responses is given by [48]

$$\dot{\boldsymbol{r}}_i = \frac{\boldsymbol{p}_i}{m_i} + \boldsymbol{r}_i.\nabla\boldsymbol{u} \tag{2.3a}$$

$$\dot{\boldsymbol{p}}_i = \boldsymbol{F}_i^{\phi} - \boldsymbol{p}_i.\nabla\boldsymbol{u} \tag{2.3b}$$

which are the so-called SLLOD equations of motion to indicate the transpose $\nabla\boldsymbol{u}.\boldsymbol{p}_i \rightarrow \boldsymbol{p}_i.\nabla\boldsymbol{u}$. In addition, it should be noted that the SLLOD equations cannot be derived from a system Hamiltonian.

To obtain an exact representation of planar Couette flow (i.e. to obtain a microscale Couette flow profile consistent with the continuum model), we apply the Lees-Edwards periodic boundary conditions [32], [10] by inducing a streaming velocity field of the form

$$\boldsymbol{u}(\boldsymbol{r},t) = D_{ij}x_j = \boldsymbol{i}\dot{\gamma}y \Rightarrow u(\boldsymbol{r},t) = (v_x \quad v_y \quad v_z) = (\dot{\gamma}y \quad 0 \quad 0) \tag{2.4}$$

where $\boldsymbol{i}$ is the unit vector, y is the channel height, and $\dot{\gamma} = \partial u_x/\partial y$ is the strain rate such that,

$$\nabla\boldsymbol{u}(\boldsymbol{r},t) = D_{ij} = \begin{pmatrix} 0 & 0 & 0 \\ \dot{\gamma} & 0 & 0 \\ 0 & 0 & 0 \end{pmatrix}. \tag{2.5}$$

Then, the SLLOD equations are expressed as,

$$\dot{\boldsymbol{r}}_i = \frac{\boldsymbol{p}_i}{m_i} + \boldsymbol{i}\dot{\gamma}y_i \tag{2.6a}$$

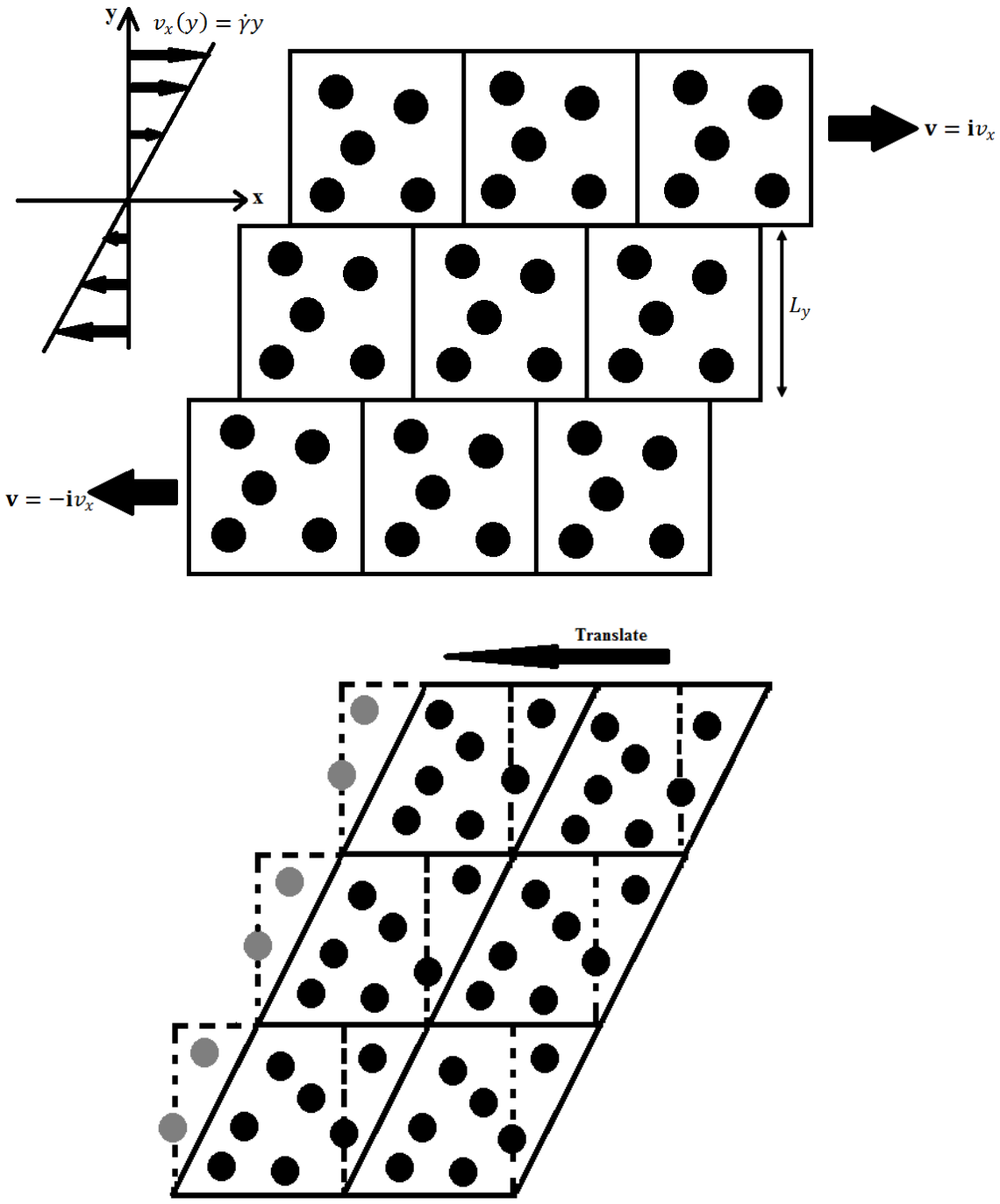

Fig. 3: Sliding brick (top) and deforming cube (bottom) representations of the Lees-Edwards periodic BCs used in NEMD simulations of atomic fluids undergoing Couette flow. The simulation domain is the center cell in the left figure with origin at the bottom left hand corner.

$$\dot{\boldsymbol{p}}_i = \boldsymbol{F}_i^{\phi} - \boldsymbol{i}\dot{\gamma} p_{yi}. \tag{2.6b}$$

In this study, the fluid undergoes SLLOD dynamics, which has been widely used and extensively documented in the literature. A schematic of the simulation methodology is shown in Fig. 3.

2.2 Lennard-Jones Fluid Model and Implementation

The molecular dynamics simulations are carried out in two-dimensions in LAMMPS [53] with particles interacting via the Lennard-Jones (LJ) potential, where the interaction is given by

$$\phi(r) = \begin{cases} 4\epsilon \left[\left(\frac{\sigma}{r}\right)^{12} - \left(\frac{\sigma}{r}\right)^{6} \right], r < r_c \\ 0, \quad r > r_c \end{cases} \tag{2.7}$$

Here ϵ is the depth of the potential well, and σ is the finite distance at which the inter-particle potential is zero. The dynamics of the simulation is governed by the SLLOD equations with Lees-Edwards periodic boundary conditions [32], [10]. To induce isothermal conditions, a Nose-Hoover thermostat in the canonical ensemble (NVT) is implemented, to yield the modified set of SLLOD equations as [9], [54]

$$\dot{\boldsymbol{r}}_i = \frac{\boldsymbol{p}_i}{m_i} + \boldsymbol{i}\gamma y_i \tag{2.8a}$$

$$\dot{\boldsymbol{p}}_i = \boldsymbol{F}_i^{\phi} - \boldsymbol{i}\gamma p_{yi} - \alpha \boldsymbol{p}_i \tag{2.8b}$$

$$\dot{\alpha} = \frac{1}{Q}\left[\frac{T(t)}{T_0} - 1\right] \tag{2.8c}$$

where α is the thermostatting multiplier, $T(t)$ is the actual kinetic temperature at time t, T_0 is the preset kinetic temperature, and Q is a constant. The equilibrium distribution function for the Nose-Hoover thermostat in the canonical ensemble is given by [10]

$$f_c(\mathbf{\Gamma}, \zeta) = \frac{\exp\left[-\beta\left(H_0 + \frac{1}{2}Q\zeta^2\right)\right]}{\int d\mathbf{\Gamma} d\zeta \exp\left[-\beta\left(H_0 + \frac{1}{2}Q\zeta^2\right)\right]} \tag{2.9}$$

Simulations are carried out for a system size of $N = 200$ molecules, in a channel of height $h^* = h/\sigma = 10$, at the state points given by $(\rho^*, T^*) = (0.6, 1.0), (0.6, 1.5), (0.8, 1.0), (0.8,1.1)$, and $(0.8442, 0.722)$, and strain rates $\left(0.0 \leq \dot{\gamma}^* = \dot{\gamma}\sigma\sqrt{m/\epsilon} \leq 2.5,\ \Delta\dot{\gamma}^* = 0.5\right)$ (in LJ reduced units), and a cutoff radius of $r_c = 2^{1/6}$. The system is run for a total of 2.6×10^7 time steps with $\Delta t^* = 0.001$ (where $t^* = t\sqrt{\epsilon\sigma^2/m}$); it is sufficiently equilibrated for 1.5×10^6 time-steps and then run for 2.45×10^7 time-steps for data extraction.

The data acquisition is unique to the distinct themes of investigation and their stated objectives and thus are explicitly described in their respective chapters (i.e. Chapters 3, 4, and 5). However, the central variable to the entire dissertation is the shear stress, which is consistently referred to and leveraged in the upcoming chapters. In these subsequent chapters, we will demonstrate how NEMD serves as a useful tool for drawing crucial insights regarding the flow dynamics and properties of sub-continuum Couette flow.

Chapter 3
Shear Thinning of Molecular Fluids Couette Flow

3.1 Introduction[1]

The Navier-Stokes (NS) equations for Couette flow consider a linear dependence between shear stress and deformation rate. However, it has been widely observed in NEMD simulations that homogeneous and isotropic fluids develop internal structure and begin shear thinning. A framework of using Monte-Carlo simulations and NEMD simulations using the SLLOD equations to study the non-Newtonian shear viscosities of simple liquids under shear has been proposed [18]. These results from Monte-Carlo simulations and MD simulations compare excellently. This theory was extended by removing the limitation of requiring isothermal conditions [19], and was subsequently used to extensively study the rheological properties of the LJ fluid. Applying the Generalized Boltzmann equation, a nonlinear expression for the viscosity of the LJ fluid similar to the Ree-Eyring formula, but absent empirical parameters, was derived. It was discovered that the scaled shear-viscosities at various state-points collapsed onto a single curve given by this expression, alluding to the existence of a universal scaling function for all temperatures and densities [19].

The purpose of this chapter is to establish a mathematical basis for the non-Newtonian behavior of the fluid. We use statistical mechanics and kinetic theory to obtain a constitutive relation for the shear stress and a viscosity model that depend on fluid properties and are absent empirical parameters. We demonstrate the versatility of our models by comparing them with others in the literature. It is shown that our models retain accuracy over a wide range of strain rates compared to selected benchmark models.

[1] Adapted from: B. V. Raghavan and M. Ostoja-Starzewski, "Shear-thinning of molecular fluids in Couette flow," *Physics of Fluids*, vol. 29, no. 2, p. 023103, 2017.

3.2 Constitutive Model Based on Kinetic Theory

We now employ the Boltzmann equation for the flows under investigation. The general expression for this equation is

$$\frac{\partial f}{\partial t} + \mathbf{v}.\nabla f + \frac{F}{m}\frac{\partial f}{\partial \mathbf{v}} = J[f,f] \tag{3.1}$$

where f is the distribution function, $\mathbf{v}$ is the velocity, F is the external force, m is the mass, and $J[f,f]$ is the collision operator [55]. For simplicity, we consider the BGK (Bhatnagar–Gross–Krook) model [56] of the form

$$\frac{\partial f}{\partial t} + \mathbf{v}.\nabla f + \frac{F}{m}\frac{\partial f}{\partial \mathbf{v}} = -\nu(f - f_L) \tag{3.2}$$

where f_L is a local equilibrium distribution function, and ν is an effective collision parameter. The BGK approximation introduces the parameter ν to render Eq. (3.1) more tractable.

Under isothermal uniform shear flow conditions, we have

$$\begin{gathered} u_i(\boldsymbol{r}) = d_{ij} r_j \\ \mathbf{d} = d_{ij} = \nabla_j u_i = \dot{\gamma}\delta_{ix}\delta_{jy} \\ \nabla T = 0 \end{gathered} \tag{3.3}$$

In order to analyze SLLOD dynamics under Lees-Edwards periodic BCs using the Boltzmann equation, we use a Galilean transformation to transition to the local rest frame (Lagrangian frame) of the fluid. Consequently, we introduce the peculiar velocity $\mathbf{V} = \mathbf{v} - \mathbf{u}(\mathbf{r})$ (i.e. in a Lagrangian frame of reference), and $\tilde{\mathbf{r}} = \mathbf{r} - \mathbf{u}t$. In the local rest frame,

$$f(\mathbf{r},\mathbf{v},\mathrm{t}) = f(\mathbf{V},t) \tag{3.4}$$

Using Eq. (3.3) in the BGK approximation in Eq. (3.2) and noting that the external thermostatting force is of the form $F = -m\alpha\mathbf{V}$, where α is the thermostatting multiplier related to the heating rate, we obtain

$$\frac{\partial f}{\partial t} + \mathbf{v}.\left[\frac{\partial f}{\partial \tilde{\mathbf{r}}}\frac{\partial \tilde{\mathbf{r}}}{\partial \mathbf{r}} + \frac{\partial f}{\partial \mathbf{V}}\frac{\partial \mathbf{V}}{\partial \mathbf{r}}\right] - \alpha \mathbf{V}\frac{\partial f}{\partial \mathbf{V}}\frac{\partial \mathbf{V}}{\partial \mathbf{v}} = -\nu(f - f_L) \tag{3.5}$$

which upon simplification yields

$$\frac{\partial f}{\partial t} + (\mathbf{I} - \mathbf{d}t)\mathbf{V}\frac{\partial f}{\partial \tilde{\mathbf{r}}} - \mathbf{dV}\frac{\partial f}{\partial \mathbf{V}} - \alpha \mathbf{V}\frac{\partial f}{\partial \mathbf{V}} = -\nu(f - f_L) \tag{3.6}$$

Under the condition of statistical spatial homogeneity, we can neglect the second term in Eq. (3.6) to obtain

$$\begin{aligned} \frac{\partial f}{\partial t} - [\mathbf{dV} + \alpha \mathbf{V}]\frac{\partial f}{\partial \mathbf{V}} &= -\nu(f - f_L) \\ \frac{\partial f}{\partial t} - \left[d_{ij}V_j + \alpha V_i\right]\frac{\partial f}{\partial V_i} &= -\nu(f - f_L) \end{aligned} \tag{3.7}$$

At this point, we note that the pressure tensor is the second moment of the peculiar velocity and is expressed as

$$\mathbf{P} := m\int \mathbf{V} \otimes \mathbf{V}\, f(\mathbf{V}, t)d\mathbf{V} \tag{3.8}$$

where $\otimes$ denotes the vector outer product. Multiplying Eq. (3.7) by V_iV_j and integrating yields

$$\frac{\partial P_{ij}}{\partial t} + d_{ik}P_{jk} + d_{jk}P_{ik} + 2\alpha P_{ij} = -\nu(P_{ij} - p\delta_{ij}) \tag{3.9}$$

Expanding Eq. (3.9), bearing in mind the following

- $P_{33} = P_{31} = P_{32} = 0$ in planar Couette flow,
- $p = \frac{P_{11}+P_{22}+P_{33}}{3} = \frac{1}{3}tr(\mathbf{P})$,
- All time derivatives vanish under steady-state conditions,

we replace $P_{11} = p$ to obtain the following set of coupled differential equations governing the time-evolution of the pressure tensor as

$$\frac{\partial p}{\partial t} + \frac{2}{3}\dot{\gamma} P_{12} + 2\alpha p = 0 \tag{3.10a}$$

$$\frac{\partial P_{22}}{\partial t} + 2\alpha P_{22} + \nu P_{22} = -\nu p \tag{3.10b}$$

$$\frac{\partial P_{12}}{\partial t} + \dot{\gamma} P_{22} + 2\alpha P_{12} = -\nu P_{12} \tag{3.10c}$$

Neglecting time derivatives, and solving Eq. (3.10c) yields

$$P_{12} = -\frac{\dot{\gamma}\frac{P_{22}}{\nu}}{1 + \frac{2}{\nu}\alpha} \tag{3.11}$$

In addition, Eq. (3.10a) yields the thermostatting multiplier as

$$\alpha = -\frac{\dot{\gamma} P_{12}}{3p} \tag{3.12}$$

Substituting Eq. (3.12) in Eq. (3.11) and noting the BGK approximation that $\nu = p/\eta_0$, where η_0 is the Newtonian viscosity of the fluid, and that under steady-state conditions $P_{22} = p$, we have

$$P_{12} = -\frac{\eta_0 \dot{\gamma}}{1 + \frac{2}{\nu}\left[\frac{-\dot{\gamma} P_{12}}{3p}\right]} \tag{3.13}$$

Substituting $P_{12} = -\eta_0 \dot{\gamma}$ in Eq. (3.13) and noting that $P_{12} = -\tau_{12}$ yields

$$\tau_{12} = \frac{\eta_0 \dot{\gamma}}{1 + \frac{2}{3\nu^2}\dot{\gamma}^2} \tag{3.14}$$

where τ_{12} is the shear stress (which is the negative of the shear component of the pressure tensor).

To find a suitable expression for the effective collision constant ν in terms of the reduced LJ parameters (i.e. the temperature T^*, density ρ^*, molecular mass m, and Newtonian viscosity η_0^*), we know that [57]

$$\nu = \frac{1}{\lambda}\left(\frac{8k_BT}{\pi m}\right)^{\frac{1}{2}} \tag{3.15}$$

where λ is the molecular mean free path. The mean free path for extended potentials is defined as [58], [59]

$$\lambda = \frac{\eta_0}{\rho}\left(\frac{\pi m}{2k_BT}\right)^{\frac{1}{2}} \tag{3.16}$$

Substituting Eq. (3.16) in Eq. (3.15) and converting to reduced LJ units [19], we have

$$\nu^* = \nu\sigma(m/\epsilon)^{1/2} = \frac{4\rho^*T^*}{\pi\eta_0^* m} \tag{3.17}$$

Thus, in reduced LJ units, the shear thinning equation of state is

$$\tau_{12}^* = \tau_{12}(\sigma^3/\epsilon) = \frac{\eta_0^*\dot{\gamma}^*}{1+\frac{2}{3}(\dot{\gamma}^*/\nu^*)^2} \tag{3.18}$$

3.3 Results

The data of primary relevance in this study are the mean values of the steady-state shear stress (i.e. the negative of the shear component of the pressure tensor, the latter being the default output in LAMMPS). After the initial equilibration period, we extract mean values for 2.45×10^7 time-steps at $\Delta t^* = 0.001$ increments. We divided the total simulation into blocks of $M = 1000$ time-steps which yields a total number of $N = 24500$ blocks. For each block, we calculate the section average which uses the 1000 data points associated with that block given by

$$\langle P_{12}(\dot{\gamma})\rangle_B = \sum_{i=1}^{M} P_{12}^{(i)} \tag{3.19}$$

and the cumulative average which accounts for all the previous section averages expressed as

$$\langle P_{12}(\dot{\gamma})\rangle_C = \sum_{i=1}^{N} \langle P_{12}(\dot{\gamma})\rangle_B^{(i)} \tag{3.20}$$

The steady-state is achieved when fluctuations in the cumulative average are no longer statistically significant.

3.3.1 Comparison of Numerical and Analytical Results

Table 1: LJ state points and parameter estimates in Eq. (3.18) obtained via curve fitting.

$\boldsymbol{\rho^*}$	$\boldsymbol{T^*}$	$\boldsymbol{\eta_0^*}$	$\boldsymbol{2/3\nu^{*2}}$
0.4	1.5	0.49	0.070
0.6	1.0	0.85	0.050
0.6	1.5	0.98	0.038
0.8	1.0	2.92	0.32
0.8	1.1	2.97	0.29
0.8442	0.722	3.76	0.62
0.9	1.1	5.39	0.42

Consistent with well-established observations made in the literature, the LJ fluid exhibits shear-thinning, the degree of which depends on the fluid state point as illustrated in Fig. 4. At low densities, the fluid only experiences moderate shear-thinning [Fig. 4 *(top)*] for the range of strain-rates considered. With increasing density, the fluid exhibits extreme shear-thinning as shown by its stress-deformation response in Fig. 4 *(bottom)*. The level of shear-thinning tends to set in quicker as the fluid density increases. For instance, extreme shear-thinning occurs at $\dot{\gamma} \geq 1.0$ at the triple point (i.e. $\rho^* = 0.8442$ and $T^* = 0.722$), but only at $\dot{\gamma} \geq 1.5$ for $\rho^* = 0.8$ and $T^* = 1.0$. Furthermore, an increase in temperature tends to delay the onset of extreme shear-thinning. Comparing two state points at $\rho^* = 0.8$ and $T^* = 1.0$ and $\rho^* = 0.8$ and $T^* = 1.1$, the latter requires a strain rate of $\dot{\gamma} \geq 2.0$

compared to $\dot{\gamma} \geq 1.5$ for the former. In either case, we see that Eq. (3.18) is able to capture the stress-deformation response extremely well.

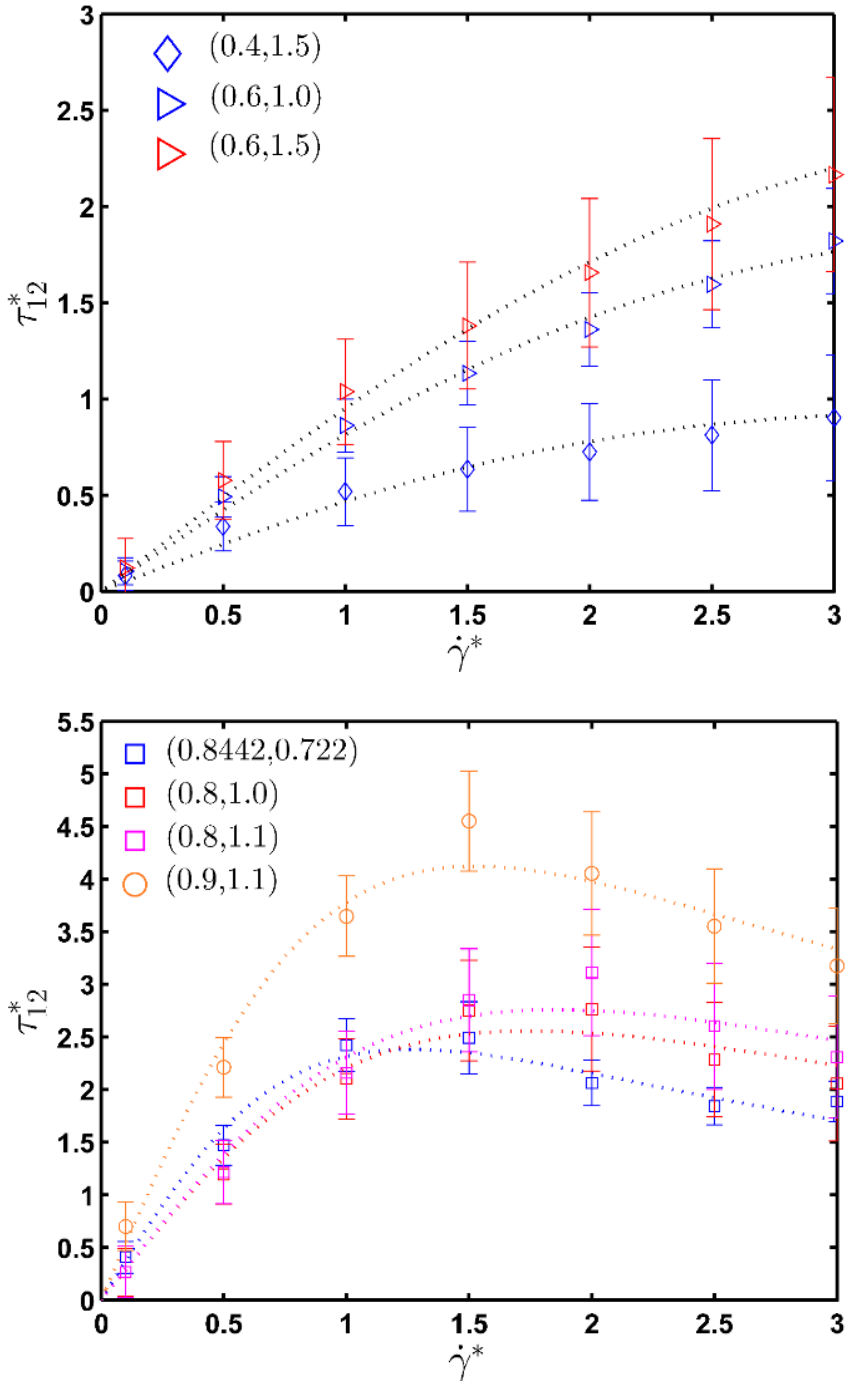

Fig. 4: Moderate *(top)* and extreme *(bottom)* shear-thinning in the stress-deformation curve for the LJ fluid at various state points. The curve-fit is performed using Eq. (3.18) and is represented by the dotted lines.

3.3.2 Model Effectiveness and Molecular Model for Viscosity

To evaluate the effectiveness of the proposed constitutive model, we compare it with widely used empirical formulae available in the literature and its goodness-of-fit measured by the r^2-value. The models of interest are as follows:

1. The Sisko equation: $\tau_{12} = k\dot{\gamma}^n + \eta_\infty \dot{\gamma}$
2. The Ree-Eyring equation: $\tau_{12} = \frac{k_b T}{V_\sigma} \sinh^{-1}(\dot{\gamma}\tilde{\tau})$ where k_b is the Boltzmann constant, T is the temperature, $\tilde{\tau}$ is the relaxation time, and V_σ is the shear stress activation volume.
3. The Bair-Winer equation: $\tau_{12} = \tau_{12}^L \left(1 - e^{-\eta_0 \dot{\gamma}/\tau_{12}^L}\right)$ where τ_{12}^L is the limiting shear stress, a concept frequently used in high-pressure lubrication.

These models are excellent for cases of moderate shear-thinning as observed for state points of $(\rho^*, T^*) = (0.4,1.5)$, and $(0.6,1.5)$, and illustrated in Fig. 5a. These models fail to accurately capture the dramatic shear-thinning feature of the LJ fluid at higher densities of $(\rho^*, T^*) = (0.8,1.0), (0.8,1.1), (0.8442,0.722)$ and $(0.9,1.1)$. For moderate shear-thinning, the Sisko equation is comparable in effectiveness to Eq. (3.18) and fits the data with $r^2 \cong 0.99$. The former fails to fit the data at state points where dramatic shear-thinning occurs. In contrast, Eq. (3.18) is consistent for all the LJ state points considered and captures the extreme shear-thinning effect. The Ree-Eyring and Bair-Winer equations, despite being widely considered more versatile than the Sisko, still suffer from the same drawbacks. In general, these equations are excellent models at low strain-rates, i.e., below the threshold where extreme shear-thinning sets in. The models are able to successfully capture the stress-deformation curve with $r^2 \cong 0.99$ for moderate shear-thinning, which falls to around $0.7 \leq r^2 \leq 0.8$ for extreme shear-thinning. The poor performance of these models at higher strain rates can be attributed to their empirical nature, where parameters are obtained by fitting experimental data, or their derivation from macro-viscoelastic models.

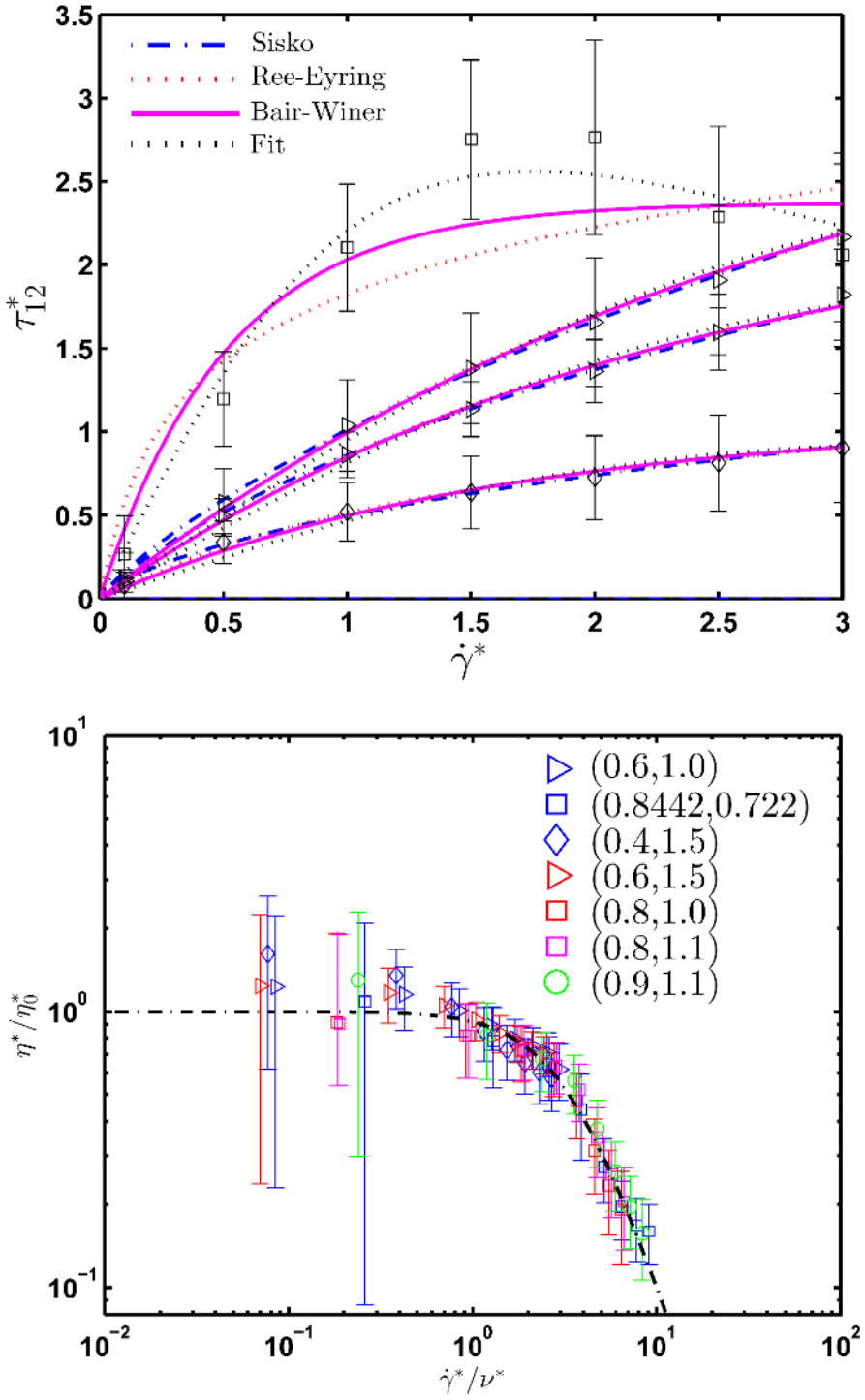

Fig. 5: (a) Demonstration of the ability of existing rheological equations to capture moderate shear-thinning in the LJ fluid and their inability to model extreme shear-thinning. The data markers are the same as used to identify the state points in Fig. 3. (b) Scaled viscosities for the LJ fluid at various state points for a system size of $n = 200$ particles. The fit is given by Eq. 21.

To obtain a strain-dependent viscosity model, we note that

$$\tau_{12} = \eta(\dot{\gamma})\,\dot{\gamma} \tag{3.21}$$

Thus, using Eq. (3.18) in Eq. (3.21), we find that

$$\frac{\eta^*}{\eta_0^*} = \frac{1}{1 + \frac{2}{3}\left(\frac{\dot{\gamma}^*}{\nu^*}\right)^2} \tag{3.22}$$

We compare our model with the well-established Cross viscosity model given in the literature as

$$\eta = \frac{\eta_0 - \eta_\infty}{1 + \beta\dot{\gamma}^n} + \eta_\infty \tag{3.23}$$

where β and n are fitting constants and η_∞ is the infinite shear-rate limiting viscosity. Interestingly, Eq. (3.22) yields the Cross viscosity model, with $n = 2$ and $\eta_\infty = 0$, absent empirical parameters since the parameters in Eq. (3.22) are completely determined by the fluid's density ρ^*, temperature T^*, and Newtonian viscosity η_0. To serve as a validation for our simulations, Eq. (3.22) yields a viscosity of $\eta_0 = 3.76$ at the LJ triple point of $(\rho^*, T^*) = (0.8442, 0.722)$, which is comparable to the value of $\eta_0 = 3.73$ calculated in the literature [60]. The Cross model has been previously used to model the strain-rate dependent viscosities of simple fluids, but in an empirical sense [5], [61]. It should be noted that our model has been completely derived from hydrodynamic and kinetic theories. A similar result has been obtained for the Ree-Eyring viscosity formula, which arose naturally from the Generalized Boltzmann equation.

In our model, we find that the effective collision parameter, ν^*, behaves as a universal scaling parameter that facilitates collapsing all the data onto a universal curve, suggesting the existence of a universal scaling law for the LJ fluid, as shown in Fig. 5b. The scatter is attributed to the inaccuracy of NEMD in accessing small strain-rates for viscosity calculations. Ideally, one would resort to the use of transient time correlation functions [62]. Additionally, we attribute the discrepancy between our calculations and those available in the literature to the truncation distance. In most studies, a truncation of $r_c = 2.5\sigma$ was used which would account

for the attractive component in the LJ potential as well, compared to $r_c = 2^{1/6}\sigma$ in this work.

3.3.3 Quasi-linearity Based on Continuum Thermomechanics

Note that Eq. (3.18) may allow one to determine a dissipation function which should equal the rate of entropy production [42]. Within the framework of thermomechanics, we know that the dissipation function is defined as

$$A_{kl}^{(d)}(\dot{d}_{ij})\dot{d_{kl}} = \Phi(\dot{d_{ij}}) \tag{3.24}$$

Where the dissipative forces $A_{kl}^{(d)}$ define a symmetric second-order tensor and $\dot{d}_{ij}$ is the deformation rate. For uniform shear flow, the dissipative forces are the shear stress σ_{ij}^{d}

$$\sigma_{ij}^{(d)}(d_{ij})d_{ij} = \Phi(d_{ij}) = \frac{\eta_0\dot{\gamma}^2}{1+\left(\frac{2}{3}\right)\left(\frac{\dot{\gamma}}{\nu}\right)^2} \tag{3.25}$$

Therefore, we have

$$\sigma_{ij}^{(d)} = \mu\frac{\partial\Phi}{\partial d_{ij}} \tag{3.26}$$

where μ is a constant of proportionality. Under uniform shear, we know that the three invariants are $d_{(1)} = 0$, $d_{(2)} = d_{12}^2 = \dot{\gamma}^2$, and $d_{(3)} = 0$. Therefore, on account of these side conditions Eq. (3.26) becomes

$$\sigma_{ij}^{(d)} = \mu\frac{\partial}{\partial d_{ij}}\left(\Phi - \lambda_1 d_{(1)} - \lambda_2 d_{(3)}\right) \tag{3.27}$$

where λ_1 and λ_2 are the Lagrange multipliers. Since d_{ij} is a deviatoric tensor, then so is σ_{ij}^{d}. Thus, we have $\sigma_{ii}^{d} = 0$. Furthermore, we also have $|\sigma_{ij}| = 0$. Upon expanding Eq. (3.27), we obtain

$$\sigma_{ij}^{(d)} = \mu\left[\frac{\partial\Phi}{\partial d_{(1)}}\frac{\partial d_{(1)}}{\partial d_{ij}} + \frac{\partial\Phi}{\partial d_{(2)}}\frac{\partial d_{(2)}}{\partial d_{ij}} + \frac{\partial\Phi}{\partial d_{(3)}}\frac{\partial d_3}{\partial d_{ij}} - \lambda_1\frac{\partial d_{(1)}}{\partial d_{ij}} - \lambda_2\frac{\partial d_3}{\partial d_{ij}}\right] \tag{3.28}$$

which simplifies to

$$\sigma_{ij}^{(d)} = \mu\left[\frac{\partial\Phi}{\partial d_{(2)}}\left(d_{ij} - d_{(1)}\delta_{ij}\right) - \lambda_1\delta_{ij} - \lambda_2(d_{ik}d_{kj} - d_{(2)}\delta_{ij})\right] \tag{3.29}$$

On account of the constraints, we have

$$-3\lambda_1 - \lambda_2\left(d_{ik}d_{kj} - 3d_{(2)}\right) = 0 \Rightarrow -3\lambda_1 + \lambda_2 d_{(2)} = 0 \tag{3.30a}$$

$$-\lambda_1 + \lambda_2 d_{(2)} = 0 \tag{3.30b}$$

Solving the system of Eqs. (3.30) yields $\lambda_1 = \lambda_2 = 0$, so that

$$\sigma_{ij}^{(d)} = \mu\frac{\partial\Phi}{\partial d_{(2)}}d_{ij} \tag{3.31}$$

Multiplying both sides of Eq. (3.31) with d_{ij} yields,

$$\Phi = \mu\frac{\partial\Phi}{\partial d_{(2)}}d_{ij}d_{ij} \tag{3.32}$$

For uniform shear, we obtain

$$\Phi = \mu\frac{\partial\Phi}{\partial\dot{\gamma}^2}(2\dot{\gamma^2}) \tag{3.33}$$

Substituting the explicit form for Φ in Eq. (3.33) and taking the derivative with respect to $\dot{\gamma}^2$, we obtain

$$\mu = \frac{1 + (2/3)(\dot{\gamma}^2/\nu^2)}{2} \tag{3.34}$$

Thus we see that a dissipation function of the form in Eq. (3.25) along with Eq. (3.31) suggest that a molecular fluid behaves at least like a quasi-linear fluid with a constitutive relationship of the form

$$\sigma_{ij}^{(d)} = 2\eta\left(d_{(2)}\right)d_{ij} \Rightarrow \sigma_{12}^{(d)} = 2\eta\left(\dot{\gamma}^2\right)\dot{\gamma} \tag{3.35}$$

where the fluid viscosity η needs to at least depend on $d_{(2)} = \dot{\gamma}^2$.

3.4 Conclusion

In this chapter, we simulated LJ fluids at different state points and employed the Boltzmann equation to study the behavior of the steady-state shear stress with applied strain rate. We observe that, in all cases, the fluid exhibits shear-thinning. At low densities, the shear-thinning effect is moderate for the range of strain-rates considered. At higher densities, dramatic shear-thinning sets in at much lower strain-rates. In light of these observations, we are motivated to use kinetic theory to find an equation of state that is able to capture this wide range of behaviors. We compare our proposed equation with other models available in the literature to validate its effectiveness.

In general, we find that the models from the literature performed well when the degree of shear-thinning is moderate. However, for cases of extreme shear-thinning, the Ostwald-deWaele and Sisko equations of state completely break down, while the Ree-Eyring and Bair-Winer equations experience a significant drop in modeling capability. In contrast, the proposed model performs consistently well across all state-points. Additionally, the formalism involving the Boltzmann equation naturally gives rise to a form of the Cross viscosity model as a steady-state solution. The effective collision frequency used in the BGK approximation acts as a scaling parameter that seems to unify the behavior of the LJ fluid across all the state-points considered.

Finally, a thermomechanical framework involving the dissipation function suggests that the LJ fluid behaves at least as a quasilinear fluid. This offers an insight into the minimum required approximations to be used in the process of

constructing a suitable constitutive model to represent a molecular fluid. The derivation shows that the proposed equation provides a suitable shear-thinning model while preserving thermodynamic orthogonality in molecular fluids, which is an important feature of continuum thermomechanics. The framework of thermodynamic orthogonality provides a means for transitioning from molecular to continuum scales and for a link to the fluctuation theorem which grasps spontaneous violations of the second law of thermodynamics on very small length and/or time scales [39]. Thus, for the purposes of modeling such fluids as continua, we need to assume that the viscosity is dependent on the strain-rate in a manner consistent with the postulates of continuum thermomechanics.

In Chapter 4, we illustrate that non-Newtonian behavior results from non-Gaussian fluctuations that correspond to the formation of structural order within the fluid. Therefore, we need to move beyond Gaussian statistics to characterize the fluid's internal dynamics and provide and all-encompassing description of fluid behavior under shear flow.

Chapter 4

Stochastic Characteristics and Second Law Violations of Atomic Fluids in Couette flow

4.1 Introduction[2]

When the system size is small, i.e. in the micro or nanoscale, classical models based on continuum theories are insufficient. Continuum models often disregard the underlying stochastic processes that yield the observable fluid behavior, thereby providing an inadequate description of the overall system. Such systems require a statistical treatment rather than a deterministic one. To characterize the statistical nature of such systems, one needs to resort to molecular dynamics (MD) simulation techniques to extract pertinent information regarding the statistical moments and the temporal and spectral characteristics. NEMD techniques and, in particular, the SLLOD equations of motion, are well established and documented tools to model atomic fluids undergoing planar Couette flow [50], [51], [52]. Owing to the chaotic nature of molecular movement and interactions within the flow field, the state variables of interest are accompanied by significant fluctuations, and thus must be dealt with in a statistical sense. In the specific case of a planar Couette flow, we focus on the statistics of the shear stress and density perturbations. The latter is a randomly fluctuating field superimposed on the mean fluid density such that its spatial and temporal averages are zero.

We use NEMD with the SLLOD equations to study the statistical and structural features of atomic fluids that undergo Couette flow, with the particles interacting via a Lennard-Jones (LJ) potential. We study the autocorrelation function, power-spectral density, and bispectrum of the shear stress and local density fluctuations to gain insight into the shear-thinning characteristics of this

[2] Adapted from: B. V. Raghavan, P. Karimi and M. Ostoja-Starzewski, "Stochastic characteristics and second law violations of atomic fluids in Couette flow," *Physica A: Statistical Mechanics and its Applications*, vol. 496, pp. 90-107, 2018.

system and its departure from a Gaussian system. We motivate the need to study these variables by illustrating the natural connection between them via the fluctuation theorem (FT). Using principles of information theory, we derive a probabilistic model for the shear stress that accounts for negative shear stress increments and thus for violations of the second law of thermodynamics. We describe the departure from Gaussian statistics as the fluid enters the nonlinear flow regime and describe how these changes can be used to identify the critical strain rate, and thus justifying the need for a more general probabilistic model. For the sake of clarity, we explain our observations based on a single LJ state-point and then elaborate on the effects of density and temperature variations on the above parameters.

4.2 The Macroscopic Connection

4.2.1 Linear Perturbation and Local Density Fluctuations

The two variables of primary interest in characterizing Couette flow in the linear and nonlinear shear-thinning regime are the temporal shear stress fluctuations and the local temporal density fluctuations. To study their statistical nature under Couette flow, we investigate local density contrast in the fluid and its relationship to microscopic phenomena via connections established by the governing equations of fluid dynamics. We define the local density contrast as

$$\delta(\boldsymbol{r},t)=\frac{\rho(\boldsymbol{r},t)-\rho_0}{\rho_0}\Leftrightarrow\rho(\boldsymbol{r},t)=\rho_0[1+\delta(\boldsymbol{r},t)] \tag{4.1}$$

where ρ_0 is the prescribed fluid density. We treat δ as small perturbations, i.e. $\delta \ll 1$, which is zero at the boundaries. We also introduce velocity perturbations as

$$\boldsymbol{v}(\boldsymbol{r},t)=\boldsymbol{v}'(\boldsymbol{r},t)+\boldsymbol{u}(\boldsymbol{r},t) \tag{4.2}$$

where $\boldsymbol{v}'$ is the fluctuating velocity (that can be attributed to the peculiar velocity of fluid particles). The perturbations are zero at the boundaries of the domain, i.e. $\boldsymbol{v}'(y=0,t)=\boldsymbol{v}'(y=h,t)=0$. We consider $||\boldsymbol{v}'||$ as being 'small', so we may

neglect quadratic terms of order $||\boldsymbol{v}'||\delta$, in accordance with linear perturbation theory. Finally, we also consider fluctuations in the pressure as

$$P(\boldsymbol{r},t) = P'(\boldsymbol{r},t) + P(\boldsymbol{r},t) \tag{4.3}$$

which can be thought of as the sum of thermodynamic (P') and dynamic pressure (P).

To obtain a transport equation for $\delta(\boldsymbol{r},t)$ under isothermal conditions (in accordance with the thermosttated SLLOD equations) we use the continuity and Navier-Stokes equations of fluid mechanics which are respectively

$$\frac{\partial \rho}{\partial t} + \nabla.(\rho \boldsymbol{v}) = 0 \tag{4.4}$$

$$\left(\frac{\partial}{\partial t} + \boldsymbol{v}.\nabla\right)\boldsymbol{v} = -\frac{1}{\rho}\nabla P + \nu\nabla^2\boldsymbol{v} + \frac{1}{3}\nu\nabla(\nabla.\boldsymbol{v}) + f \tag{4.5}$$

where P is the pressure, ν is the kinematic viscosity, and f are external forces. Substituting Eq. (4.2) and Eq. (4.3) in Eq. (4.4), and subtracting the perturbed equations from the unperturbed ones, we obtain

$$\frac{\partial \delta}{\partial t} + \nabla.([1+\delta]\boldsymbol{v}') = 0 \tag{4.6}$$

and eliminating all quadratic terms yields

$$\frac{\partial \delta}{\partial t} + \nabla.\boldsymbol{v}' = 0 \tag{4.7}$$

In a similar manner, we substitute Eq. (4.2) and Eq. (4.3) in Eq. (4.5) and performing the same operation as above, we obtain,

$$\begin{aligned} &\frac{\partial \boldsymbol{v}'}{\partial t} + (\boldsymbol{v}'.\nabla)\boldsymbol{v}' + (\boldsymbol{v}'.\nabla)\boldsymbol{u} + (\boldsymbol{u}'.\nabla)\boldsymbol{v}' \\ &= -\frac{1}{\rho}\nabla P' + \nu\nabla^2\boldsymbol{v}' + \frac{1}{3}\nu\nabla(\nabla.\boldsymbol{v}') \end{aligned} \tag{4.8}$$

which after eliminating the quadratic term $(\boldsymbol{v}'.\nabla)\boldsymbol{v}'$ reduces to

$$\frac{\partial \boldsymbol{v}'}{\partial t} + (\boldsymbol{v}'.\nabla)\boldsymbol{u} + (\boldsymbol{u}.\nabla)\boldsymbol{v}' = -\frac{1}{\rho_0(1+\delta)}\nabla P' + \nu\nabla^2\boldsymbol{v}' + \frac{1}{3}\nu\nabla(\nabla.\boldsymbol{v}') \qquad (4.9)$$

The goal now is to write the thermodynamic pressure, P', in terms of the density. We achieve this by using the thermodynamic relation

$$TdS = dU + P'dV \qquad (4.10)$$

where dS is the change in entropy of the system, dU is the flow of energy into the system, and $P'dV$ is the work done on the system. The ideal gas relations

$$P' = \rho k_B T \qquad (4.11a)$$

$$U = \frac{3}{2}k_B T \qquad (4.11b)$$

with k_B being the Boltzmann constant are combined to yield

$$U = \frac{3}{2}\frac{P'}{\rho} \qquad (4.12)$$

Substituting the relations in Eq. (4.11a) and Eq. (4.12) into Eq. (4.10), we obtain

$$TdS = d\left(\frac{3}{2}\frac{P'}{\rho}\right) + P'd\left(\frac{1}{\rho}\right) \qquad (4.13)$$

Substituting for the temperature using Eq. (4.11a), and expanding Eq. (4.13) yields

$$\frac{1}{k_B}\frac{P'}{\rho}dS = \frac{3}{2}\frac{1}{\rho}dP' + \frac{5}{2}P'd\left(\frac{1}{\rho}\right) \qquad (4.14)$$

which can be rearranged as

$$\frac{dP'}{P'} = \frac{1}{k_B}dS - \frac{5}{2}\rho d\left(\frac{1}{\rho}\right) \qquad (4.15)$$

Integrating Eq. (4.15) and simplifying yields,

$$P' = \rho^{5/3}e^{\frac{2}{3k_B}S} \qquad (4.16)$$

which implies that $P' = P'(\rho, S)$. Then, we can express the gradient of the pressure in terms of the density and entropy as

$$\nabla P = \left(\frac{\partial P'}{\partial \rho}\right)_S \nabla\rho + \left(\frac{\partial P'}{\partial S}\right)_\rho \nabla S = c_s^2 \nabla\rho + \frac{2}{3}\rho T \nabla S \tag{4.17}$$

Substituting Eq. (4.17) in Eq. (4.9) gives

$$\begin{aligned} &\frac{\partial \boldsymbol{v}'}{\partial t} + (\boldsymbol{v}'.\nabla)\boldsymbol{u} + (\boldsymbol{u}.\nabla)\boldsymbol{v}' \\ &= -\frac{1}{\rho_0(1+\delta)}[K\nabla\rho + \frac{2}{3}\rho T\nabla S] + \nu\nabla^2\boldsymbol{v}' + \frac{1}{3}\nu\nabla(\nabla.\boldsymbol{v}') \end{aligned} \tag{4.18}$$

where K is the bulk modulus of the fluid. Simplifying the above equation and using $\delta \ll 1$, we obtain

$$\frac{\partial \boldsymbol{v}'}{\partial t} + (\boldsymbol{v}'.\nabla)\boldsymbol{u} + (\boldsymbol{u}.\nabla)\boldsymbol{v}' = -[c_s^2\nabla\rho + \frac{2}{3}T\nabla S] + \nu\nabla^2\boldsymbol{v}' + \frac{1}{3}\nu\nabla(\nabla.\boldsymbol{v}') \tag{4.19}$$

Operating with $-\nabla.(.)$, we obtain,

$$\begin{aligned} &\frac{\partial(-\nabla.\boldsymbol{v}')}{\partial t} - \nabla.[(\boldsymbol{v}'.\nabla)\boldsymbol{u} + (\boldsymbol{u}.\nabla)\boldsymbol{v}'] \\ &= \left[c_s^2\nabla^2\rho + \frac{2}{3}T\nabla^2 S\right] - \nabla.[\nu\nabla^2\boldsymbol{v}'] - \nabla.\left[\frac{1}{3}\nu\nabla(\nabla.\boldsymbol{v}')\right] \end{aligned} \tag{4.20}$$

and using Eq. (4.7) in Eq. (4.20) and making the appropriate substitution yields

$$\frac{\partial^2\delta}{\partial t^2} + \frac{4}{3}\nu\nabla^2\left(\frac{\partial\delta}{\partial t}\right) - \rho_0 c_s^2\nabla^2\delta = \frac{2}{3}T\nabla^2 S + \nabla.[(\boldsymbol{v}'.\nabla)\boldsymbol{u} + (\boldsymbol{u}.\nabla)\boldsymbol{v}'] \tag{4.21}$$

which is a third order wave equation for local density contrast in the fluid. The first term on the left-hand side is related to the entropy production, and the second term is the coupling between the external driving force, i.e. the strain rate captured by $\boldsymbol{u}$ and $\nabla\boldsymbol{u}$ (as shown in Eq. (2.4) and Eq. (2.5), respectively), and the fluctuating velocity field.

4.2.2 Entropy Production and Violations of the Second Law of Thermodynamics

Considering Eq. (4.21), we now define the dissipation function as

$$\Omega_{\mathrm{t}}[\boldsymbol{\Gamma}(t)] = \int_0^s \Omega[\boldsymbol{\Gamma}(s)]ds = \ln\left[\frac{f(\boldsymbol{\Gamma}(0),0)}{f(\boldsymbol{\Gamma}(t),0)}\right] - \int_0^t \Lambda[\boldsymbol{\Gamma}(s)]ds \tag{4.22}$$

where $\boldsymbol{\Gamma}$ is the phase space, and $f(\boldsymbol{\Gamma}(t),t)$ is the phase space distribution function and $\Lambda[\boldsymbol{\Gamma}(t)]$ is the phase space compression factor. Equivalently, it can also be expressed as

$$\Omega_{\mathrm{t}}[\boldsymbol{\Gamma}(t)] = \Sigma(t) = \beta \boldsymbol{J}(t) F_e V \tag{4.23}$$

where $\boldsymbol{J}(t)$ is the dissipative flux, F_e is the external dissipative field, V is the system volume, and $\beta = 1/k_B T$. The dissipation function, Ω_t, is equal to the total irreversible entropy production rate, $\Sigma(t)$. So, we can set $S = \Sigma(t)/V$. It is through the dissipation function that violations of the second law of thermodynamics are explored.

Violations of the second law of thermodynamics are captured via the *fluctuation theorem* [13]. Mathematically, it is expressed as

$$\frac{p(\Omega_t = A)}{p(\Omega_t = -A)} = e^{-AVt} \tag{4.24}$$

representing the ratio of observing positive and negative instances of negative entropy production. It is evident from the formulation that as the system size increases or the time period of observation extends to infinity, the probability of observing negative instances of entropy production decrease exponentially.

In the case of Couette flow, $\boldsymbol{J}(t) = \tau_{xy}(t)$, which is the total shear stress, i.e. $\tau_{xy}(t) = \langle \tau_{xy} \rangle + \tau'_{xy}(t)$. The first term is due to the streaming velocity profile with $\langle \tau_{xy} \rangle = \eta\dot{\gamma}$ which is a deterministic process that contributes to the increasing rate of entropy within the system, and the second term is the time-dependent fluctuating component owing to the stochastic nature of the system [45], [63]. It is through the second term that the system can violate the second law of

thermodynamics. In order to observe such violations, one observes the distribution of the shear stress, through which one can explicitly identify violating instances. For more details, readers are referred to [39]. Thus, using the rate of entropy production per unit volume given by $S = \Omega_t/VT$ in Eq. (4.21) and the fact that $1/V = \rho/m$, where m is the molecular mass of the fluid and V is the system volume, we obtain

$$\frac{\partial^2\delta}{\partial t^2} + \frac{4}{3}\nu\nabla^2\left(\frac{\partial\delta}{\partial t}\right) - \rho_0 c_s^2\nabla^2\delta = \frac{2}{3}\nabla^2\frac{\rho\Omega_t}{m} + \nabla.[(\boldsymbol{v}'.\nabla)\boldsymbol{u} + (\boldsymbol{u}.\nabla)\boldsymbol{v}'] \quad (4.25)$$

Eq. (4.25) simplifies to

$$\frac{\partial^2\delta}{\partial t^2} + \frac{4}{3}\nu\nabla^2\left(\frac{\partial\delta}{\partial t}\right) - \left(\rho_0 c_s^2 + \frac{2\rho_0\Omega_t}{3m}\right)\nabla^2\delta = \nabla.[(\boldsymbol{v}'.\nabla)\boldsymbol{u} + (\boldsymbol{u}.\nabla)\boldsymbol{v}'] \quad (4.26)$$

Now, we take a closer look at the right-hand side of Eq. (4.26). Taking the volume integral, and applying the divergence theorem, we have

$$\int_V \nabla.[(\boldsymbol{v}'.\nabla)\boldsymbol{u} + (\boldsymbol{u}.\nabla)\boldsymbol{v}']dV = \int_{\partial V}[(\boldsymbol{v}'.\nabla)\boldsymbol{u} + (\boldsymbol{u}.\nabla)\boldsymbol{v}'].\hat{\boldsymbol{n}}da \quad (4.27)$$

The first term in Eq. (4.27) is 0 due to the boundary conditions on $\boldsymbol{v}'$**.** Evaluating the second term for Couette flow yields,

$$\int_{\partial V}[(\boldsymbol{u}.\nabla)\boldsymbol{v}'].\hat{\boldsymbol{n}}da = \int_{y=h} U\frac{\partial v_x'}{\partial y}dxdz \quad (4.28)$$

where $U = \dot{\gamma}h$ is the velocity of the top plate, and $\partial v_x'/\partial y = \tau'_{xy}(t)$ is the time-dependent fluctuating component of the shear stress. Thus, Eq. (4.28) becomes

$$\int_{y=h} U\frac{\partial v_x'}{\partial y}dxdz = \dot{\gamma}\tau'_{xy}(t)h\int_{y=h}dxdz = \dot{\gamma}\tau'_{xy}(t)V = \int_V \dot{\gamma}\tau'_{xy}(t)dV \quad (4.29)$$

Therefore, we can write Eq. (4.26) as

$$\frac{\partial^2\delta}{\partial t^2} + \frac{4}{3}\nu\nabla^2\left(\frac{\partial\delta}{\partial t}\right) - \left(\rho_0 c_s^2 + \frac{2\rho_0\Omega_t}{3m}\right)\nabla^2\delta = \dot{\gamma}\tau'_{xy}(t) \quad (4.30)$$

where $\tau'_{xy}(t)$ is a stochastic term. Eq. (4.30) is a stochastic partial differential equation that illustrates the intimate connection between local density fluctuations and the shear stress. It should be noted that $\tau'_{xy}(t)$ is a stochastic forcing term, through which the possibility of second-law violations is explicitly captured in the system. As a consequence, it would be prudent to study the statistical properties of the density fluctuations, δ and the shear stress, $\tau_{xy}(t)$. In the continuum limit as the system size increases, statistical fluctuations in the shear stress are negligible resulting in a deterministic equation of the form

$$\frac{\partial^2 \delta}{\partial t^2} + \frac{4}{3}\nu\nabla^2\left(\frac{\partial \delta}{\partial t}\right) - \left(\rho_0 c_s^2 + \frac{2\rho_0 \eta \dot{\gamma}^2}{3mk_B T}\right)\nabla^2\delta = 0 \tag{4.31}$$

where the influence of the shear stress owing to the stochastic motion on the microscale disappears entirely.

4.2.3 Probability Density Function of the Stress Tensor

Based on the statistical nature of the shear stress in molecular Couette flow, and its non-Gaussian nature, we are inclined to develop a non-Gaussian probabilistic model for the shear stress that can account for non-zero higher order statistics. In the linear flow regime, τ_{xy} is approximately Gaussian. But, this is not the case in the nonlinear flow regime. To capture both these effects we develop a general probability distribution function. We bear in mind that at the molecular scale, the shear stress can spontaneously attain negative values, which corresponds to negative entropy production and which means that the second law of thermodynamics holds only in a statistical (average) sense and not in an absolute one.

Primarily, we are interested in the steady-state probability density function (PDF) of the shear stress. We compute the PDF for the stress tensor, and obtain the PDF for the shear stress as a marginal distribution. To obtain a general expression, we use the *principle of maximum entropy* (MaxEnt) to obtain a suitable probability distribution for the stress tensor subjected to certain inherent constraints on its

moments. The random pressure tensor (which is the negative of the stress tensor, i.e. $\mathbf{P} = -\mathbf{T} \Leftrightarrow P_{12} = -\tau_{12}$) is defined as,

$$\mathbf{P} = P_{kl} := -\left(\sum_{i=1}^{N} \frac{p_{ik} p_{il}}{m} - \frac{1}{2} \sum_{i,j}^{N} r_{ijk} F_{ijl} \right), \qquad \mathbf{P} \in \mathbb{R}^{+}_{2\times 2} \tag{4.32}$$

We are interested in maximizing the differential entropy defined as

$$S(f_{\mathbf{P}}) := -\int f(\mathbf{P}) ln\,[f(\mathbf{P})]\, d\mathbf{P} \tag{4.33}$$

To maximize S_f, we need suitable constraints on $f(\mathbf{P})$. The first constraint is the normalization constraint

$$\int f(\mathbf{P})\, d\mathbf{P} = 1 \tag{4.34}$$

Under steady-state conditions, we know that the mean $\langle P_{kl} \rangle$ exists. Additionally, moments of the inverse of $\mathbf{P}$ must also exist since $\mathbf{P}$ is invertible. Restricting ourselves to the first moment in the latter, we obtain the constraints as

$$\int \mathbf{P} f(\mathbf{P})\, d\mathbf{P} = \langle \mathbf{P} \rangle \Rightarrow \mathrm{E}(\mathbf{P}) = \langle \mathbf{P} \rangle \tag{4.35a}$$

$$\int ln\,(|\mathbf{P}|) f(\mathbf{P})\, d\mathbf{P} = \kappa \Rightarrow \mathrm{E}(ln\,(|\mathbf{P}|)) = \kappa, \qquad \kappa < +\infty \tag{4.35b}$$

where $|\mathbf{P}|$ is the determinant of $\mathbf{P}$. Using the constraints in Eqs. (4.34), (4.35a), and (4.35b), we maximize the differential information entropy in Eq. (4.33) using Lagrange multipliers. We define the objective function to be maximized as,

$$\begin{aligned} \mathcal{F} = &-\int f(\mathbf{P})\, ln[f(\mathbf{P})]\, d\mathbf{P} - \lambda_0 \left(\int_{\mathbf{P}} f(\mathbf{P}) d\mathbf{P} - 1 \right) \\ &- \lambda_1 \left(\int_{\mathbf{P}} ln(|\mathbf{P}|)\, f(\mathbf{P})\, d\mathbf{P} - \nu \right) \\ &- Tr \left[\mathbf{\Lambda_2} \left(\int_{\mathbf{P}} \mathbf{P} f(\mathbf{P})\, d\mathbf{P} - \langle \mathbf{P} \rangle \right) \right] \end{aligned} \tag{4.36}$$

where λ_0, λ_1, and $\mathbf{\Lambda}_2$ are Lagrange multipliers, and Tr is the trace operator. Thus, we have

$$\frac{\partial \mathcal{F}}{\partial f(\mathbf{P})} = 0 \Rightarrow -(1 + \ln[f(\mathbf{P})]) - \lambda_0 - \lambda_1 \ln(|\mathbf{P}|) - Tr(\mathbf{\Lambda_2 P}) = 0 \qquad (4.37)$$

The solution to Eq. (4.37) is

$$ln[f(\mathbf{P})] = -(1 + \lambda_0) - \lambda_1 \ln(|\mathbf{P}|) - Tr(\mathbf{\Lambda_2 P}) \qquad (4.38)$$

Or,

$$f(\mathbf{P}) = e^{-(1+\lambda_0)} |\mathbf{P}|^{-\lambda_1} e^{-Tr(\mathbf{\Lambda_2 P})} \qquad (4.39)$$

To find the Lagrange multipliers, we substitute Eq. (4.39) into the constraint equations. The next steps are as follows.

i. Using the normalization condition, we have

$$\int_{\mathbf{P}} e^{-(1+\lambda_0)} |\mathbf{P}|^{-\lambda_1} e^{-Tr(\mathbf{\Lambda_2 P})} \, d\mathbf{P} = 1 \qquad (4.40)$$

which implies that

$$\int_{\mathbf{P}} |\mathbf{P}|^{-\lambda_1} e^{-Tr(\mathbf{\Lambda_2 P})} \, d\mathbf{P} = e^{(1+\lambda_0)} \qquad (4.41)$$

Using the matrix generalization of the Laplace transform [64], we find that

$$e^{(1+\lambda_0)} = |\mathbf{\Lambda}_2|^{\lambda_1 - \frac{n+1}{2}} \Gamma_n \left(\frac{n+1}{2} - \lambda_1 \right) \qquad (4.42)$$

Thus, we have

$$f(\mathbf{P}) = \frac{|\mathbf{\Lambda}_2|^{-\lambda_1 + \frac{n+1}{2}}}{\Gamma_n \left(\frac{n+1}{2} - \lambda_1 \right)} |\mathbf{P}|^{-\lambda_1} e^{-Tr(\mathbf{\Lambda_2 P})} \qquad (4.43)$$

ii. To obtain $\mathbf{\Lambda}_2$, we obtain the mean corresponding to the distribution in Eq. (4.43). The matrix characteristic function of $\mathbf{P}$ is defined as

$$\psi_{\mathbf{P}}(\mathbf{P}) = E\left[e^{Tr(i\mathbf{\Pi P})}\right] = \int_{\mathbf{P}} e^{Tr(i\mathbf{\Pi P})} f(\mathbf{P}) d\mathbf{P} \tag{4.44}$$

Substituting Eq. (4.43) in (4.44), we have

$$\begin{aligned}\psi_{\mathbf{P}}(\mathbf{P}) &= \frac{|\mathbf{\Lambda}_2|^{-\lambda_1+\frac{n+1}{2}}}{\Gamma_n\left(\frac{n+1}{2}-\lambda_1\right)} \int_{\mathbf{P}} e^{-Tr[-(\mathbf{\Lambda_2}-i\mathbf{\Pi})\mathbf{P}]} |\mathbf{P}|^{-\lambda_1} d\mathbf{P} \\ &= |\mathbf{\Lambda}_2|^{-\lambda_1+\frac{n+1}{2}} |\mathbf{\Lambda_2} - i\mathbf{\Pi}|^{\lambda_1-\frac{n+1}{2}} = |\mathbf{I} - i\mathbf{\Pi}\mathbf{\Lambda}_2^{-1}|^{\lambda_1-\frac{n+1}{2}}\end{aligned} \tag{4.45}$$

Using the cumulant (an alternative set of quantities to moments describing a PDF) generating function, we have

$$\begin{aligned}ln[\psi_{\mathbf{P}}(\mathbf{P})] &= \left(\lambda_1 - \frac{n+1}{2}\right) ln|\mathbf{I} - i\mathbf{\Pi}\mathbf{\Lambda}_2^{-1}| \\ &= \left(\lambda_1 - \frac{n+1}{2}\right)[(-i\mathbf{\Pi}\mathbf{\Lambda}_2^{-1}) + \frac{1}{2}(-i\mathbf{\Pi}\mathbf{\Lambda}_2^{-1})^2 + \cdots]\end{aligned} \tag{4.46}$$

From which we obtain the mean as

$$E(\mathbf{P}) = \frac{\partial \ln\left[\psi_{\mathbf{P}}(\mathbf{P})\right]}{\partial(i\mathbf{\Omega})}\bigg|_{\mathbf{\Omega}=0} = \left(\lambda_1 - \frac{n+1}{2}\right)\mathbf{\Lambda}_2^{-1} \tag{4.47}$$

Comparing Eq. (4.47) with (4.35a) yields

$$\left(\lambda_1 - \frac{n+1}{2}\right)\mathbf{\Lambda}_2^{-1} = \langle\mathbf{P}\rangle \Rightarrow \mathbf{\Lambda}_2 = \left(\lambda_1 - \frac{n+1}{2}\right)\langle\mathbf{P}\rangle^{-1} \tag{4.48}$$

From (i) and (ii), we see that the probability density function for the pressure tensor is given by

$$\begin{aligned}&f(\mathbf{P}; \lambda_1, n, \langle\mathbf{P}\rangle^{-1}) \\ &= \frac{\left(\lambda_1 - \frac{n+1}{2}\right)^{\boldsymbol{n}\left(\lambda_1-\frac{n+1}{2}\right)} |\langle\mathbf{P}\rangle|^{\lambda_1-\frac{n+1}{2}}}{\Gamma_n\left(\frac{n+1}{2}-\lambda_1\right)} |\mathbf{P}|^{-\lambda_1} e^{-Tr\left[\left(\lambda_1-\frac{n+1}{2}\right)\langle\mathbf{P}\rangle^{-1}\mathbf{P}\right]}\end{aligned} \tag{4.49}$$

which is recognized as the matrix-variate gamma distribution. We leave λ_1 as a free modeling parameter in Eq. (4.49).

The probability density for the shear component of the pressure tensor (or the shear stress) is found via the Bartlett decomposition. Explicitly, the scale matrix is given by for the probability distribution in Eq. (4.49) is given by

$$\langle \mathbf{P} \rangle = \begin{pmatrix} \langle P_{11} \rangle & \langle P_{12} \rangle \\ \langle P_{12} \rangle & \langle P_{22} \rangle \end{pmatrix} \tag{4.50}$$

The Lower Cholesky factor of $\langle \mathbf{P} \rangle$ is given by

$$\mathbf{L} = \begin{pmatrix} \sqrt{\langle P_{11} \rangle} & 0 \\ \dfrac{\langle P_{12} \rangle}{\sqrt{\langle P_{11} \rangle}} & \sqrt{\dfrac{\langle P_{11} \rangle \langle P_{22} \rangle - \langle P_{12} \rangle^2}{\langle P_{11} \rangle}} \end{pmatrix} \tag{4.51}$$

Using the Bartlett decomposition, we express the random stress tensor as

$$\mathbf{P} = \mathbf{L}\mathbf{A}\mathbf{A}^T\mathbf{L}^T \tag{4.52}$$

where the matrix $\mathbf{A}$ is given by

$$\mathbf{A} = \begin{pmatrix} g_1 & 0 \\ n_{12} & g_2 \end{pmatrix} \tag{4.53}$$

where $g_i^2 \sim \Gamma(a, b)$ and $n_{ij} \sim \mathcal{N}(0,1)$. Due to molecular interactions, the parameters a and b are in general non-integer parameters. We expect a reduction to the chi-squared distribution when molecular interactions are neglected. That is, $g_i^2 \sim \Gamma\left(\frac{n-i+1}{2}, \frac{1}{2}\right) = \chi^2_{n-i+1}$.

Expanding Eq. (4.52), we obtain the expression for P_{12} as

$$P_{12} = g_1^2 \langle P_{12} \rangle + g_1 n_{12} \sqrt{\langle P_{11} \rangle \langle P_{22} \rangle - \langle P_{12} \rangle^2} \tag{4.54}$$

which we recognize as a normal variance-mean mixture with the mixing density being a gamma distribution. The PDF is given by

$$f(P_{12}) = \int_0^\infty \frac{1}{\sqrt{2\pi\sigma^2 g_1^2}} e^{\left[\frac{-\left(P_{12} - \beta g_1^2\right)^2}{2\sigma^2 g_1^2}\right]} h(g_1^2) dg_1^2 \tag{4.55}$$

where $\beta = \eta(\dot{\gamma})\dot{\gamma}$ and $\sigma = \sqrt{\langle P_{11}\rangle\langle P_{22}\rangle - \langle P_{12}\rangle^2}$, and $h(g_1^2)$ is the gamma distribution $\Gamma(a, b)$ with a and b being adjustable parameters (of the gamma distribution) based on the data being modeled. Carrying out the integration in Eq. (4.55) with

$$h(g_1^2) = \frac{a^b}{\Gamma(b)}(g_1^2)^{b-1}e^{-a(g_1^2)} \tag{4.56}$$

we obtain the most suitable distribution for P_{12} as the variance-gamma distribution expressed as

$$\begin{aligned} f(P_{12}; a, b, \beta, \sigma, \langle P_{12}\rangle) \\ &= \frac{2a^b}{\Gamma(b)\sigma^2\sqrt{2\pi(\beta^2 + 2a\sigma^2)^{b-\frac{1}{2}}}}|P_{12} \\ &- \langle P_{12}\rangle|^{b-\frac{1}{2}}K_{b-\frac{1}{2}}\left(\frac{\sqrt{\beta^2 + 2a\sigma^2}}{\sigma^2}|P_{12}\right. \\ &\left. - \langle P_{12}\rangle|\right)e^{\frac{\beta}{\sigma^2}|P_{12}-\langle P_{12}\rangle|} \end{aligned} \tag{4.57}$$

4.3 Results

In this section, we discuss the structural features of the fluid under shear flow and investigate the stochastic processes governing its observable behavior. We illustrate the inadequacy of Gaussian approximations and propose a more general statistical description that captures the two distinct flow regimes (i.e. the Newtonian and shear-thinning regimes). We describe how changes in the fluid's statistical properties correspond to the emergence of structure, thus enabling us to use the former as a proxy to identify different flow regimes and the nature of structural transitions.

4.3.1 Stochastic Characteristics of Density Fluctuations and Shear Stress

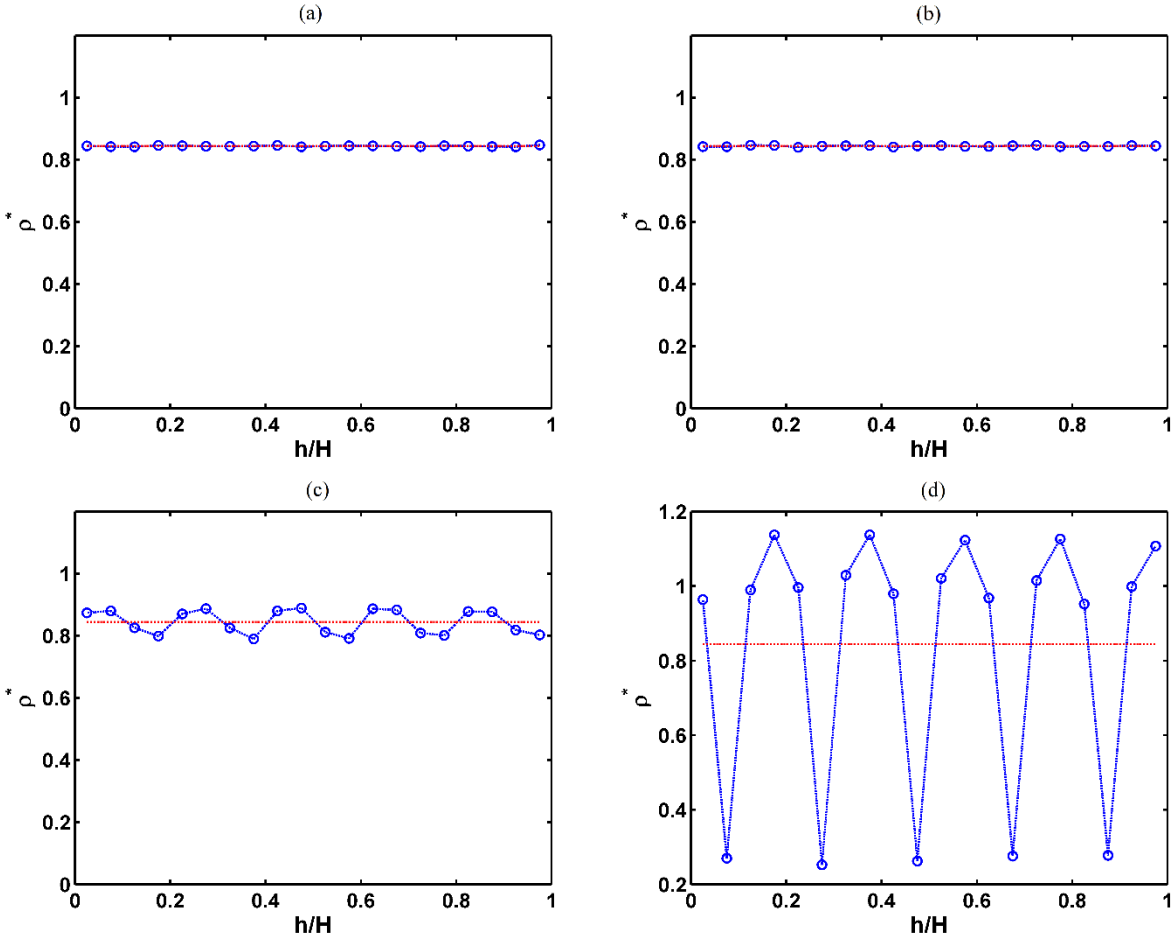

Fig. 6: Density profiles for the LJ fluid at the state point $(\rho^*, T^*) = (0.8442, 0.722)$ for (a) $\dot{\gamma}^* = 0.1$ and (b) $\dot{\gamma}^* = 0.5$ and (c) $\dot{\gamma}^* = 1.5$ and (c) $\dot{\gamma}^* = 2.5$. The red line indicates the average prescribed density, and the blue line with markers indicates the actual density profile during the simulation.

There exists a critical strain rate above which the LJ fluid begins to exhibit shear-thinning in Couette flow [3], [4], [6], [7], [34]. This is characterized by a drop in shear stress as depicted in a plot of stress and strain rate [35]. The reason is that above the critical strain-rate, fluid particles begin to align in the direction of the flow and develop into a so-called 'string phase'. Therefore, there is a decrease in friction between fluid layers and an observable drop in the shear-stress and viscosity of the fluid. The string phase is considered to be an artifact of the

thermostatting mechanism, which artificially imposes a streaming velocity profile [6], [10]. Nonetheless, it is a physical development in the system being modeled which provides insight into the simulation algorithm as well as shear-thinning fluids in microscale and nanoscale systems. We focus on studying the statistical characteristics and features of the flow that accurately describe the linear and nonlinear flow regimes. We focus on investigating the statistical nature of the local density contrast as expressed in Eq. (4.2) and the shear stress. The former is a useful metric by which we can identify the development of the 'string-phase', and the latter is closely related to the stability of the fluid [33], [34].

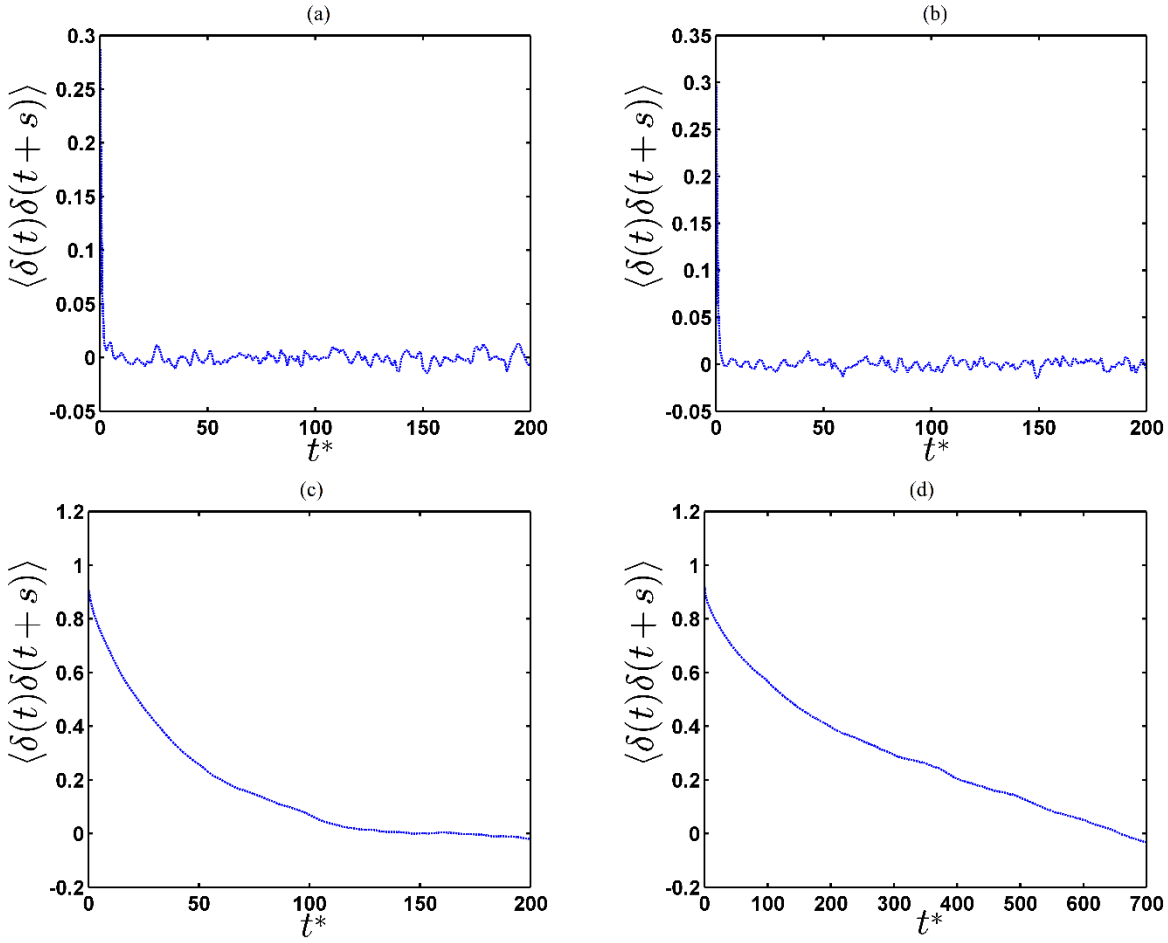

Fig. 7: Autocorrelation function of the local density contrast for the LJ fluid at the state point $(\rho^*, T^*) = (0.8442, 0.722)$ for (a) $\dot{\gamma}^* = 0.1$ and (b) $\dot{\gamma}^* = 0.5$ and (c) $\dot{\gamma}^* = 1.5$ and (d) $\dot{\gamma}^* = 2.5$.

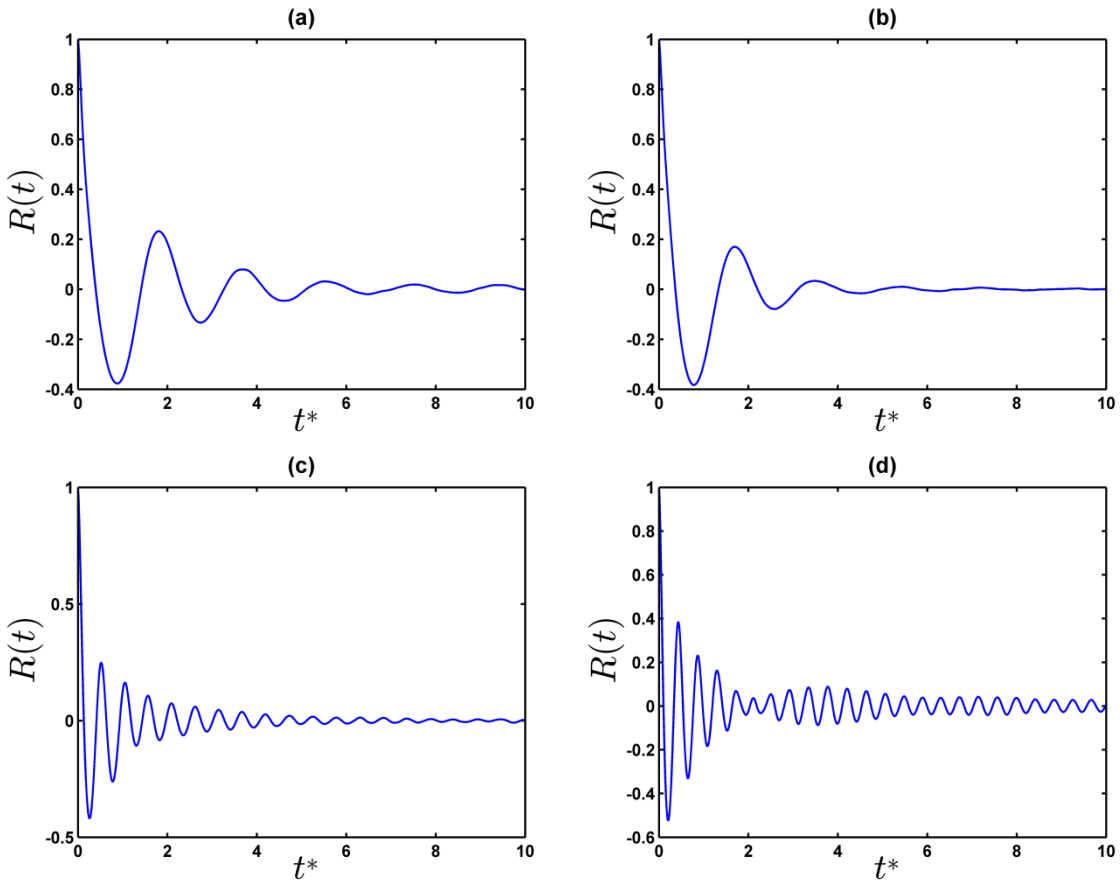

Fig. 8: Shear stress autocorrelation function for the LJ fluid at the state point $(\rho^*, T^*) = (0.8442, 0.722)$ at (a) $\dot{\gamma}^* = 0.1$ (b) $\dot{\gamma}^* = 0.5$ (c) $\dot{\gamma}^* = 1.5$, and (d) $\dot{\gamma}^* = 2.5$. The top plots are in the linear regime and the bottom plots are the nonlinear regime.

Although the LJ fluid being simulated is inherently homogeneous, there exists a critical strain-rate above which extreme shear-thinning occurs due to the development of structural anisotropy, owing to the formation of a 'string-phase' in which molecules tend to align themselves along the direction of the flow. To explore this phenomenon further, we study the spatial density profiles (i.e. variation in density with respect to channel height) for a fluid with state points $\rho^* = 0.8442$ and $T^* = 0.722$ in the shear-thinning regime of the flow and compare them with the profile at small strain-rates where shear-thinning has not yet set, see Fig. 6. At low strain-rates, we see that the fluid remains homogeneous and the spatial density is equivalent to the prescribed density of the fluid, with fluctuations within negligible limits. As the deformation rate increases, this leads to an increasingly saw-tooth profile that alludes to the formation of strings that are aligned in the

direction of flow, with the degree of alignment being proportional to deformation rate. The induced structural anisotropy results in a decrease in friction between fluid layers causing a drop in the shear stress and a corresponding decrease in fluid viscosity. We see that the development of the string-phase corresponds to the critical strain rate, $\dot{\gamma}_{cr}^{*} = 1.5$ which is the peak of the stress-deformation curve [35] at which a discontinuity forms due to the development of an ordering transition. Such a critical strain-rate above which an ordering transition occurs and the flow becomes unstable may also be predicted by the Loose-Hess stability criterion, which suggests that for $\dot{\gamma} > \dot{\gamma}_{cr}$ a velocity perturbation in the shear gradient direction can amplify a density perturbation along that direction [33]. The Reynolds number is $Re \approx 91$ which in the regime for the excitation of the first harmonic of the Fourier modes ($82 \leq Re \leq 107$) [8]. Consequently, we can expect some perturbations to grow as some eigenmodes do not dampen out with increasing shear rate, resulting in an ordering transition [34]. This is indeed the transition we see in Fig. 6c and Fig. 6d for $\dot{\gamma} = \dot{\gamma}_{cr}$ and $\dot{\gamma} > \dot{\gamma}_{cr}$, respectively. As a consequence, we see that the shear-thinning regime is in the unstable regime of the flow.

Another key indicator of this fact is the development of long range correlations in local density contrast as shown in Fig. 7. Since density perturbations vary the most in the direction of the shear gradient, we calculate the spatially-averaged density autocorrelation as

$$\langle \delta(t)\delta(\, t+s)\rangle = \frac{1}{N}\sum_{i=1}^{N} \delta(y_i, t)\delta(y_i, t+s) \tag{4.58}$$

where $i = 1\ to\ N$ represents the number of spatial slices of the domain in the y direction. Fig. 7a and Fig. 7b indicates that the local density fluctuations are essentially white noise in the linear regime of the flow. However, at the onset of shear-thinning, the local density fluctuations become correlated over a long-time period as shown in Fig. 7c and Fig. 7d. At small strain rates, the fluid remains homogeneous. Consequently, the density fluctuations resulting from molecular interactions are uncorrelated and distributed homogeneously throughout the fluid. At the onset of shear-thinning, molecules tend to align via the formation of string-

like structures oriented in the direction of the flow. This confines the density fluctuations to a particular layer in the direction of the flow thus leading to the development of correlations as they no longer homogeneously permeate throughout the fluid. Furthermore, these correlations take longer to die out with increasing strain rate as is evident by comparing Fig. 7c and Fig. 7d.

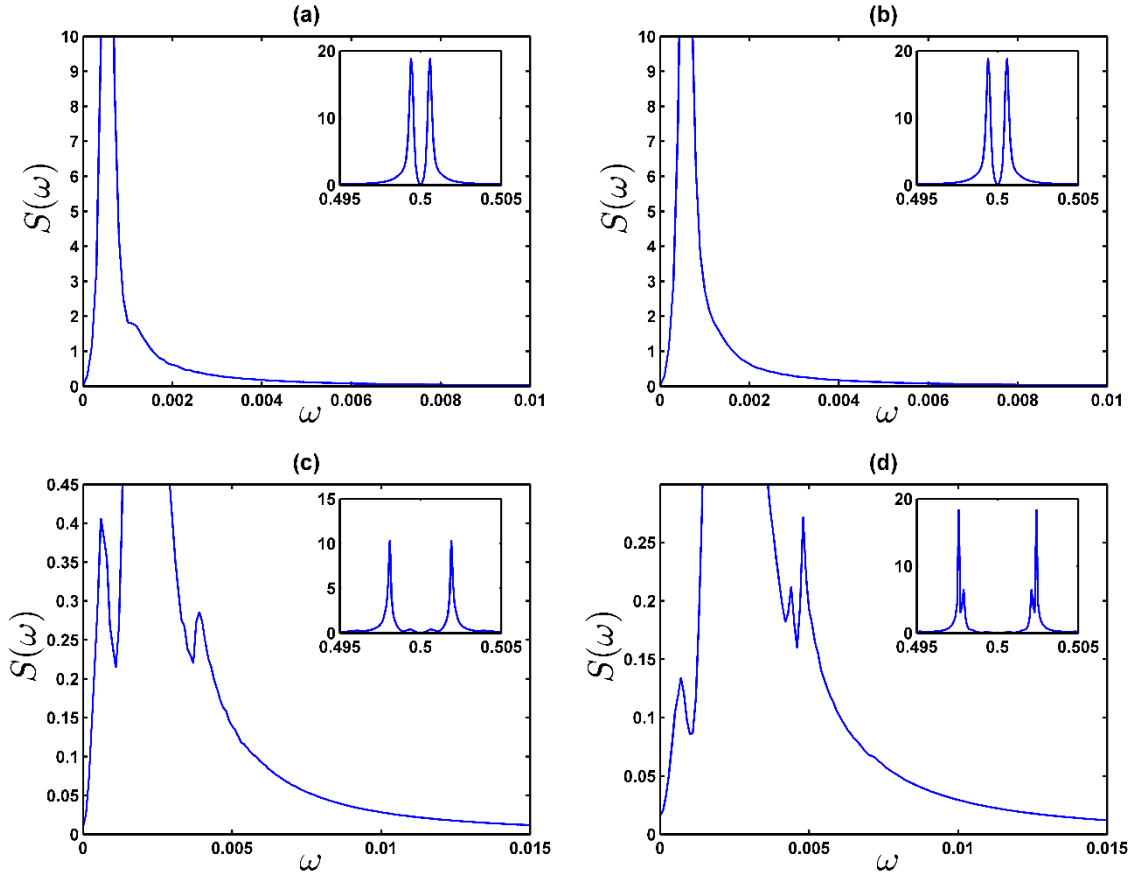

Fig. 9: Shear stress power spectral density (PSD) for the LJ fluid at the state point $(\rho^*, T^*) = (0.8442, 0.722)$ at (a) $\dot{\gamma}^* = 0.1$ (b) $\dot{\gamma}^* = 0.5$ (c) $\dot{\gamma}^* = 1.5$, and (d) $\dot{\gamma}^* = 2.5$. The top plots are for the linear regime and the bottom plots are for the nonlinear regime. The inset figures are the total PSD, while the outer plot zooms in to show the existence of additional frequencies, particularly in (c) and (d).

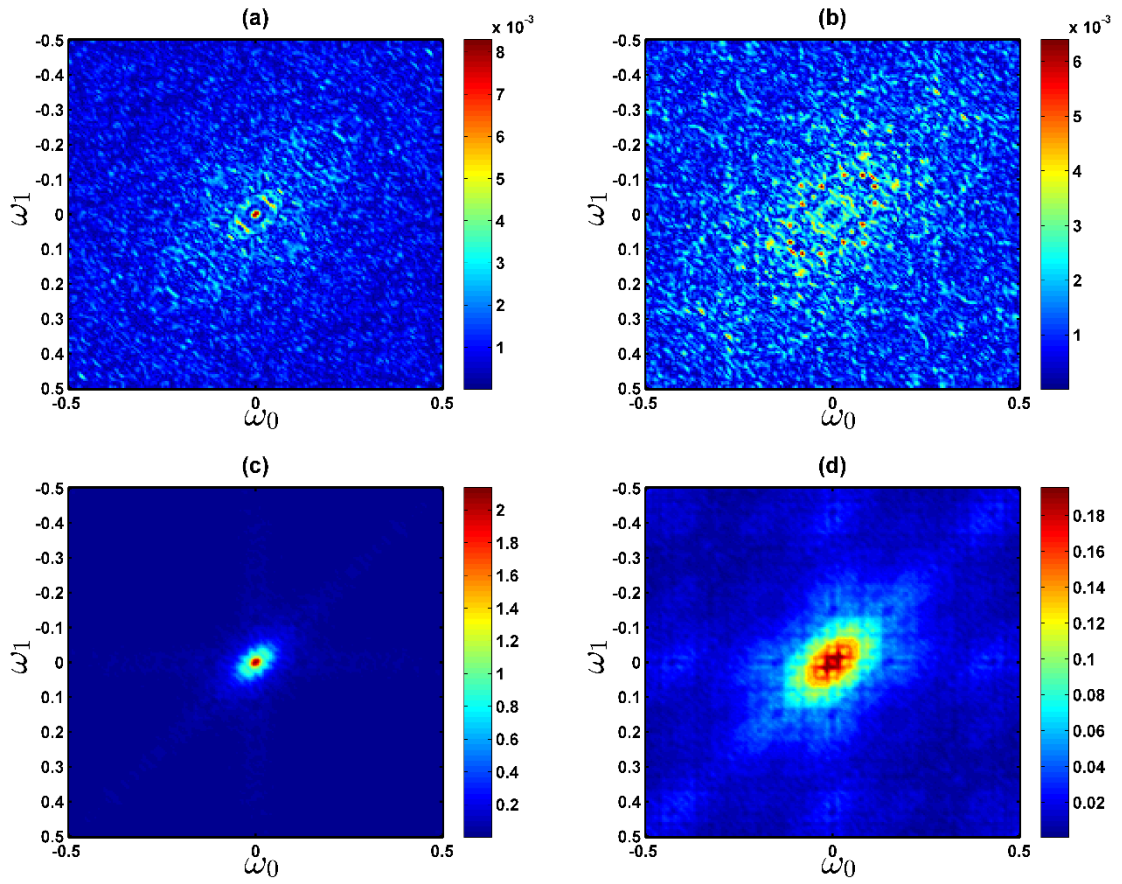

Fig. 10: Bispectrum magnitude $|B(\omega_0, \omega_1)|$ for the LJ fluid at the state point $(\rho^*, T^*) = (0.8442, 0.722)$ at (a) $\dot{\gamma}^* = 0.1$ (b) $\dot{\gamma}^* = 0.5$ (c) $\dot{\gamma}^* = 1.5$, and (d) $\dot{\gamma}^* = 2.5$.

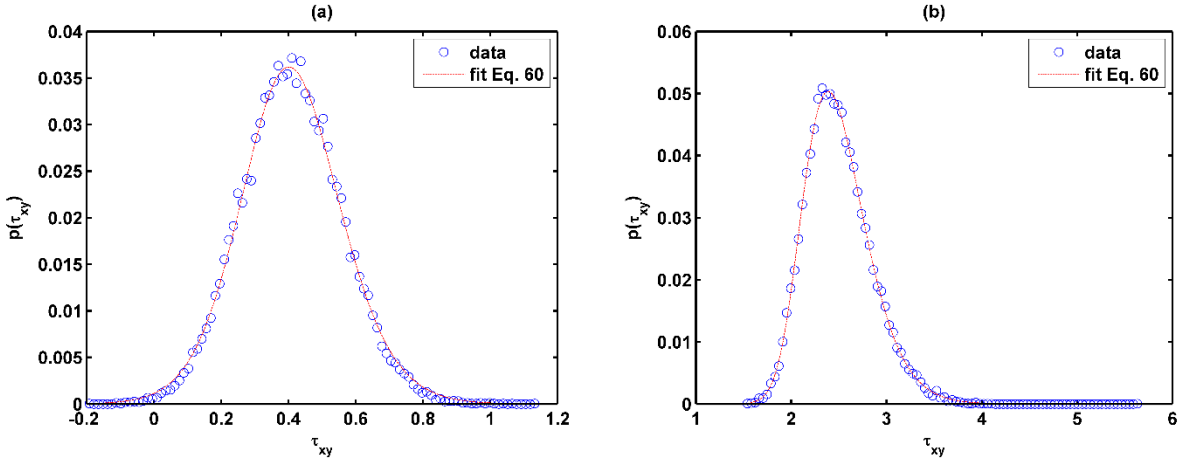

Fig. 11: Probability distribution of the shear stress, τ_{xy}, for (a) $\dot{\gamma}^* = 0.1$ and (b) $\dot{\gamma}^* = 1.5$ with the fit given by Eq. (4.52) in *red.*

Fig. 8 compares the time autocorrelation functions (ACFs) of the fluctuating component of the shear stress, $R(t)$. The microscopic formulation of the stress tensor [Eq. (4.32)] is linked to the peculiar velocities of the fluid particles. Fig. 8a shows that when the string phase is absent, the ACF decays to 0 in the long-time limit and is an indication of the homogeneity and isotropy of the fluid. The peak to peak times correspond well to $\theta^*/\dot{\gamma}^*$ where θ^* is the effective collision frequency of the particles [35]. Additionally, in this regime correlations are damped in proportion to the strain rate as illustrated in Fig. 8a and Fig. 8b. On the other hand, in the nonlinear regime alignment in the flow direction confines all interactions to the x streaming direction. In this regime, the peak to peak times correspond to $\dot{\gamma}^{*-1}$, since the strain-rate is much larger than the mean collision frequency of the molecules. Furthermore, once shear-thinning sets in, the correlations do not decay in the long-time limit and continue oscillating indefinitely, i.e. for the remaining duration of the simulation run, indicating the development of anisotropy in the fluid. These correlations get increasingly stronger with increasing strain rate, as shown in Fig. 8c and Fig. 8d. In particular, from Fig. 8d, we see that autocorrelation function decays in a manner consistent with the low strain behavior of the fluid ($0 \leq t^* < 2$), but after structural reordering occurs (at $t^* \geq 2$), the autocorrelation actually increases for a finite time before decaying slightly but not entirely dying out. The power spectral density (PSD) of the shear stress shown in Fig. 9 shows that, in the linear regime, fluctuations in the shear stress are confined to a narrow frequency range showing its narrow-band character. With increasing shear strain, additional frequencies are activated, as shown in Fig. 9c and Fig. 9d. These additional frequencies are estimated to correspond to the initiation of structural reordering within the fluid because some of the eigenmodes of the velocity perturbations do not decay.

This is further indicated by the bispectrum of the shear stress. Fig. 10 depicts the bispectrum for the LJ fluid in the linear and nonlinear regimes. The bispectrum of the shear stress, is the Fourier transform of the 3rd order cumulant function and is expressed in the frequency domain as

$$B(\omega_0, \omega_1) = \langle \tau_{12}(\omega_0)\tau_{12}(\omega_1)\tau_{12}(\omega_0 + \omega_1) \rangle \quad (4.59)$$

The bispectrum clearly indicates the degree of nonlinearity in the system and the degree of departure from a Gaussian system. In general, the application of an external strain rate results in system nonlinearities. However, for weak external fields, a linear approximation still holds as $|B(\omega_0, \omega_1)|$ is small. In such cases, a Gaussian approximation for the system is valid. On the other hand, from Fig. 10c and Fig. 10d, we see that the system possesses a significant degree of nonlinearity in the shear-thinning regime of the flow owing to molecular alignment, and thus is an indicator of the development of structural anisotropy. Furthermore, the bispectrum alludes to the development of quadratic phase coupling (QPC). In particular, we see that there are frequency components at $\omega_0 + \omega_1$. The bispectrum is often used to indicate the presence of quadratic nonlinearities in the system [65], [66]. Consequently, this alludes to the influence of quadratic terms in the perturbed quantities, which suggests a departure from linear perturbation theory. Additionally, non-gaussianity is a key feature indicative of flow instability and transition to the string phase. This substantiates the need for higher-order constitutive models that may be used in more advanced simulations for a variety of engineering systems.

Non-Gaussianity is also demonstrated by the probability density function of the shear stress shown in Fig. 11. Fig. 11 shows the probability distribution for the shear stress in the linear regime of the flow. It is approximately Gaussian and in good agreement with NEMD observations [39]. In addition, there is a non-zero albeit small probability that the shear stress can become negative. This implies the existence of system trajectories that violate the second law of thermodynamics. Additionally, the probabilistic nature of shear stress can have important consequences for system stability. For instance, although the Loose-Hess instability criterion, which quantifies instability by relating the shear-stress and normal stress components, holds in the average sense, there may be instances where an unstable flow might temporarily become stable owing to the probabilistic nature of the stress tensor, as negative shear stress increments can violate this instability criterion. The ordering transition at the critical strain rate also leads to a departure from a Gaussian

distribution. In this case, depicted in Fig. 11b, the probability density function becomes skewed and higher-order moments exist, which is also consistent with the observation made in the bispectrum of the shear stress. This suggests that the flow tends to be stable so long as it remains Gaussian. We also demonstrate that Eq. (4.57) is a suitable generalization to a Gaussian Approximation for the shear stress and is able to successfully model the system in the linear and nonlinear regimes by accounting for the existence of higher-order moments.

4.3.2 Effects of Temperature and Density

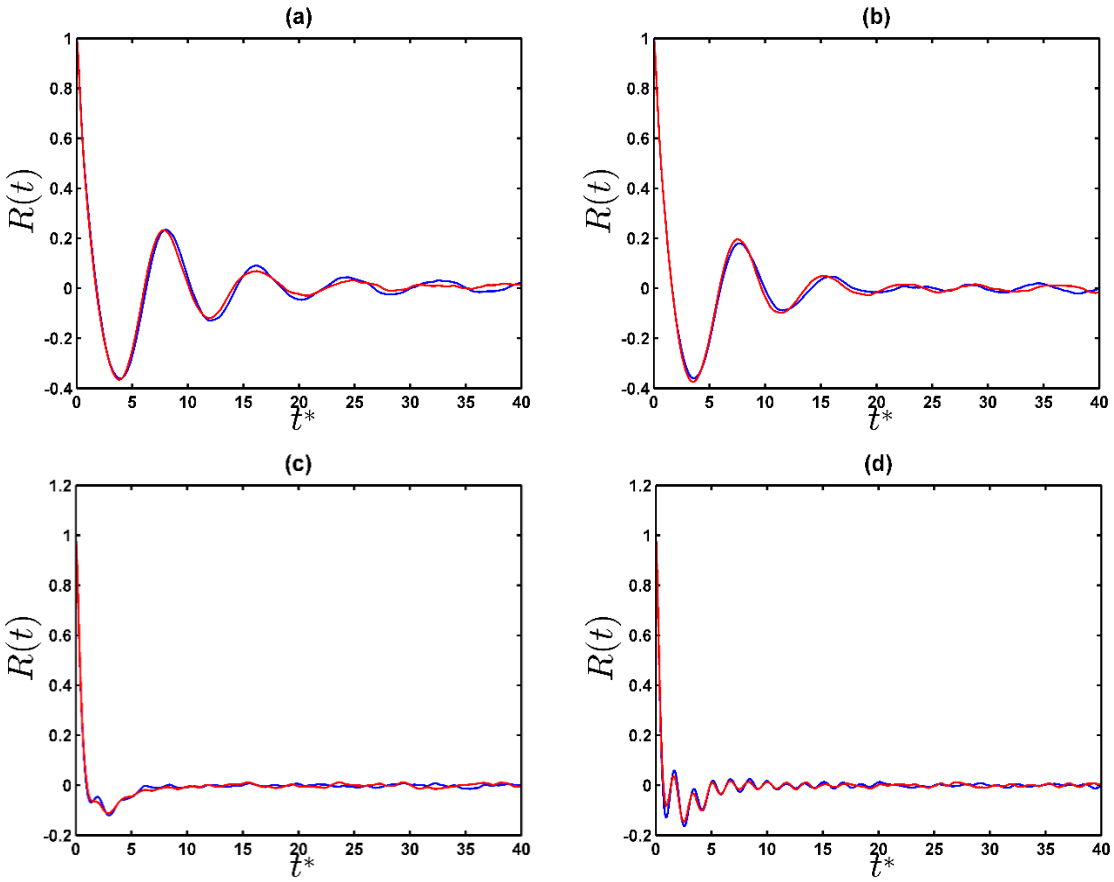

Fig. 12: Shear stress autocorrelation function for the LJ fluid at the state point $(\rho^*, T^*) = (0.8, 1.0)$ *(blue curve)* and $(\rho^*, T^*) = (0.8, 1.1)$ *(red curve)* at strain rates of (a) $\dot{\gamma}^* = 0.1$ (b) $\dot{\gamma}^* = 0.5$ (c) $\dot{\gamma}^* = 2.0$, and (d) $\dot{\gamma}^* = 2.5$.

To examine the effects of fluid temperature and density on the shear stress ACF, we study the LJ fluid at additional state points of $(\rho^*, T^*) = (0.6, 1.0), (0.6, 1.5), (0.8, 1.0)$ and $(0.8, 1.1)$. In this set, only the last two state

points exhibit shear thinning for the range of strain-rates considered. From the autocorrelation functions in Fig. 12 and Fig. 13, we see that in the linear regime of the flow, the temperature of the fluid increases the time period of the shear stress autocorrelations. This is particularly evident at the state points $(\rho^*, T^*) = (0.6, 1.0)$ and $(0.6, 1.5)$ in Fig. 13. Compared with $(\rho^*, T^*) = (0.8, 1.0)$ and $(0.8, 1.1)$, it would appear that the increase in the time period of the ACF is proportional to the increase in fluid temperature. Additionally, we also see that an increase in fluid density tends to cause molecular alignment at lower strain rates, as shown in Figs. Fig. 12c and Fig. 12d. For all the cases, in the linear regime of the flow, the strain rate acts as a damping parameter and causes the ACF to decay faster to 0.

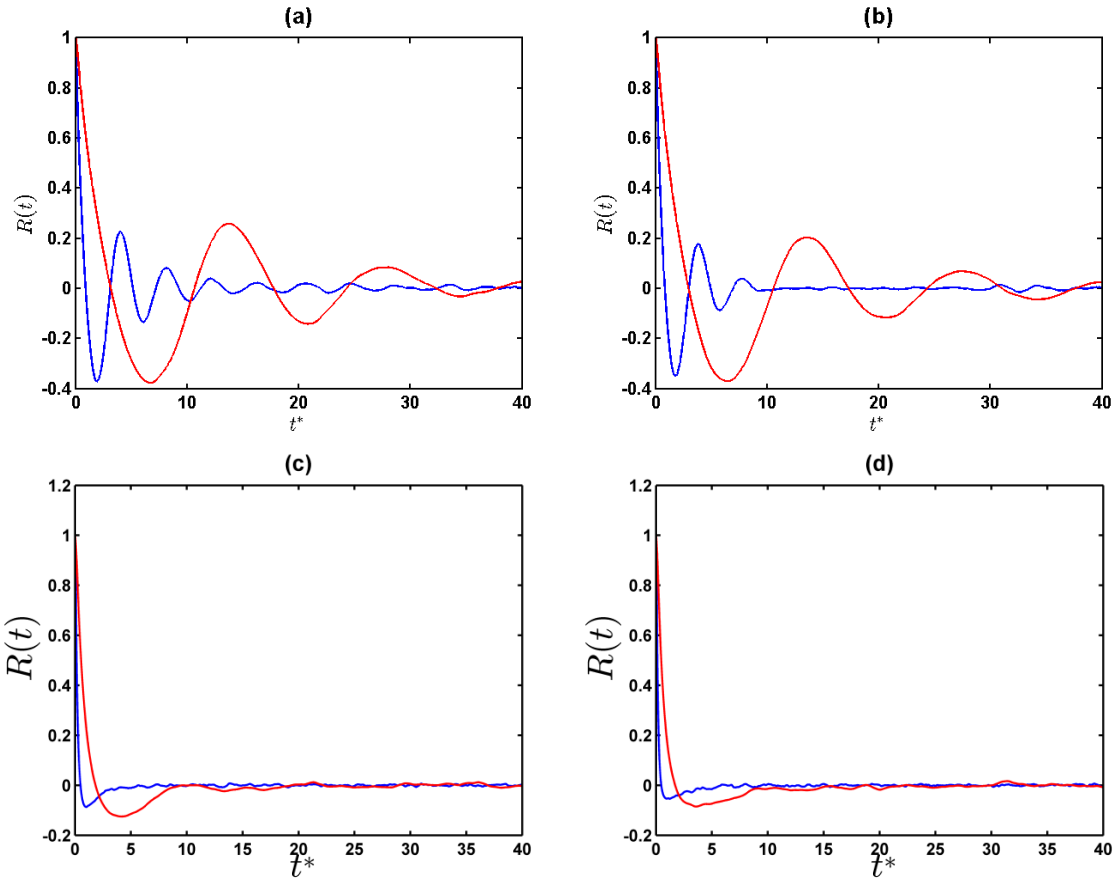

Fig. 13: Shear stress autocorrelation function for the LJ fluid at the state point $(\rho^*, T^*) = (0.6, 1.0)$ *(blue curve)* and $(\rho^*, T^*) = (0.6, 1.5)$ *(red curve)* at strain rates of (a) $\dot{\gamma}^* = 0.1$ (b) $\dot{\gamma}^* = 0.5$ (c) $\dot{\gamma}^* = 2.0$, and (d) $\dot{\gamma}^* = 2.5$.

By examining the PSDs of the corresponding ACFs in Fig. 14 and Fig. 15, we see that at a fluid density of $\rho^* = 0.8$, a higher temperature leads to a lower PSD value at the activated frequencies in the linear regime of the flow. From Fig. 14c and Fig. 14d, we see that multiple frequencies are activated at the onset of shear thinning. Additionally, we also see that an increase in fluid temperature delays the onset of shear-thinning. We infer that a higher fluid temperature leads to increased molecular activity, thus requiring a higher strain-rate to cause molecular alignment. Furthermore, at higher temperatures, the power at the activated frequencies seems to be more evenly distributed among the activated frequencies in the nonlinear shear thinning regime of the flow and is particularly evident in Fig. 14d.

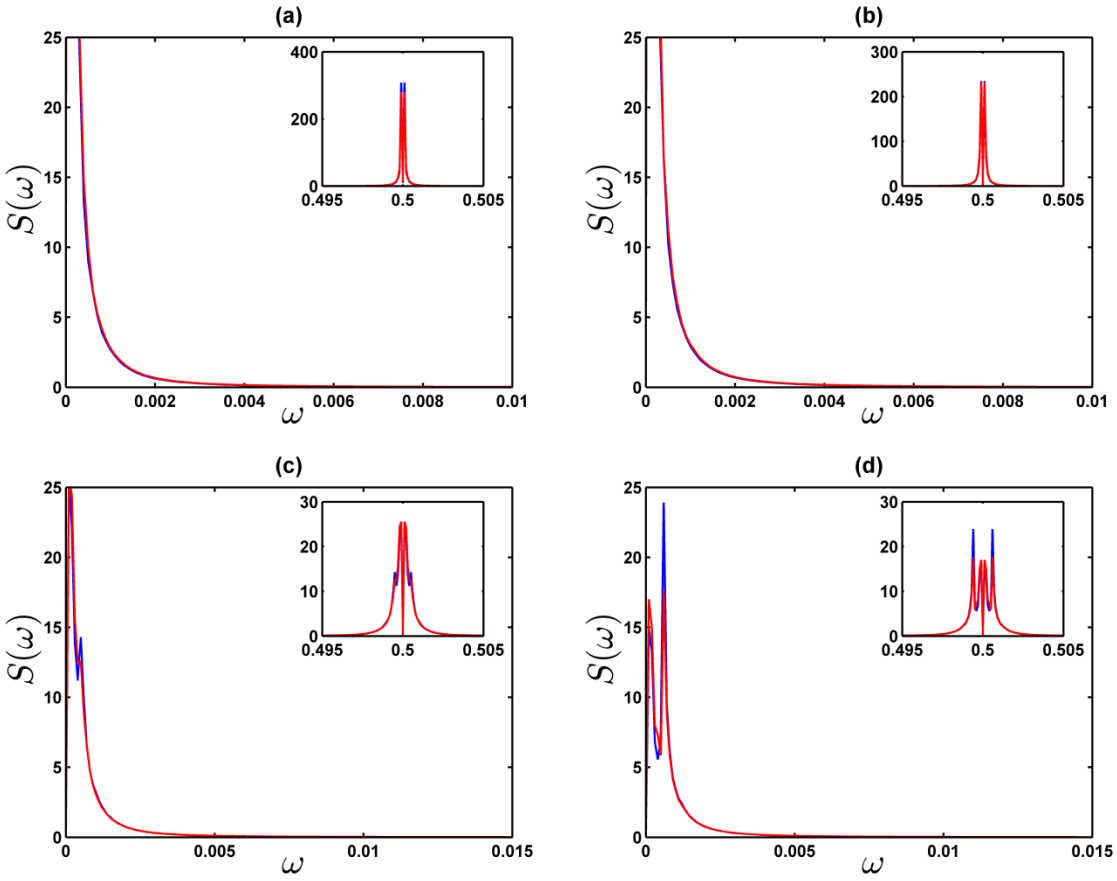

Fig. 14: Shear stress power spectral density (PSD) for the LJ fluid at the state point $(\rho^*, T^*) = (0.8, 1.0)$ *(blue curve)* and $(\rho^*, T^*) = (0.8, 1.1)$ *(red curve)* at strain rates of (a) $\dot{\gamma}^* = 0.1$ (b) $\dot{\gamma}^* = 0.5$ (c) $\dot{\gamma}^* = 2.0$, and (d) $\dot{\gamma}^* = 2.5$.

In contradistinction to this, at $\rho^* = 0.6$ in Fig. 15, we see that a higher temperature leads to a higher PSD value. At high strain rates, despite the range of activated frequencies being the same, the energy distribution across them is more uniform in the case of lower fluid temperature, as illustrated in Fig. 15c and Fig. 15d. Consequently, the shear stress behaves as a wide-band random process for low temperatures, and a narrow-band random process for high temperatures, at a given fluid density. In addition, we see that an increase in fluid density leads to a higher PSD value at a given strain rate.

In all cases, it is interesting to note that the shear stress autocorrelation function in the linear regime strongly matches an exponentially damped cosine wave that is able to accurately capture its narrow-band or wide-band characteristics. The ACF for the shear stress is expressed as [67]

$$\langle \sigma_{12}(s)\sigma_{12}(s+t)\rangle = R(t) = e^{-at}\cos(bt) \tag{4.60}$$

where a and b are fitting constants depending on the molecular parameters (i.e. ν^*, ρ^*, and T^*), and the lag t. The corresponding PSD (via the Fourier transform) is given as

$$S(\omega) = \frac{a}{\pi}\left[\frac{\omega^2 + a^2 + b^2}{\omega^4 + 2\omega^2(a^2 - b^2) + (a^2 + b^2)^2}\right] \tag{4.61}$$

The fitting is illustrated in Fig. 16. In particular, we note that Eq. (4.60) is able to accurately capture the ACF for a range of fluid state-points. This modeling ability is preserved for any range of strain-rates so long as shear-thinning has not set in, and the fluid continues to behave linearly. In the nonlinear regime, Eq. (4.60) breaks down and is no longer a suitable model owing to the activation of multiple frequencies.

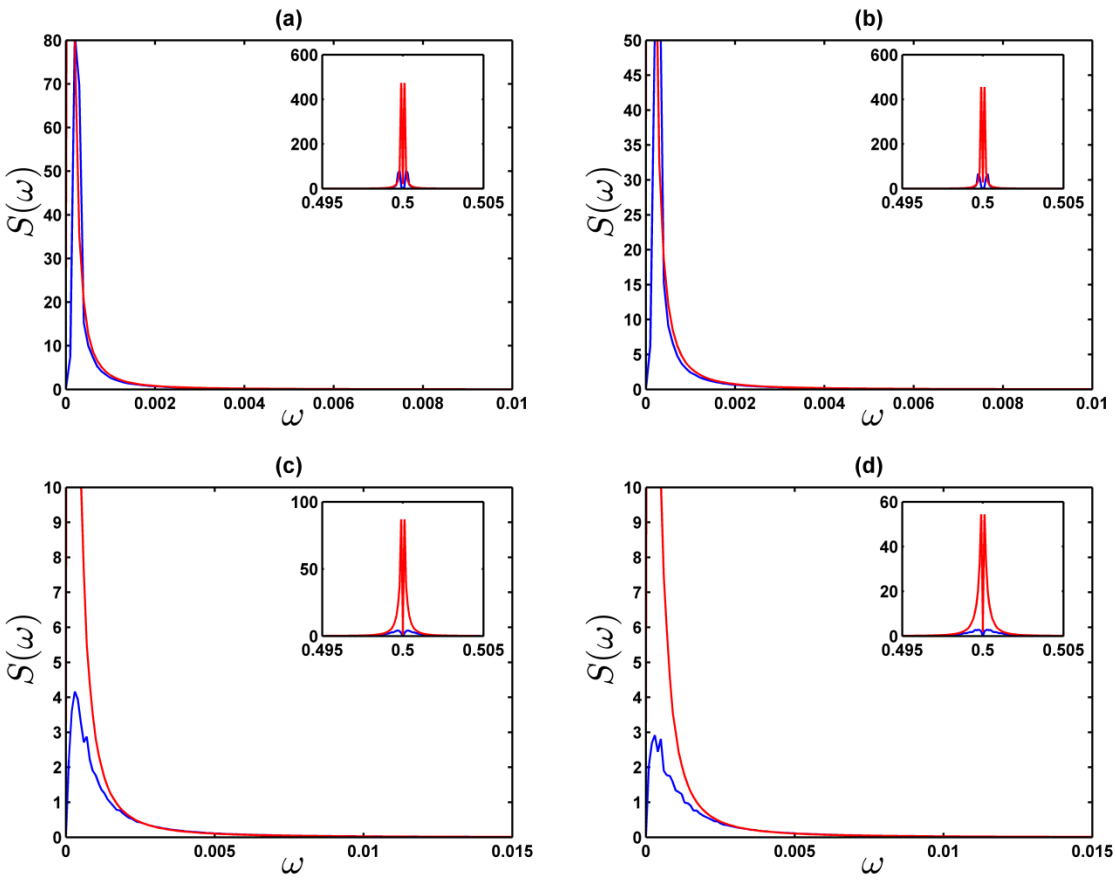

Fig. 15: Shear stress power spectral density (PSD) for the LJ fluid at the state point $(\rho^*, T^*) = (0.6, 1.0)$ *(blue curve)* and $(\rho^*, T^*) = (0.6, 1.5)$ *(red curve)* at strain rates of (a) $\dot{\gamma}^* = 0.1$ (b) $\dot{\gamma}^* = 0.5$ (c) $\dot{\gamma}^* = 2.0$, and (d) $\dot{\gamma}^* = 2.5$.

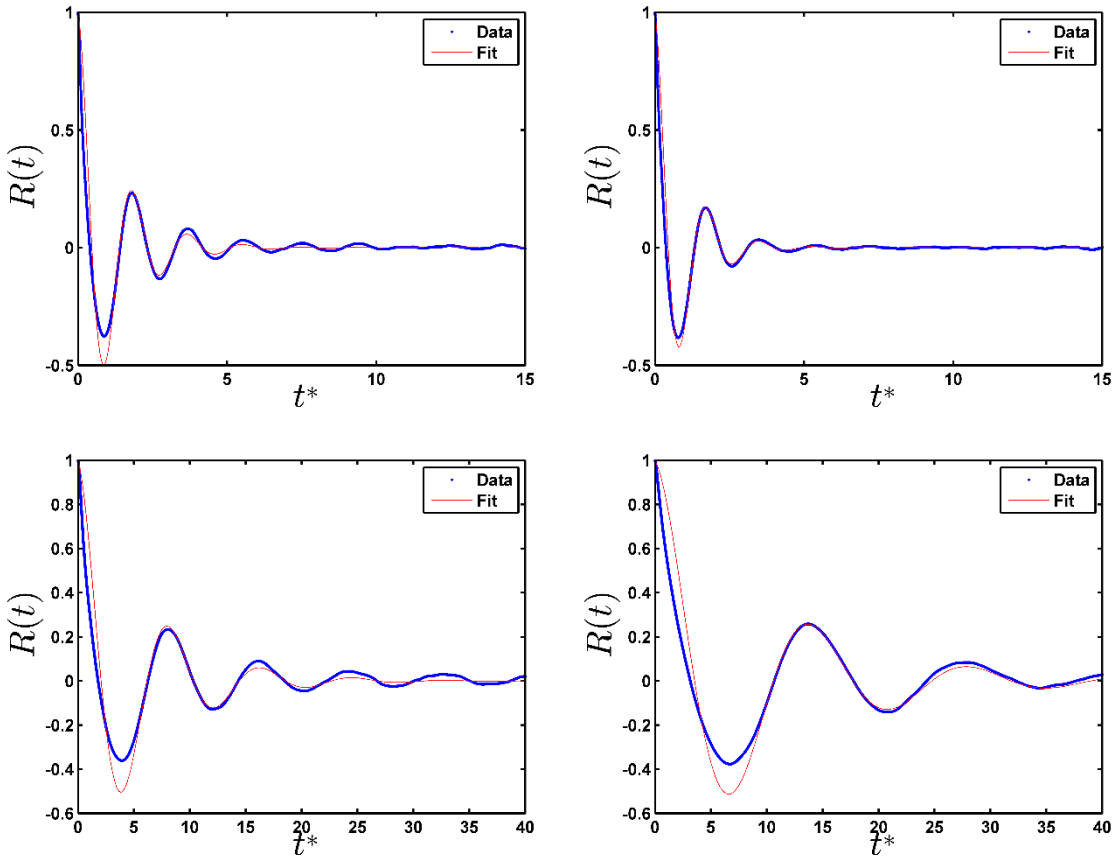

Fig. 16: Shear stress ACF (*blue*) and fit given by Eq. (8) *(red)* for the LJ fluid. The *top row* is at the state point $(\rho^*, T^*) = (0.8442, 0.722)$ and *bottom row* is at $(\rho^*, T^*) = (0.6, 1.5)$. The *left* column is at strain rate of $\dot{\gamma}^* = 0.1$ and the *right* column is $\dot{\gamma}^* = 0.5$.

4.4 Conclusion

The objectives of this study were to investigate the stochastic characteristics of an atomic fluid undergoing Couette flow. In Sec. 4.3.1 and 4.3.2, we demonstrated the connection between local density fluctuations and the shear stress and thus restricted our focus to these properties, and how changes in their statistical characteristics could be used to identify the critical shear rate at which planar Couette flow of an atomic fluid ceases to be stable. We explicitly show how fluctuations in shear stress drive density perturbations. Using the dissipation function, we relate entropy production to shear stress and obtain a stochastic partial differential equation. In the continuum limit, we recover a deterministic equation as statistical fluctuations in the shear stress die out. Driven by observations made

in NEMD simulations of Couette flow, we formulated a probability density function to describe the shear stress using the framework of information theory.

In general, there exists a critical shear rate at which the fluid undergoes an ordering transition from an amorphous phase to a ‘string’ phase in which particles align in the direction of the flow. This transition manifests as a saw-tooth profile in plots of the spatial density profile. The degree of alignment is proportional to the strain rate. To better understand the mechanism behind this transition and subsequently identify linear and nonlinear regimes of the flow, we examine the statistical characteristics of the local density contrast and the shear stress. By studying the autocorrelation function of the density perturbations, we find that in the linear regime or amorphous phase it is Gaussian noise. Above the critical strain rate, once the ordering transition sets in, correlations develop which indicate the development of internal structure within the fluid.

The shear stress is an additional indicator of the development of nonlinear phenomena in the system and can be used to identify the critical shear rate and determine the transition from the amorphous to the string phase. One such indicator of change is the autocorrelation function of the shear stress, which significantly changes between the linear and nonlinear flow regimes. The autocorrelation function does not decay entirely in the latter. By observing the power spectral density of the shear stress, there are additional frequencies activated in the nonlinear regime of the flow. These changes correspond quite well to the excitation of the first harmonic of Fourier modes. The bispectrum provides further insight into the nonlinearity of the flow by suggesting the existence of a quadratic phase coupling between eigenmodes. We also demonstrate how the probability distribution for the shear stress changes in the linear and nonlinear regimes of the flow. In the linear regime, the system is approximately Gaussian as it is amorphous. At the critical strain rate, the transition to a string phase introduces nonlinearities into the system that result in higher-order moments of the shear stress no longer being negligible. We show how the probability density function given in Eq. (4.57) is a more general approximation than a Gaussian one as it is not restricted to the linear flow regime

and is able to accurately model the response of the system regardless of the flow regime.

Finally, we see that the critical shear rate increases when the fluid density decreases or the temperature increases. Additionally, for an amorphous system, the autocorrelation function and the power spectral density are accurately described by an exponentially damped cosine function and its corresponding Fourier transform, respectively.

In summary, we have characterized the statistical nature of Couette flow via molecular dynamics. We have demonstrated how the density perturbations and the shear stress and their corresponding temporal and spectral moments can be used to identify the critical shear rate at which the ordering transition occurs, and subsequently when the flow instability sets in. Such insight is particularly useful in more complicated simulations, for instance in micro and nanofluidics, when the system under study requires a statistical treatment.

In Chapter 5, we will see how the fluctuation theorem (FT) naturally emerges as a stochastic forcing function in the mathematical generalization of the Reynolds-Orr equation to molecular and atomic fluids. Contrary to classical stability theory, we will illustrate that the perturbed kinetic energy does not decay monotonically. This phenomenon is governed by a Langevin-type equation (specifically an inequality), the moments of which yield insight into the critical Reynolds number at which flow instability sets in.

Chapter 5
Effects of Second Law Violations on the Hydrodynamic Stability of a Lennard-Jones Atomic Fluid

5.1 Introduction[3]

Simple atomic fluids are studied using non-equilibrium molecular dynamics (NEMD). These simulations typically use SLLOD dynamics where fictitious forces are added to the equations of motion [8] along with Lees–Edwards boundary conditions [32] to generate the desired shear gradient. In an early study of the stability of simple atomic fluids, Loose and Hess [33], [34] had formulated a stability theory to predict the critical shear rate at which steady-state planar Couette flow of an amorphous (no long-range spatial order) atomic fluid ceases to be stable. This theory is similar to the traditional linear stability analysis of the NS equation except that the linear constitutive thermodynamic relationship between the pressure and strain rate tensors is no longer assumed to be true. This critical strain-rate is characterized by the onset of shear-thinning and the strain-rate dependent structural re-ordering of fluid particles in the direction of the flow (i.e. the 'string'-phase). In this regime, steady-state Couette flow of an amorphous fluid is no longer possible. It is accompanied by a reduction in viscosity and a change in the slope of the stress-deformation rate response [35].

It will be shown that shear stress plays a central role in the stability of atomic fluids under shear. It is the stochastic forcing term in the dynamical equation for the kinetic energy of perturbations [41], and arises naturally from the fluctuation theorem (FT) [40] and the dissipation function [40], [42], [68]. The latter is a

[3] Adapted from: B. V. Raghavan and M. Ostoja-Starzewski, " On the Hydrodynamic Stability of a Lennard-Jones Molecular Fluid," *Journal of Statistical Physics*, vol. 177, pp. 61-77, 2019.

central concept in microscale theories and continuum thermomechanics and facilitates unifying phenomena in these two distinct length scales [43]. The FT explicitly allows for stochastic fluctuations in the shear stress that allow for instantaneous violations [39], [44], [45] of the classical Clausius-Duhem inequality of entropy production in the very small-scale limit. It demonstrates that despite the exponential stability of the perturbations, the stochastic contribution from the shear-stress can contribute to subcritical transient amplification of their kinetic energy.

We restrict ourselves to two-dimensional (2D) simulations be consistent with the simulations used to observe violations of the second law of thermodynamics and establish a method to identify the critical Reynolds number corresponding to string formation [6], [7], [8], [9], [34], [35], [43]. Although the 'string'-phase is an artifact of the thermostatting mechanism, it is an observable unstable structure that depends on the Reynolds number of the flow. Consequently, there exists a critical strain-rate above which the 'string'-phase instability manifests. The goal of this chapter is to provide a framework for estimating the critical Reynolds number at which the flow becomes unstable and examine the mechanisms responsible for the formation of strings.

5.2 Stability and Kinetic Energy Dissipation

To study the stability via the dissipation of kinetic energy in Couette flow, we derive the Reynolds-Orr equation for atomic fluids [69]. We begin by denoting the velocity field and pressure field as

$$\boldsymbol{u}(\boldsymbol{x},t) = \boldsymbol{u}^{\boldsymbol{C}} + \boldsymbol{v}'(\boldsymbol{x},t) \tag{5.1a}$$

$$p(\boldsymbol{x},t) = p + p'(\boldsymbol{x},t) \tag{5.1b}$$

where $\boldsymbol{u}^C = \mathbf{i}\dot{\gamma}y$ is the Couette flow velocity field from the Navier-Stokes equation. The individual fluid particle velocities fluctuate randomly about the mean flow velocity with a peculiar velocity given by $\boldsymbol{v}'(\boldsymbol{x},t) = \boldsymbol{u}(\boldsymbol{x},t) - \boldsymbol{u}^C$, So, we can consider a basic state as $(\boldsymbol{u}^C, p)$ and a perturbed state as $(\boldsymbol{u}^C + \boldsymbol{v}', p + p')$ to derive the evolution equations for the perturbation field.

The continuity equation yields

$$\frac{\partial \rho}{\partial t} + \nabla . \rho \boldsymbol{u} = 0 \tag{5.2}$$

where $\boldsymbol{u} = \boldsymbol{u^C} + \boldsymbol{v'}$ is the total velocity field. Additionally, we also have

$$\frac{\partial \rho}{\partial t} + \nabla . \rho \boldsymbol{u^C} = 0 \tag{5.3}$$

for the Couette flow field. If we subtract Eq. (5.3) from (5.2), we obtain

$$\frac{\partial \rho}{\partial t} + \nabla . \rho (\boldsymbol{u^C} + \boldsymbol{v'}) - \left[\frac{\partial \rho}{\partial t} + \nabla . \rho \boldsymbol{u^C}\right] = 0 \tag{5.4}$$

which for an incompressible flow yields

$$\nabla . \rho \boldsymbol{v'} = 0 \Longrightarrow \nabla . \boldsymbol{v'} = 0 \tag{5.5}$$

The flow is subjected to Lees-Edwards periodic boundary conditions, on account of which the fluctuating velocity field is subject to periodic boundary conditions of the form

$$\begin{aligned} v_x'(y = L_y, t) &= v_x'(y = 0, t) + \dot{\gamma} L_y, \\ v_y'(y = L_y) &= v_y'(y = 0), \\ v_z'(y = L_y) &= v_z'(y = 0) = 0 \end{aligned} \tag{5.6}$$

The macroscopic definition for the isothermal incompressible fluid flow is given by the Navier-Stokes equation,

$$\rho_0 \left[\frac{\partial \boldsymbol{v}}{\partial t} + \boldsymbol{v} . \nabla \boldsymbol{v}\right] = \eta \nabla^2 \boldsymbol{v} - \nabla p + \rho_0 \boldsymbol{b} \tag{5.7}$$

Considering perturbations to the velocity and pressure of the form in (1) and noting that $\boldsymbol{u}^C = \boldsymbol{u}(\boldsymbol{x}, t)$ is a solution of Eq. (5.7), we can substitute the perturbed velocity field in (5.7) and subtract from the unperturbed version to obtain the equations for the perturbed velocity field as

$$\rho_0 \left[\frac{\partial \boldsymbol{v}'}{\partial t} + \boldsymbol{v}'.\nabla \boldsymbol{v}'\right] = \eta \nabla^2 \boldsymbol{v}' - \nabla p' - \rho_0 \boldsymbol{v}'.\nabla \boldsymbol{u}(\boldsymbol{r}) - \rho_0 \boldsymbol{u}(\boldsymbol{r}).\nabla \boldsymbol{v}' \tag{5.8}$$

Dividing by ρ_0 we obtain,

$$\left[\frac{\partial \boldsymbol{v}'}{\partial t} + \boldsymbol{v}'.\nabla \boldsymbol{v}'\right] = \nu \nabla^2 \boldsymbol{v}' - \boldsymbol{v}'.\nabla \boldsymbol{u}(\boldsymbol{r}) - \boldsymbol{u}(\boldsymbol{r}).\nabla \boldsymbol{v}' - \frac{1}{\rho_0}\nabla p' \tag{5.9}$$

For Couette flow, Eq. (5.9) can be simplified further as

$$\frac{\partial \boldsymbol{v}'}{\partial t} = -\boldsymbol{v}'.\nabla \boldsymbol{v}' + \nu \nabla^2 \boldsymbol{v}' - \dot{\gamma} y \partial_x v' - \mathbf{i}\dot{\gamma} v_y - \frac{1}{\rho_0}\nabla p' \tag{5.10}$$

We can define the kinetic energy of the perturbations as

$$K(t) = \frac{1}{2}\rho_0 \int_V \|\boldsymbol{v}'(\boldsymbol{x}, t)\|^2 dV \tag{5.11}$$

and its time evolution as

$$\frac{d}{dt}K(t) = \rho_0 \int_V \boldsymbol{v}'(\boldsymbol{x}, t).\, \partial_t \boldsymbol{v}'(\boldsymbol{x}, t) dV \tag{5.12}$$

Using Eq. (5.10) in (5.12) for the term $\partial_t \boldsymbol{v}'(\boldsymbol{x}, t)$, where ∂_t is the partial derivative with respect to time, and noting that $\nabla \boldsymbol{u}(\boldsymbol{r}) = \boldsymbol{\epsilon}$, we obtain

$$\frac{d}{dt}K(t) = \rho_0 \int_V \boldsymbol{v}'.[\nu \nabla^2 \boldsymbol{v}' - \nabla p' - \boldsymbol{v}'.\boldsymbol{\epsilon} - \boldsymbol{u}(\boldsymbol{r}).\nabla \boldsymbol{v}' - \boldsymbol{v}'.\nabla \boldsymbol{v}']dV \tag{5.13}$$

The second term is 0 since there are no spatial variations in the perturbed pressure field (i.e. $p' = \rho k_B T = constant$) and owing to the periodicity of the simulation domain. For the last term, we have

$$-\int_V \boldsymbol{v}'.[\boldsymbol{v}'.\nabla \boldsymbol{v}']dV = -\int_V \nabla.\left(\frac{1}{2}\boldsymbol{v}'\|\boldsymbol{v}'\|\right)dV \tag{5.14}$$

Applying the divergence theorem to the right-hand-side of Eq. (5.14) and expanding yields

$$-\int_V \nabla.\left(\frac{1}{2}\boldsymbol{v}'\|\boldsymbol{v}'\|\right)dV = -\int_{\partial V}\|\boldsymbol{v}'\|\boldsymbol{v}'.\boldsymbol{n}\,dS \tag{5.15}$$

where $\boldsymbol{n}$ is the surface normal to the simulation domain (namely, the periodic bounding box). Expanding Eq. (5.15) gives

$$\begin{aligned}
&-\int_{\partial V}\|\boldsymbol{v}'\|\boldsymbol{v}'.\boldsymbol{n}\,dS \\
&= -\left[\int_{top}\|\boldsymbol{v}'\|\{\begin{bmatrix}v_x'(0,t)+\dot{\gamma}L_y & v_y'(L_y,t)\end{bmatrix}\begin{pmatrix}0\\1\end{pmatrix}\}dxdz\right. \\
&+\int_{bottom}\|\boldsymbol{v}'\|\{\begin{bmatrix}v_x'(0,t) & v_y'(0,t)\end{bmatrix}\begin{pmatrix}0\\-1\end{pmatrix}\}dxdz \\
&+\int_{left}\|\boldsymbol{v}'\|\{\begin{bmatrix}v_x'(0,t) & v_y'(0,t)\end{bmatrix}\begin{pmatrix}-\cos[\theta(t)]\\-\sin[\theta(t)]\end{pmatrix}\}dydz \\
&\left.+\int_{right}\|\boldsymbol{v}'\|\{\begin{bmatrix}v_x'(L_x,t) & v_y'(L_x,t)\end{bmatrix}\begin{pmatrix}\cos[\theta(t)]\\\sin[\theta(t)]\end{pmatrix}\}\;dydz\right] = 0
\end{aligned} \tag{5.16}$$

where $\theta(t) = \pi/2 - \tan^{-1}(2\dot{\gamma}t)$ [8]. We now simplify the expression for the special case of uniform shear flow using $\boldsymbol{u}(\boldsymbol{x},t) = \boldsymbol{i}\dot{\gamma}y \Rightarrow \boldsymbol{u}(\boldsymbol{x},t) = \begin{pmatrix}u_x & u_y & u_z\end{pmatrix} = \begin{pmatrix}\dot{\gamma}y & 0 & 0\end{pmatrix}$

$$\frac{d}{dt}K(t) = \rho_0\int_V \boldsymbol{v}'.\left[\nu\nabla^2\boldsymbol{v}' - \hat{\boldsymbol{i}}v_y'\dot{\gamma} - \dot{\gamma}.\partial_x\boldsymbol{v}'\right]dV \tag{5.17}$$

where **i** is the unit vector, y is the channel height, and $\dot{\gamma} = \partial u_x/\partial y$ is the strain rate to track the evolution of the perturbations, we apply the Lees-Edwards periodic boundary conditions and calculate term-by-term in the integral in Eq. (5.17). Owing to the periodicity of the simulation domain in the x-direction and assuming it to be of infinite length, we can take $\partial_x\boldsymbol{v}' = 0$. Applying the divergence theorem to the first term in the integral we have,

$$\int_V \boldsymbol{v}'.[\nabla^2\boldsymbol{v}']dV = \int_V [\boldsymbol{\nabla}.(\boldsymbol{v}'.\boldsymbol{\nabla}\boldsymbol{v}') - (\boldsymbol{\nabla}\boldsymbol{v}'):(\boldsymbol{\nabla}\boldsymbol{v}')dV \tag{5.18}$$

Eq. (5.18) can be rewritten as

$$\int_V \boldsymbol{v}'.[\nabla^2\boldsymbol{v}']dV = \int_{\partial V}(\boldsymbol{v}'.\boldsymbol{\nabla}\boldsymbol{v}').\hat{\boldsymbol{n}}\,dS - \int_V \|\boldsymbol{\nabla}\boldsymbol{v}'\|^2 dV \tag{5.19}$$

Applying the boundary conditions in the first integral in Eq. (5.19) yields

$$\begin{aligned}
&\int_{\partial V}(\boldsymbol{v}'.\boldsymbol{\nabla}\boldsymbol{v}').\hat{\boldsymbol{n}}\,dS \\
&= \int_{top}\begin{bmatrix}v'_x(0,t)+\dot{\gamma}L_y & v'_y(L_y,t)\end{bmatrix}\begin{bmatrix}v'_{x,x} & v'_{x,y}\\ v'_{y,x} & v'_{y,y}\end{bmatrix}\begin{pmatrix}0\\1\end{pmatrix}dxdz \\
&+ \int_{bottom}\begin{bmatrix}v'_x(0,t) & v'_y(0,t)\end{bmatrix}\begin{bmatrix}v'_{x,x} & v'_{x,y}\\ v'_{y,x} & v'_{y,y}\end{bmatrix}\begin{pmatrix}0\\-1\end{pmatrix}dxdz \\
&+ \int_{left}\begin{bmatrix}v'_x(0,t) & v'_y(0,t)\end{bmatrix}\begin{bmatrix}v'_{x,x} & v'_{x,y}\\ v'_{y,x} & v'_{y,y}\end{bmatrix}\begin{pmatrix}-\cos[\theta(t)]\\-sin[\theta(t)]\end{pmatrix}dydz \\
&+ \int_{right}\begin{bmatrix}v'_x(L_x,t) & v'_y(L_x,t)\end{bmatrix}\begin{bmatrix}v'_{x,x} & v'_{x,y}\\ v'_{y,x} & v'_{y,y}\end{bmatrix}\begin{pmatrix}\cos[\theta(t)]\\sin[\theta(t)]\end{pmatrix}dydz
\end{aligned} \tag{5.20}$$

Simplifying Eq. (5.20) yields

$$\int_V \boldsymbol{v}'.[\nabla^2\boldsymbol{v}']dV = \dot{\gamma}L_y\int_{\partial V(y=L)}\partial_y v'_x dxdz - \int_V \|\boldsymbol{\nabla}\boldsymbol{v}'\|^2 dV \tag{5.21}$$

We note that $\partial_y v'_x = \sigma'_{xy}(t)/\eta$ is the time-dependent fluctuating component of the shear-stress [43]. Therefore, we obtain

$$\int_V \boldsymbol{v}'.[\nabla^2\boldsymbol{v}']dV = \frac{\dot{\gamma}L_y\sigma'_{xy}(t)L_xL_z}{\eta} - \int_V \|\boldsymbol{\nabla}\boldsymbol{v}'\|^2 dV \tag{5.22}$$

Thus, we have

$$\int_V \boldsymbol{v}'.[\nabla^2\boldsymbol{v}']dV = \frac{\dot{\gamma}\sigma'_{xy}(t)V}{\eta} - \int_V \|\boldsymbol{\nabla}\boldsymbol{v}'\|^2 dV \tag{5.23}$$

Interestingly, the term $\dot{\gamma}\sigma'_{xy}(t)V$ is the stochastic component of the dissipation function $\Omega_t(\mathbf{\Gamma})$ that is the foundation of the FT. For the second term in the integral in (5.17), we have

$$\int_V \boldsymbol{v}'.\left[\hat{\boldsymbol{\imath}}v'_y\right]dV = \int_V v'_x v'_y dV \tag{5.24}$$

which yields

$$\begin{aligned} &\frac{1}{2}\rho_0 \frac{d}{dt}\int_V \|\boldsymbol{v}'(\boldsymbol{x},t)\|^2 dV \\ &= \dot{\gamma}\sigma'_{xy}(t)V - \eta\int_V \|\boldsymbol{\nabla v}'\|^2 dV - \rho_0\dot{\gamma}\int_V v'_x v'_y dV \end{aligned} \tag{5.25}$$

We now apply the Poincaré inequality [41] to Eq. (5.25) to obtain[4,5]

$$\begin{aligned} &\frac{d}{dt}\left(\frac{1}{2}\rho_0\int_V \|\boldsymbol{v}'(\boldsymbol{x},t)\|^2 dV\right) \\ &\qquad \leq \dot{\gamma}\int_V \sigma'_{xy}(t)dV \\ &\qquad -\left(\frac{\eta\pi^2}{L_y^2} - \frac{\rho_0\dot{\gamma}}{2}\right)\times\frac{2}{\rho_0}\left(\frac{1}{2}\rho_0\int_V \|\boldsymbol{v}'(\boldsymbol{x},t)\|^2 dV\right) \end{aligned} \tag{5.26}$$

Bearing in mind Eq. (5.11), we simplify Eq. (5.26) to obtain

$$\frac{d}{dt}K(t) \leq -\left(\frac{2\eta\pi^2}{\rho_0 L_y^2} - \dot{\gamma}\right)K(t) + \dot{\gamma}\sigma'_{xy}(t)V \tag{5.27}$$

When Eq. (5.27) is written with the equality sign, it is a stochastic ordinary differential equation, i.e. a Langevin equation for $K(t)$ in the presence of random

[4] *Let D be a regular, bounded region in $\mathbb{E}^3$. Then there is a scalar constant $\lambda > 0$, depending only on D, with the property $\int_D |\boldsymbol{w}|^2 dV_{\boldsymbol{x}} \leq \lambda \int_D \nabla\boldsymbol{w}:\nabla\boldsymbol{w} dV_{\boldsymbol{x}}$ for all smooth vector fields $\boldsymbol{w}$ satisfying $\boldsymbol{w} = \mathbf{0}$ on ∂D.*

[5] Suppose $f(y)$ is a (smooth enough) function on $y \in [0,h]$ and $f(0) = 0 = f(h)$. Then, $\|f\|^2 = \int_0^h [f(y)]^2 dy \leq \frac{\pi^2}{h^2}\int_0^h [f'(y)]^2 dy = \frac{\pi^2}{h^2}\|f'\|^2$.

noise. The first term is the conventional deterministic continuum result, and the second term is the stochastic modification owing to random molecular motion that has been introduced due to the FT. As a result, Eq. (5.27) can be written as

$$\frac{d}{dt}K(t) \leq -\left(\frac{2\eta\pi^2}{\rho_0 L_y^2} - \dot{\gamma}\right)K(t) + S(t) \tag{5.28}$$

Where $S(t)$ is the total volumetric entropy production, which acts as a stochastic forcing term in Eq. (5.28) [40]. In this manner, the FT acts as a bridge between classical continuum scales and the microscopic scale. The solution to the above relation implies the condition

$$K(t) \leq e^{-\left(\frac{2\eta\pi^2}{\rho_0 L_y^2} - \dot{\gamma}\right)t}K(0) + \dot{\gamma}V\int_0^t e^{-\left(\frac{2\eta\pi^2}{\rho_0 L_y^2} - \dot{\gamma}\right)(t-s)}\sigma'_{xy}(s)ds \tag{5.29}$$

5.3 Results and Discussion

5.3.1 Lower Bound on the Critical Reynolds Number

Alternatively, the relation in Eq. (5.28) can be written for the magnitude of the fluctuations ($v^2 = \|\mathbf{v}\|^2$) as

$$\frac{d}{dt}\|\mathbf{v}\|^2 + \frac{\|\mathbf{v}\|^2}{\tau_r} \leq \frac{\eta\dot{\gamma}}{\rho_0}\sigma'_{xy}(t) \tag{5.30}$$

where $\tau_r = 1/\left(\frac{2\eta\pi^2}{\rho_0 L_y^2} - \dot{\gamma}\right)$. The statistical mean of Eq. (5.30) is

$$\langle\|\mathbf{v}\|_t^2\rangle \leq \langle\|\mathbf{v}\|_0^2\rangle e^{-t/\tau_r} \tag{5.31}$$

where $\|\mathbf{v}\|_0^2$ is $\|\mathbf{v}\|_t^2$ at $t = 0$ where we assumed $\langle\sigma'_{xy}(t)\rangle = 0$. The variance of (5.30) is given by

$$s_t^2 \leq \frac{\eta^2\dot{\gamma}^2 g_{\sigma'}\tau_r}{\rho_0^2}(1 - e^{-2t/\tau_r}) \tag{5.32}$$

where $g_{\sigma\prime} = \int_0^t \langle \sigma'_{xy}(0)\sigma'_{xy}(s)\rangle ds = k_B T\eta$ from the Green-Kubo relation for viscosity [10] arising from linear-response theory, T is the fluid temperature, and k_B is the Boltzmann constant. As $t \to \infty$, using the definition of the variance and under the assumption of Maxwell dynamics (where the motion of the fluid molecules is described probabilistically by the Maxwell-Boltzmann distribution),

$$s^2_{t\to\infty} = \langle (v^2)^2\rangle - \langle v^2\rangle^2 = \langle v^4\rangle - \langle v^2\rangle^2 \leq \frac{\eta^2\dot{\gamma}^2 g_{\sigma\prime}\tau_r}{\rho_0^2} \tag{5.33}$$

The left-hand side of Eq. (5.33) can be simplified as

$$s^2_{t\to\infty} = \langle v^2\rangle^2 \left[\frac{\langle v^4\rangle}{\langle v^2\rangle^2} - 1\right] \tag{5.34}$$

where $\langle v^2\rangle^2 = 9v_p^4/4$ with v_p as the most probable speed of the Maxwell-Boltzmann distribution. We define the excess kurtosis of the Maxwell-Boltzmann distribution as $\kappa = \langle v^4\rangle/\langle v^2\rangle^2 - 3$. Then, the variance can be rewritten as

$$s^2_{t\to\infty} = \frac{9v_p^4}{4}[\kappa + 2] \tag{5.35}$$

Substituting Eq. (5.35) in Eq. (5.33), and using the definition of τ_r, we obtain

$$\frac{9v_p^4}{4}[\kappa + 2] \leq \frac{\eta^3\dot{\gamma}^3 k_B T}{\rho_0^2}\left(\frac{2\pi^2}{Re} - 1\right) \tag{5.36}$$

where $Re = \rho_0\dot{\gamma}L_y^2/\eta$ is the Reynolds number. Using the ideal gas relation[6] $P = \rho k_B T$, and considering pressure to be compressive, and $\sigma_{xy} = \eta\dot{\gamma}$, we have

$$\frac{9v_p^4}{4}[\kappa + 2] \leq \frac{\eta^3\dot{\gamma}^3\rho_0 k_B T}{\rho_0^3}\left(\frac{2\pi^2}{Re} - 1\right) = -\frac{\sigma_{xy}^3 P}{\rho_0^3}\left(\frac{2\pi^2}{Re} - 1\right) \tag{5.37}$$

[6] *In the specific case of Couette flow of fluid whose particles interact via the Lennard-Jones potential, the influence of the particle interactions on the transport properties of the fluid is weak even in states far from equilibrium* [74]. *Hence, the reason why the ideal gas equation is a reasonable approximation in this case.*

Rearranging Eq. (5.37), we obtain

$$\frac{9}{4Pv_p^2}[\kappa+2] \leq -\left(\frac{2\pi^2}{Re}-1\right)\left[\frac{\sigma_{xy}}{\rho_0 v_p^2}\right]^3 \tag{5.38}$$

The term $\sigma_{xy}/\rho_0 v_p^2$ is related to the hydraulic friction factor $f = a\sigma_{xy}/\rho_0 v_p^2$ where a is a constant depending on the type of f used (Fanning, Darcy, Stanton, etc). Using f in Eq. (5.38) yields Table 2.

$$\frac{9}{4Pv_p^2}[\kappa+2] \leq -\left(\frac{2\pi^2}{Re}-1\right)\left[\frac{f}{a}\right]^3 \tag{5.39}$$

Now, applying the relationship $f \sim b/Re$, where b is a constant once again depending on the definition used in Eq. (5.31),

$$\frac{9}{4Pv_p^2}[\kappa+2] \leq -\left(\frac{2\pi^2}{Re}-1\right)\left[\frac{8}{Re}\right]^3 \tag{5.40}$$

where factor 8 is the ratio b/a. For the Maxwell-Boltzmann distribution, $\kappa = 0.1082$ and $v_p = \sqrt{2RT/M}$ where $R = 8.314\ \mathrm{J/K.mol}$, and M is the molar mass of the fluid. Rearranging and simplifying Eq. (5.40) yields the quartic inequality

$$-\left(\frac{5.572\times10^{-4}M}{PT}\right)Re^4 + Re - 2\pi^2 \geq 0 \tag{5.41}$$

Under RTP conditions (i.e. $P = 101.325kPa, T = 300K$) we obtain

$$-1.833\times10^{-8}MRe^4 + Re - 2\pi^2 \geq 0 \tag{5.42}$$

Eq. (5.42) can be solved (numerically or graphically as in Fig. 1) for different gases to yield a fluid dependent Reynolds number that governs the transition to turbulence as shown in Table 2.

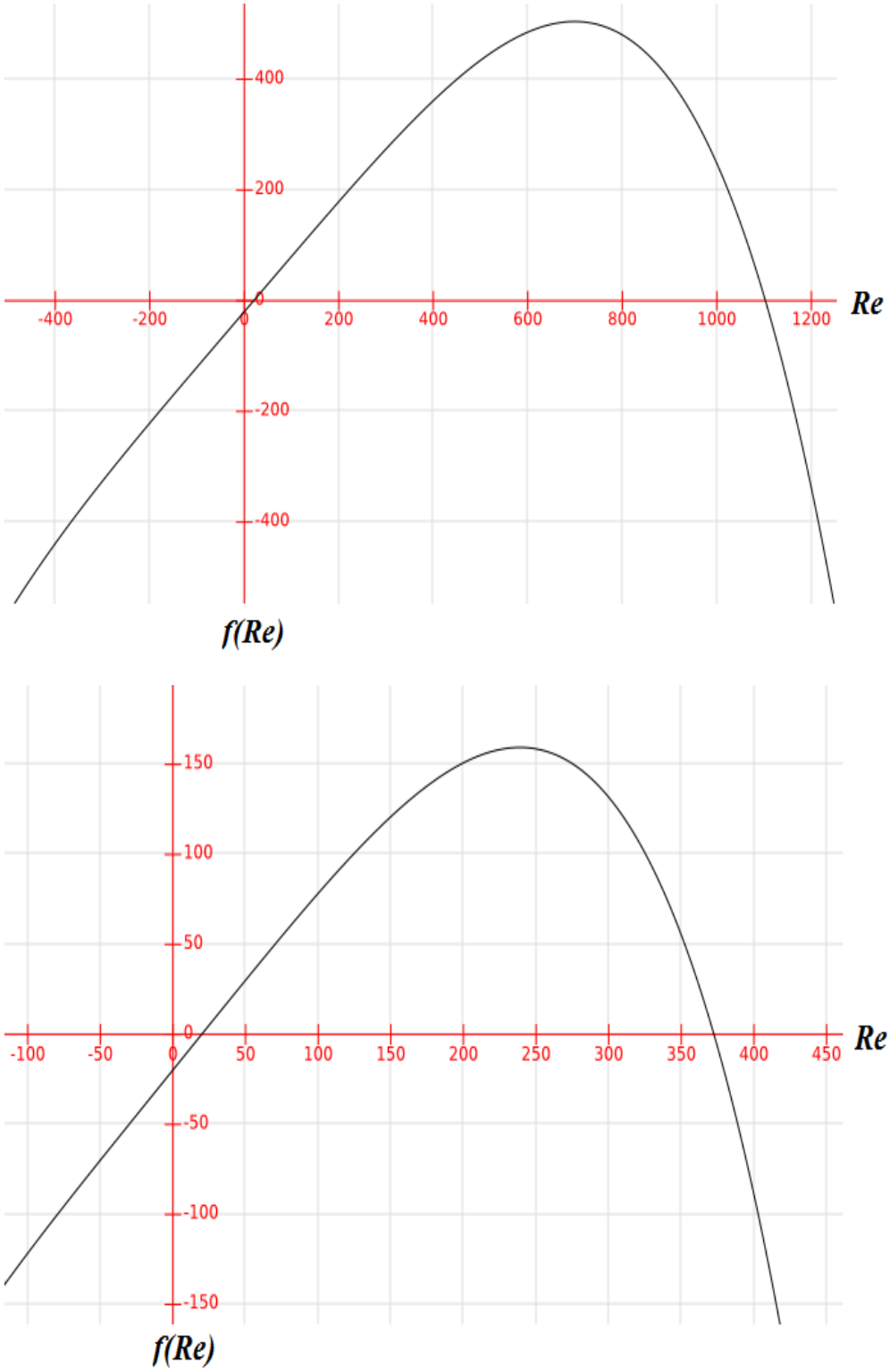

Fig. 17: Plot of the left-hand side of the inequality in Eq. (5.42), expressed as $f(Re)$, for Argon with $M = 39.948 \times 10^{-3}\ kg$ (*top*) and $M = 1$ (*bottom*).

An exciting result of Eq. (5.42) is that, by choosing $M = 1$, and solving the quartic equation (see Fig. 17), we obtain a baseline value for the critical Reynolds number as Re_{cr}~372.45 which is remarkably consistent with experimental observations. This significantly tightens the lower bound of $Re_{cr} \geq 2\pi^2$ derived from the classical Poincaré inequality, as shown in Fig. 23. In fact, the application of the FT has yielded a result consistent with experimental observations. Additionally, the explicit use of the molar mass, M, of the fluid under consideration yields a modified value for Re_{cr} that satisfies the inequality in Eq. (5.42) to serve as an upper bound. For instance, the critical Reynolds number for Argon from Table 2 would be in the region $372.45 \leq Re_{cr} \leq 1{,}103$, as shown in Fig. 23. Somewhere in this region is where the transition to turbulence is expected to occur spontaneously.

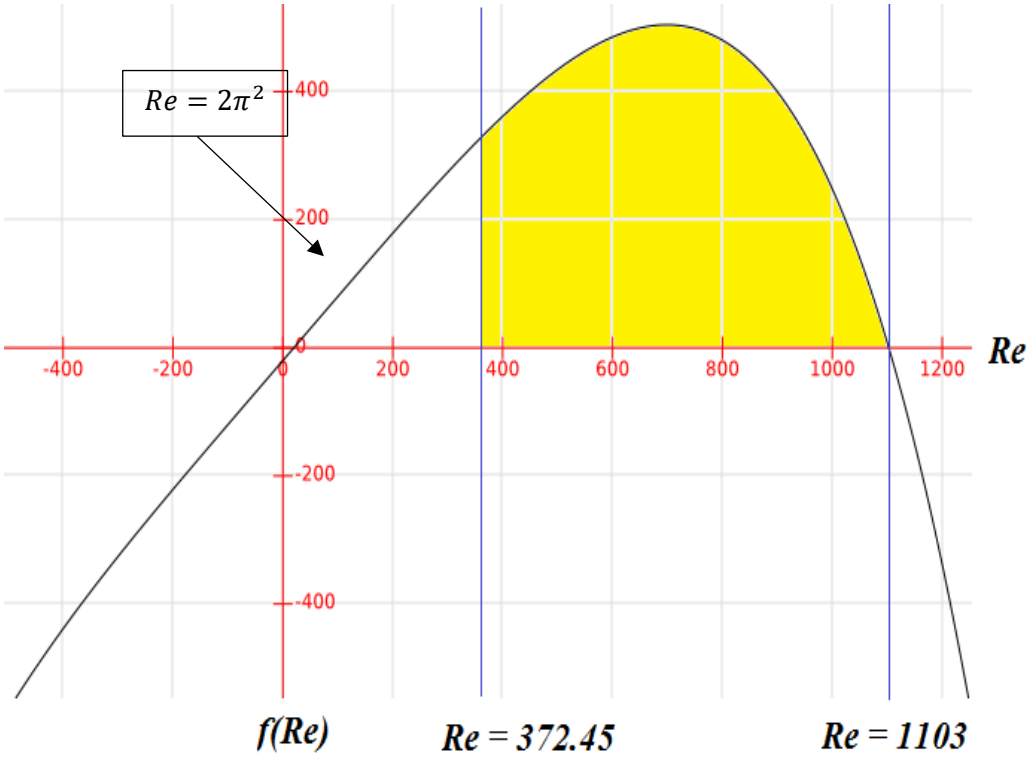

Fig. 18: Plot of inequality in Eq. (5.42) for Argon showing the critical Reynolds number. The yellow shaded region is constrained by the two values for the critical Reynolds number that satisfy Eq. (5.42). The classical deterministic solution of $Re \geq 2\pi^2$ is shown to illustrate the tightening of the bounds via implementation of the FT.

Table 2: Critical Reynolds numbers for gases based on Eq. (5.42)

Gas	**M** (g/mol)	$\mathbf{Re_{cr}}$
$\mathbf{N_2}$	28.014	1255
Ar	39.948	1103
$\mathbf{Cl_2}$	70.9	923
$\mathbf{n-Decane}$	142.86	733
$\mathbf{H_2O}$	18.015	1453
$\mathbf{H_2}$	2.008	3013
He	4.0026	2395
PEG 400	420	513

From Table 2, we gather that the predicted upper bound for the critical Reynolds number from Eq. (5.42) is larger for lighter gases than heavier ones as dictated by their molar mass. Only for the heaviest organic compounds (n-Decane and PEG 400) do we observe Re_{cr} being close to the experimental value of 360 reported in the literature. One possible reason for this fluid-dependent Reynolds number could be that, for light gases, the random molecular motion is inherently significant as compared to their heavier counterparts. Therefore, perturbations of much higher magnitude are required to overcome this natural activity and create sufficient inertial disturbance to induce turbulence. As an example, the flow of the diatomic hydrogen gas potentially becomes turbulent at $Re_{cr}\sim 2{,}395$, whereas the flow of the diatomic chlorine gas, which is roughly 35 times heavier, is predicted to become turbulent at $Re_{cr}\sim 923$, and PEG 400 (polyethylene glycol 400) which is more than 200 times heavier is predicted to become turbulent at $Re_{cr}\sim 513$. It is interesting to note that although the upper bound value for the critical Reynolds number for the majority of the gases is much greater than the experimental value of 360 or the computational value of 372.45, they are still on the order of 1,000 as described in Ref. [23]. One possible explanation for this over-prediction could be due to the 2D nature of the analysis leading to Eq. (5.42) which constrains perturbations to the $xy-$plane, inhibiting the development of 3D disturbances and vortex formation. A much tighter bound on the critical Reynolds number could potentially be obtained with a 3D analysis that would relax these constraints.

5.3.2 Kinetic Energy of Velocity Perturbations

To calculate the kinetic energy of velocity perturbations we divide the simulation domain in the *y*-direction into 20 equally thick slabs and calculate the spatially averaged velocities of the particles in that region. The spatially averaged velocities are obtained by binning each of the 20 slabs and then estimating the average velocity by

$$\langle v'(y,t)\rangle = \frac{1}{n}\sum_{i=1}^{n}\left(\frac{1}{N}\sum_{j=1}^{N} v_j\left(q_{x,j}, q_{y,j}, t\right)\right) \tag{5.43}$$

where n is the number of bins in each slab, N is the number of particles in a bin, and $\mathbf{q}$ is the coordinate in one of these sub-cells. At each instant of time, the fluctuations are calculated by subtracting the streaming velocity profile, $\mathbf{u}(\mathbf{r},t) = \mathbf{i}\dot{\gamma}y$. We then calculate the kinetic energy of the perturbations at each of the slabs as $K(y,t) = \frac{1}{2}\rho_0\|\boldsymbol{v}'(y,t)\|^2$. By averaging over all the spatial slabs, we obtain the global perturbation field as $K(t) = \frac{1}{20}\sum_{i=1}^{20} K(y_i,t)$.

5.3.3 Instability and Transition.

Table 3: Reynolds numbers for LJ fluid at the state point $(\rho^*, T^*) = (0.8442, 0.722)$ based on channel widths

$L_y^*\sigma$	$\dot{\gamma}^* = \mathbf{0.1}$	$\dot{\gamma}^* = \mathbf{0.5}$	$\dot{\gamma}^* = \mathbf{1.5}$	$\dot{\gamma}^* = \mathbf{2.5}$
10	2.3	11.35	34	56.7
25	14	71	212.75	354.6
50	56.7	284	851	1418.3

We restrict ourselves to an LJ fluid at the state point $(\rho^*, T^*) = (0.8442, 0.722)$. Fig. 19 shows the time-evolution of the kinetic energy of the perturbation field for different system sizes characterized by the number of particles N. For $N = 200$, 500, and 1,000, the channel width is $L = 10\sigma$, 25σ, and 50σ, respectively. We have normalized the velocities by $\|\mathbf{v}'\|_0^2$ which is $\|\mathbf{v}'(\mathbf{x}, \mathrm{t} = 0)\|$. Hence, at $t = 0$ the normalized variable being plotted $|\mathbf{v}|^2 = \frac{\|\mathbf{v}'\|^2}{\|\mathbf{v}'\|_0^2} = 1$. The most immediate observation is that, as suggested by Eq. (5.29), the kinetic energy of the perturbation

field undergoes a general exponential decay superposed with an additional stochastic contribution. The randomness is due to the fluctuations in the shear stress and results in a non-monotonic decay of perturbations. Therefore, over the general exponentially decaying trend, we would observe instances of a spontaneous increase in kinetic energy.

It is expected that in situations where the stochastic forcing of the shear stress is sufficiently strong, it can result in transient amplification of the kinetic energy that overcomes the exponential stability, thus resulting in a subcritical transition to turbulence. This is illustrated in Fig. 19a, for $\dot{\gamma}^* = 0.1$. The Reynolds number for $L_y = 10\sigma$ is approximately $Re = \rho_0 \dot{\gamma} L_y^2 / \eta \approx 2.3$. This is well below the threshold ($325 \leq Re_{cr} \leq 370$) at which we would expect the breakdown of hydrodynamic stability as suggested by experiments for plane Couette flow [34], [70]. However, we see transient amplification of the kinetic energy.

The instances of subcritical transition can be seen in cases with $L_y^* = 25\sigma$ and $\dot{\gamma}^* = 2.5$ (Fig. 3d), and $L_y^* = 50\sigma$ and $\dot{\gamma}^* = 0.5$ (Fig. 19b). In Fig. 19b, we see that for $N = 200$ and $N = 500$ the perturbation field decays exponentially.

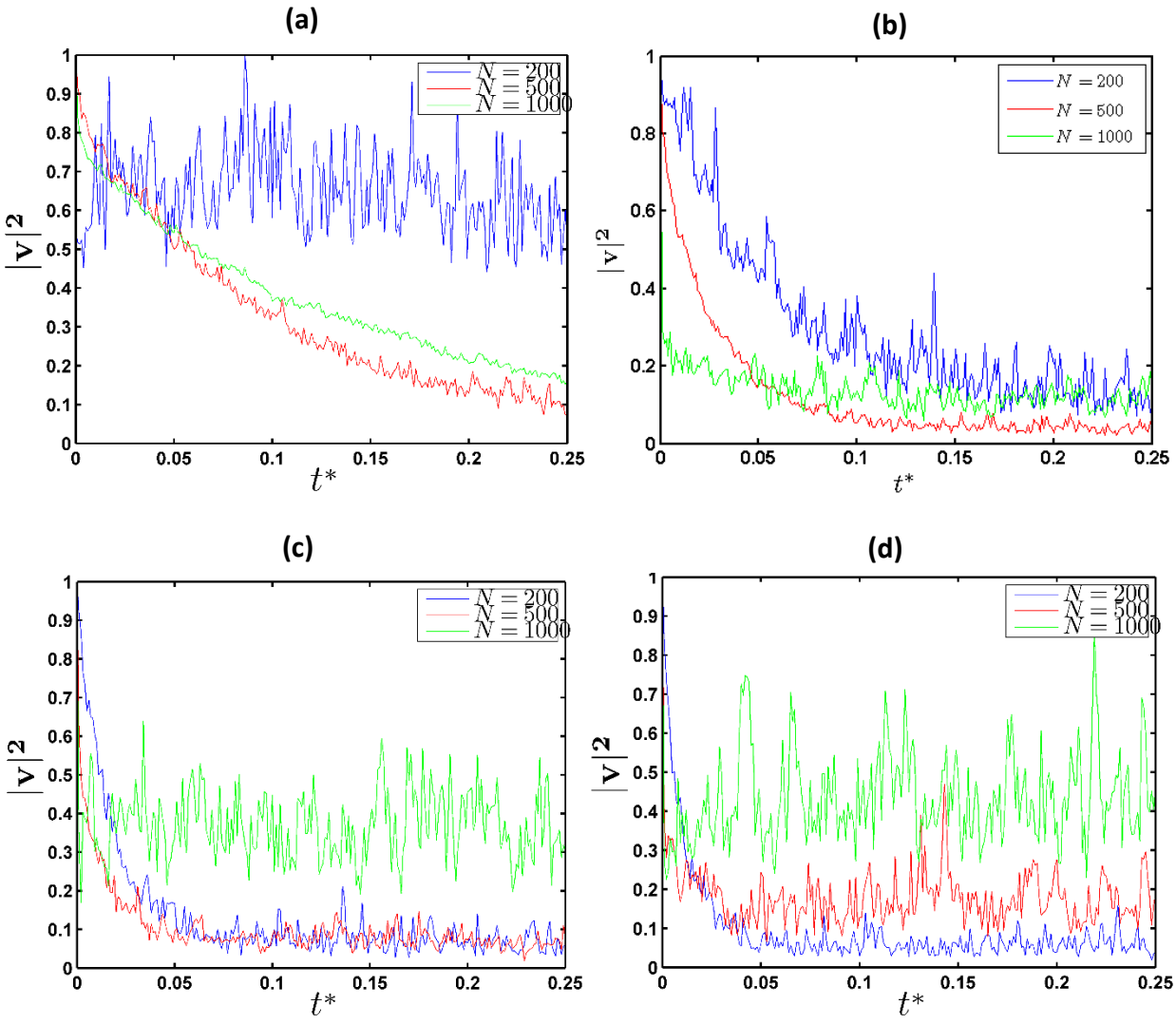

Fig. 19: The kinetic energy of the time-varying velocity perturbations for LJ fluid at the state point $(\rho^*, T^*) = (0.8442, 0.722)$ for (a) $\dot{\gamma}^* = 0.1$ and (b) $\dot{\gamma}^* = 0.5$ and (c) $\dot{\gamma}^* = 1.5$ and (d) $\dot{\gamma}^* = 2.5$.

However, for $N = 1000$, $|\mathbf{v}|^2$ does not decay but rather fluctuates around a constant value. This is because the Reynolds number $Re = 284$, which very close to the transition regime for Couette flow ($Re \sim 320$ at the lower end). Near this region, we no longer observe a transient decay of perturbations as the flow is no longer stable. In Fig. 19c and Fig. 19d we see that for the larger systems, $|\mathbf{v}|^2$ increases. The fluid is no longer stable and thus a transition is taking place which is illustrated by the lack of exponential decay of the perturbation field. Table 3 provides further evidence from the Reynolds numbers, which are greater than 320. This indicates

that the fluid flow is in the regime where transient growth of perturbations is generally observed.

The Reynolds numbers for the range of strain-rates considered and several channel widths are shown in Table 3. One possible reason for this transient growth in kinetic energy at subcritical Reynolds numbers is that stochastic forcing facilitates the transfer of energy from the mean flow to the perturbation field, which may potentially be greater than the sum of all the contributions of the normal modes being independently excited by a stochastic forcing field [28]. Thus, despite exponential stability, in some cases, we observe transient growth.

In summary, the observations drawn from Fig. 19 are precisely those characterizing instability based on the Reynolds-Orr equation [69]. Therefore, it is not necessarily true that the magnitude of perturbations becomes smaller as the system size increases. This is only the case if the inequality in Eq. (5.29) is satisfied. Otherwise, as we approach the critical Reynolds number the perturbations will cease to decay. In particular, observations from Fig. 19c and Fig. 19d indicate that as the system size increases, the Reynolds number increases leading to growth (rather than decay) of the perturbation field.

5.3.4 Shear Thinning and 'String' – Phase Instability

Fig. 20 illustrates the stress strain-rate response and the density profiles before and after the onset of shear-thinning. From Fig. 20a, it is observed that all the fluids that undergo shear-thinning are characterized by a dramatic change in the slope of the response plot. The peaks of the response curves are the reduced critical strain-rates, $\dot{\gamma}_{cr}^{*}$ at which that change occurs. For the Lennard-Jones (LJ) fluid at a reduced density $\rho^{*} = 0.8442$ and a reduced temperature of $T^{*} = 0.722$, which corresponds to the triple-point of Argon, $\dot{\gamma}_{cr}^{*} \approx 1.0$. The cause of shear-thinning is the molecular alignment in the direction of the flow leading to the saw-toothed profile after the onset of shear-thinning (Fig. 20c) as opposed to a homogeneous density profile (Fig. 20b), which are shown for the LJ fluid at $(\rho^{*}, T^{*}) = (0.8442, 0.722)$. Fig. 20c gives the characteristic profile of the so-called 'string'-phase [5], [7]. In this

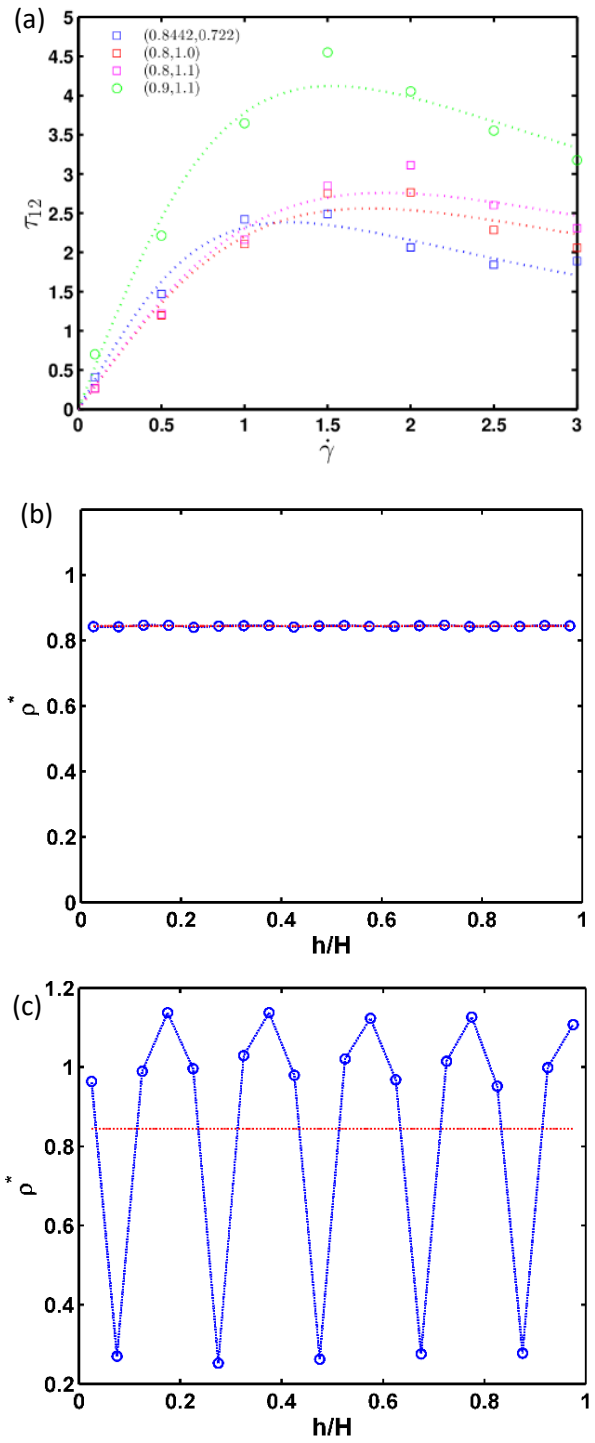

Fig. 20: Response and structural features of shear-thinning and the 'string'-phase. (a) Stress strain-rate responses for different Lennard-Jones state-points [35], (b) homogeneous density profile for $\dot{\gamma}^* = 0.5$, and (c) saw-tooth density profile in the 'string'-phase after the onset of shear-thinning for $\dot{\gamma}^* = 2.5$. (b) and (c) correspond to the fluid at a state with a reduced density $\rho^* = 0.8442$ and a reduced temperature of $T^* = 0.722$ [43].

phase, particles organize themselves into columns in the direction of flow with hexagonal symmetry [34], [70].

5.3.5 The Nature of Perturbations

In the event of transient growth of the kinetic energy, what we observe is that, rather than the development of vortices, the particles align themselves in the direction of the flow resulting in shear-thinning. This phenomenon is illustrated in Fig. 21, where we have plotted the density correlations $\langle \delta(t)\delta(t+s) \rangle$. As the strain-rate increases, the density correlations decay more slowly. In fact, what we observe is that the stochastic fluctuations of the shear stress augment the density fluctuations leading to the formation of the 'string'-phase. By observing shear stress autocorrelations, $R(t)$, in Fig. 22 and, in particular, Fig. 22c and Fig. 22d, we notice that the 'string'-phase is accompanied by prevalent fluctuations in the shear stress, in contrast to the amorphous phase (Fig. 22a and Fig. 22b). Consistent with well-established observations, shear stress fluctuations (related to velocity perturbations) are slow in 2D. The 'string'-phase instability is a manifestation in 2D Couette flow as an artifact of the thermostatting mechanism in the SLLOD equations [6], [10] due to the confinement of velocity perturbations in the xy-plane. In fact, in 3D Couette flow the presence of rapid fluctuations in velocity perturbations along with the presence of fluctuations in the y and z directions perpendicular to the direction of the flow, leads to the formation of streamwise vortices that result in the disappearance of the 'string'-phase [34]. These observations allude to the fact that 3D disturbances along with rapid fluctuations in the shear stress, and the formation of vortices, are necessary for the emergence of turbulence at subcritical Reynolds numbers and the prevention of an ordering transition from the amorphous to the 'string'-phase.

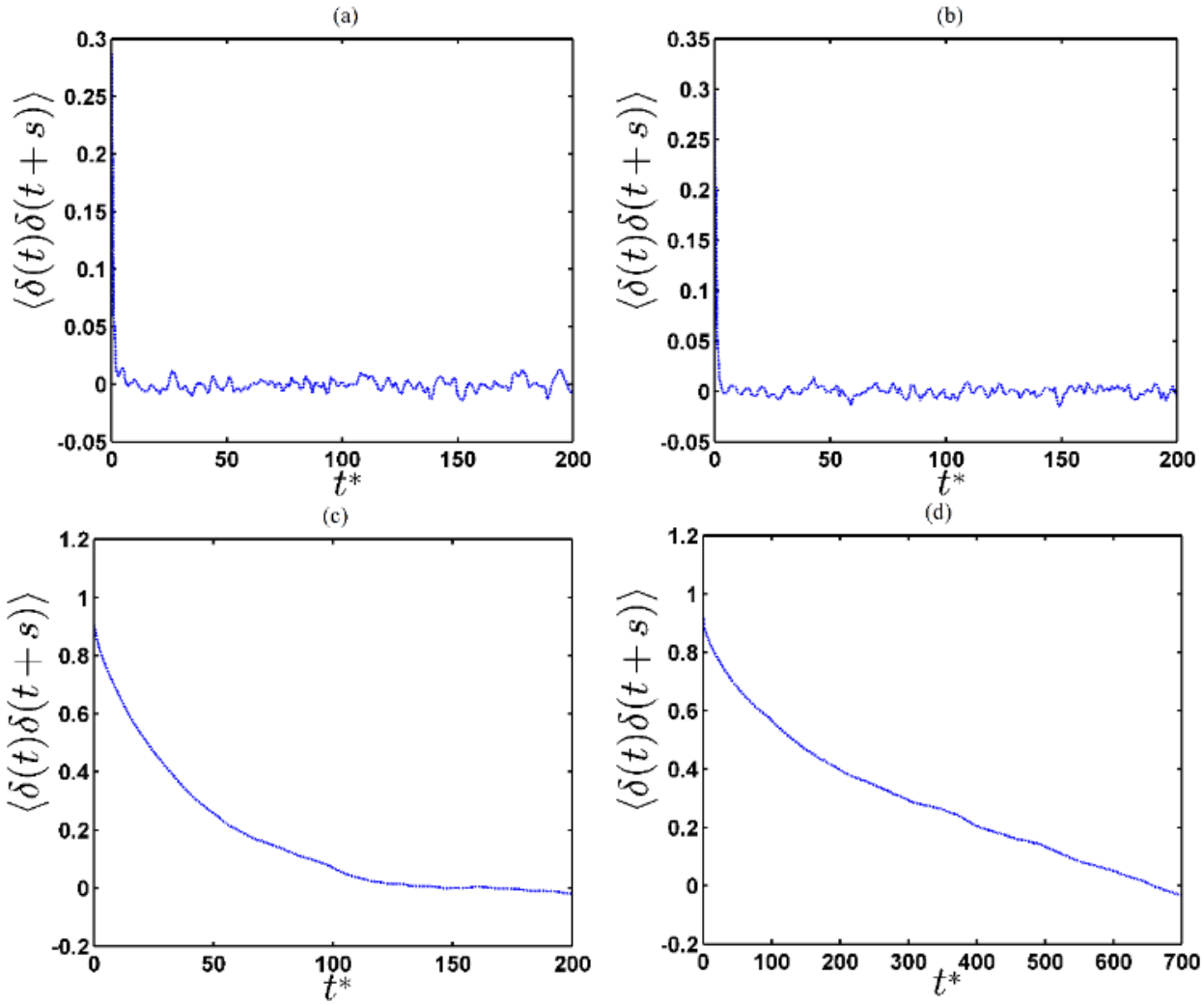

Fig. 21: Density correlations and for LJ fluid at the state point $(\rho^*, T^*) = (0.8442, 0.722)$ for (a) $\dot{\gamma}^* = 0.1$ and (b) $\dot{\gamma}^* = 0.5$ and (c) $\dot{\gamma}^* = 1.5$ and (d) $\dot{\gamma}^* = 2.5$.

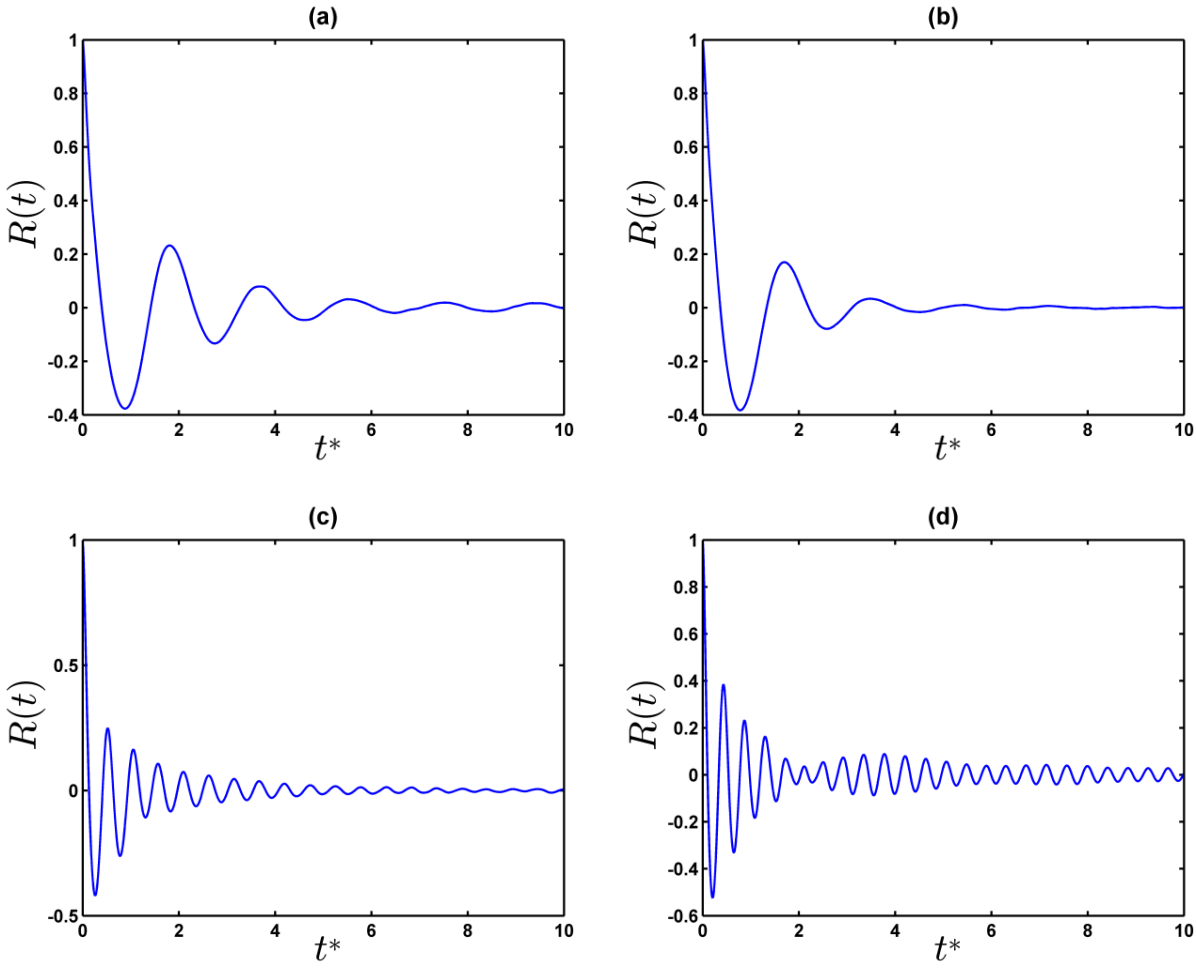

Fig. 22: Shear stress autocorrelation for LJ fluid at the state point $(\rho^*, T^*) = (0.8442, 0.722)$ for (a) $\dot{\gamma}^* = 0.1$ and (b) $\dot{\gamma}^* = 0.5$ and (c) $\dot{\gamma}^* = 1.5$ and (d) $\dot{\gamma}^* = 2.5$.

5.4 Conclusions

In this chapter, we study the dissipation of kinetic energy of perturbations in a molecular fluid undergoing Couette flow, with the particles interacting via the Lennard-Jones potential. By employing the Lees-Edwards periodic boundary conditions and the Poincaré inequality, we obtain a stochastic Langevin-equation-type generalization to the classical exponential decay of the perturbation field, as shown in Eq. (5.22)**.** We illustrate the intimate connection between the relation Eq. (5.22) and the FT by showing that the random term in Eq. (5.22) is simply the dissipation function that is the cornerstone of the FT.

We demonstrate how under the assumption of Maxwell dynamics the variance can be used to establish a lower bound on the critical Reynolds number at which the transition to turbulence occurs. This value of Re depends on the molar mass of the fluid and is obtained by solving a 4^{th}-order polynomial equation. We highlight reasons as to the nature of this fluid dependence and the departure from experimental observations at continuum scales.

Furthermore, we provide computational evidence of this phenomenon by running NEMD simulations using SLLOD dynamics in LAMMPS. It is observed that the decay of the perturbation field is dependent on the strain-rate and the system volume (or the number of particles in the fluid). In general, in the laminar regime of the flow, we see an exponential albeit non-monotonic decay owing to fluctuations in the shear stress. Additionally, there are instances of large increases in the perturbation field owing to negative instances of shear stress as predicted by the FT. We formulate the dissipation function and the rate of entropy production and demonstrate the system's tendency to violate the second law of thermodynamics, which strongly influences the stability of the system, as particularly evident in small systems. As the system size increases, we see that the decay is faster and the magnitude of fluctuations is smaller. For larger system sizes, we also see that the perturbations do not decay. This is expected to be due to the onset of turbulence and the formation of vortices in the stream-wise direction.

Chapter 6

Conclusion and Future Research

Concluding remarks on the topics presented in the dissertation are provided in this chapter, followed by a discussion on some future research directions. It was highlighted that in sub-continuum flows, fluids exhibit exotic properties not observed at continuum scales. In this dissertation, the focus was on the viscosity of the fluid and its tendency to spontaneously violate the second law of thermodynamics.

In Chapter 3, we focused on the shear thinning characteristics of a fluid composed of Lennard-Jones particles. Based on NEMD observations, we reported that at a critical strain rate, the fluid undergoes dramatic shear thinning. Although the fluid is inherently homogeneous and isotropic, at the critical strain rate it begins to align in the direction of the flow and form ‘strings’. The layering of the fluid results in a drop in friction between fluid layers causing a dramatic change in the slope of the stress-deformation response and a corresponding drop in viscosity. In light of these observations, we used the BGK approximation to the Boltzmann equation to obtain a strain rate dependent constitutive model for the shear stress. From this model, we obtained a model for the viscosity which resembles the Cross model but absent empirical fitting constants. We also established the existence of scaling behavior in the LJ fluid by unifying the rheological behavior of the LJ fluid at several state points through the effective molecular collision frequency, which forms the basis of the BGK approximation. We expressed this parameter entirely in terms of measurable fluid properties, i.e. its density, temperature and Newtonian viscosity. Finally, within the framework of thermomechanics, such fluids must be treated as quasi-linear to accurate capture their non-Newtonian behavior.

Chapter 4 delved into the stochastic nature of the sub-continuum flows and the implications of instantaneous violations of the second law of thermodynamics. We developed a theoretical framework to generalized continuum theories to microscale flows via the fluctuation theorem (FT) and demonstrated the importance

of the shear stress in bridging the gap between these two distinct scales. In particular, we showed how random fluctuations in the shear stress play a critical role in the microscale dynamics of the flow. Via density perturbations of the Navier-Stokes equations, we illustrated the interplay between these important factors and their decoupling at the continuum limit. Subsequently, we studied and characterized the randomness in the shear stress and local density fluctuations, and the nature of these fluctuations. This was achieved by analyzing their temporal and spectral characteristics. We developed a range of models for atomic fluids that could potentially enhance the current state of simulations in micro and nano-fluidics by enriching conventionally deterministic models by introducing crucial statistical effects.

Building upon the observations and conclusions of Chapter 4, in Chapter 5 we investigated how stochastic fluctuations in the shear stress affected the flow stability of the fluid. Using the Poincare inequality and the Navier-Stokes equations, we generalized the conventional exponential stability of the kinetic energy of velocity perturbations to a stochastic Langevin equation that incorporates the fluid's tendency to spontaneously violate the second law of thermodynamics. We discussed the intricate connection of this equation to the FT via the dissipation function. The latter forms the basis of the FT and explicitly arises in the governing equation for velocity perturbations. Owing to the analytical nature of this equation, we solved this model for the variance of velocity perturbations and obtained a fluid-dependent lower bound on critical Reynolds number for the onset of turbulence, thus shedding some light on the nature of subcritical transitions in Couette flow. We substantiated our theoretical analyses with computational evidence with cases of exponential decay and transient amplification of the kinetic energy of velocity perturbations. We discussed reasons for their occurrence and the nature of these perturbations as applicable to Couette flow of atomic fluids.

6.1 Major Outcomes

In summary, the major outcomes of this research are as follows:

1. Atomic fluids undergo a strain-rate dependent ordering transition from an amorphous to a ‘string’-phase that leads to shear thinning.
2. The shear stress and viscosity are accurately captured by a model similar to the Cross viscosity model.
3. The effective molecular collision frequency from the BGK approximation to the Boltzmann equation acts as a universal scaling constant that unifies the rheological behavior of the LJ fluid at several state points.
4. Shear stress fluctuations and density perturbations play a crucial role in dynamics of microscale flows.
5. The FT is a key tool that allows us to generalize continuum laws to sub-continuum scales via the dissipation function.
6. Owing to FT, the stability of microscale flows, as characterized by the kinetic energy of velocity perturbations, is governed by a stochastic Langevin equation which reduces to classical exponential stability at continuum scales.
7. The introduction of stochastic fluctuations in the shear stress enriches the classical exponential model by facilitating the establishment of a tighter lower bound on the critical Reynolds number for the onset of turbulence.
8. The critical Reynolds number in (7) is fluid-dependent and much closer to experimental observations.
9. The theoretical and computational evidence [in (6) - (8)] provide insight into the nature of subcritical transitions to turbulence as commonly observed in simulations and experiments of Couette flow.

6.2 Future Directions

6.2.1 Flow in Porous Media

Scale-dependent homogenization of flow in spatially-random porous media under Dirichlet and Neumann boundary conditions was considered in [71]. In this study, estimates on the size of the Representative Volume Element (RVE) of a conventional continuum Darcy’s Law

$$q_i = \frac{1}{\eta} \mathrm{K} p_i \tag{6.1}$$

were obtained; here q_i is the fluid flux and K is the permeability. This approach may be generalized to account for the existence of nano-channels in which spontaneous violations of the second law may occur, Fig. 23. In this case, a modification of Darcy's law to the form

$$q_i = \frac{1}{\eta} (\mathrm{K} + \mathcal{M}) p_i \tag{6.2}$$

is expected; here $\mathcal{M}$ is the randomness in permeability. MD can provide insight into fluctuations in the narrow channels and potentially allow one to probe the appropriate type of randomness consistent with the FT. This would further our understanding of fluid flow in large networks of micro/nano-channels (e.g. capillaries in biological systems, nano-foams, etc).

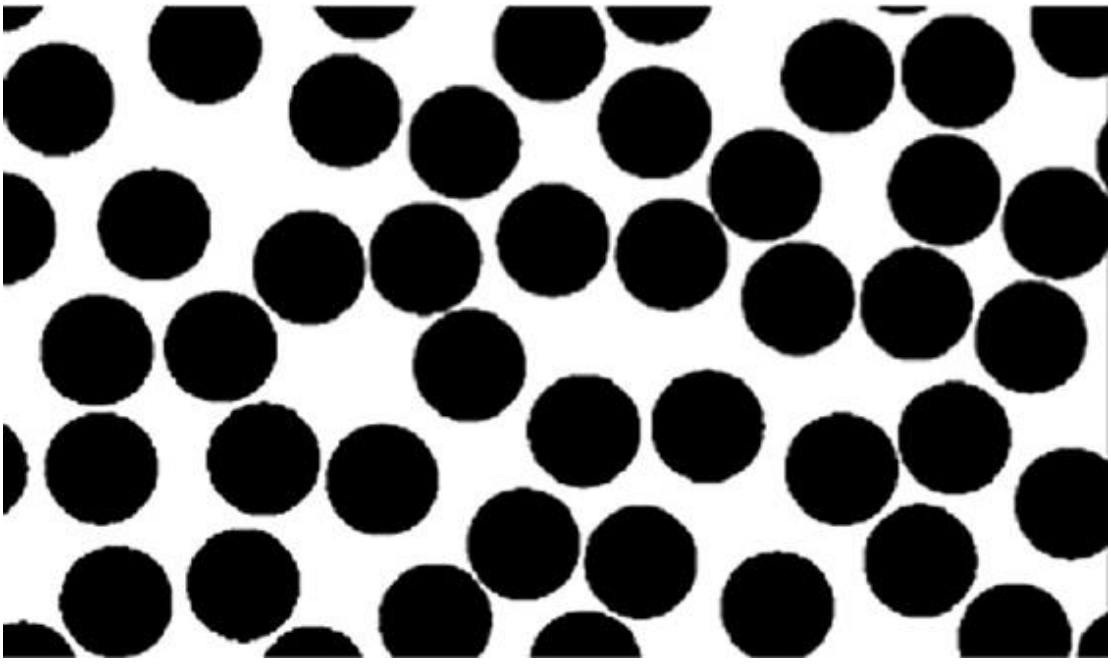

Fig. 23: Sample porous medium with narrow channels that can potentially result in the fluid spontaneously violating the second law of thermodynamics.

6.2.2 Micropolar Fluids

Micropolar fluids are fluids with microscale orientational order, i.e. individual material points can undergo rigid rotations in addition to translation, the rotations being independent degrees of freedom not dictated by the gradient of velocity field [72]. Additionally, such fluids carry couples and do not require the Cauchy stress tensor to be symmetric. They are interesting because they possess the basic mechanisms relevant to suspensions, liquid crystals, and anisotropic fluids. In these physical systems, molecular rotation influences the hydrodynamics of the fluid and NEMD is particularly well suited to study these effects [1].

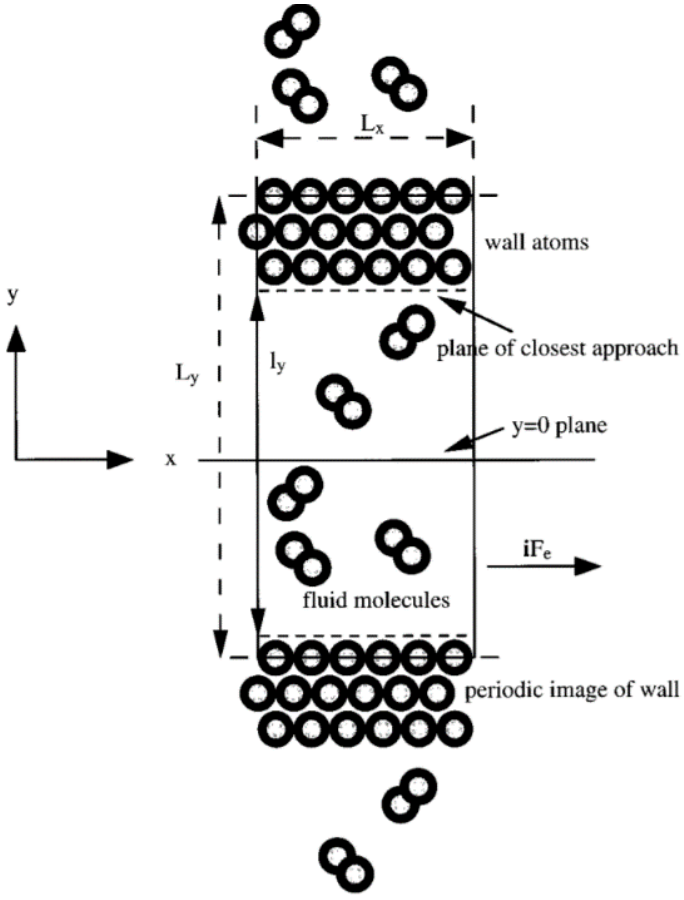

Fig. 24: Schematic of a Couette/Poiseuille flow system with explicit walls. The fluid, in this case, is comprised of large diatomic molecules (similar to chlorine gas) that possess translation as well as rigid rotation.

Our aim is to focus on Couette and Poiseuille flows, for which the solutions are analytic and therefore amenable to testing by computer simulation experiments [73]. In contrast to an idealized NEMD study using Lees-Edwards Periodic Boundary Conditions, we will investigate explicit wall-driven flows as shown in Fig. 24.

NEMD is particularly suited for this study as large molecules (such as polymer chains, ellipsoidal suspensions, etc) are naturally allowed to rotate in addition to translation. This offers a more realistic scenario as molecules such as water and chlorine inherently possess structure (see Fig. 25).

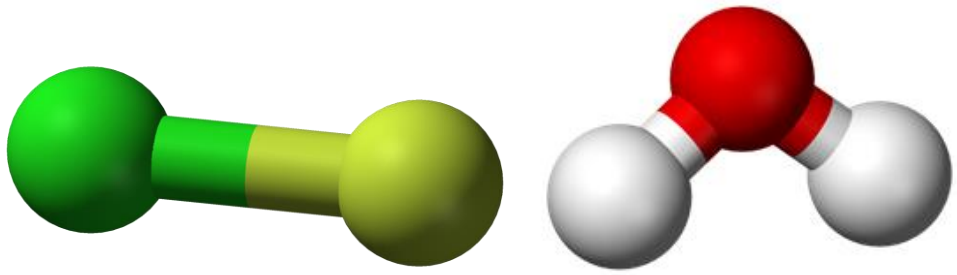

Fig. 25: Chlorine *(left)* and water *(right)* molecular models. Simulations incorporating these structures and treating them as rigid bodies have the potential to offer more realistic insights into fluid behavior in micro and nano-fluidic engineering applications.

It has been demonstrated that the micropolar fluid model agrees well with NEMD results for Poiseuille flow. The objectives and foci of a future study would be as follows:

1. To investigate the influence of molecular rotation on fluid hydrodynamics and examining the consistency of micropolar theory in modeling fluids comprised of large molecules and comparing the computational with analytical results available in the literature to verify our models.
2. Flow stability/instability of large molecules via the stress-deformation response, where it is expected that the rotation of the molecules would impact the flow stability and the critical Reynolds number at which the transition to an unstable flow occurs. Additionally, the research should clarify whether the ‘string-phase’ instability occurs in wall-driven flows.

3. Effects of walls (for example, slip-length) on the structure and flow dynamics of the fluid, and the extent of these effects depending on the channel size. In poromechanics, one would expect the structure of the walls of channels to affect the hydrodynamics of the flow, especially for very small channels. As the channel size increases, these effects should decrease. The goal would be to fully grasp the nature of these effects and their dependence on channel width.
4. Rheological properties/anisotropic fluid behavior with the aim to develop a model for stress and couple-stress viscosities that account for the geometry of molecules in addition to strain-rate dependence.
5. Extend (4) to fluid mixtures (i.e. colloidal suspensions) so that volume fractions are also considered.

References

[1] J. Delhommelle and D. J. Evans, "Poiseuille flow of a micropolar fluid," *Molecular Physics,* vol. 100, no. 17, pp. 2857-2865, 2002.

[2] D. M. Heyes, "Shear thinning of the Lennard-Jones fluid by molecular dynamics," *Physica A: Statistical Mechanics and its Applications,* vol. 133, no. 3, pp. 473-496, 1985.

[3] D. M. Heyes, "Structural changes in simple liquids during extreme shearing," *Chemical Physics Letters,* vol. 127, no. 5, pp. 515-520, 1986.

[4] D. M. Heyes, "The nature of extreme shear thinning in simple liquids," *Molecular Physics,* vol. 57, no. 6, pp. 1265-1282, 1986.

[5] D. M. Heyes, "Non-Newtonian behaviour of simple liquids," *Journal of Non-Newtonian Fluid Mechanics,* vol. 21, no. 2, pp. 137-155, 1986.

[6] J. Delhommelle, J. Petravic and D. J. Evans, "Reexamination of string phase and shear thickening in simple fluids," *Physical Review E,* vol. 68, no. 3, p. 031201, 2003.

[7] J. Delhommelle, J. Petravic and D. J. Evans, "Non-Newtonian behavior in simple fluids," *The Journal of Chemical Physics,* vol. 120, no. 13, pp. 6117-6123, 2004.

[8] D. J. Evans, "Molecular dynamics simulations of the rheological properties of simple fluids," *Physica A: Statistical Mechanics and its Applications,* vol. 118, no. 1-3, pp. 51-68, 1983.

[9] A. Baranyai and P. T. Cummings, "Fluctuations close to equilibrium," *Physical Review E,* vol. 52, no. 3, p. 2198, 1995.

[10] D. J. Evans and G. Morriss, *Statistical Mechanics of Nonequilibrium Liquids*, Cambridge University Press, 2008.

[11] S. Bair, C. McCabe and P. T. Cummings, "Comparison of nonequilibrium molecular dynamics with experimental measurements in the nonlinear shear-thinning regime," *Physical Review Letters,* vol. 88, no. 5, p. 058302, 2002.

[12] S. T. Cui, S. A. Gupta, P. T. Cummings and H. D. Cochran, "Molecular dynamics simulations of the rheology of normal decane, hexadecane, and tetracosane," *The Journal of Chemical Physics*, vol. 105, no. 3, pp. 1214-1220, 1996.

[13] S. T. Cui, P. T. Cummings, H. D. Cochran, J. D. Moore and S. A. Gupta, "Nonequilibrium molecular dynamics simulation of the rheology of linear and branched alkanes," *International Journal of Thermophysics*, vol. 19, no. 2, pp. 449-459, 1998.

[14] A. Berker, S. Chynoweth, U. C. Klomp and Y. Michopoulos, "Non-equilibrium molecular dynamics (NEMD) simulations and the rheological properties of liquid n-hexadecane," *Journal of the Chemical Society, Faraday Transactions*, vol. 88, no. 13, pp. 1719-1725, 1992.

[15] H.-C. Tseng, J.-S. Wu and R.-Y. Chang, "Shear thinning and shear dilatancy of liquid n-hexadecane via equilibrium and nonequilibrium molecular dynamics simulations: Temperature, pressure, and density effects," *The Journal of Chemical Physics,* vol. 129, no. 1, p. 014502, 2008.

[16] Y.-R. Jeng, C.-C. Chen and S.-H. Shyu, "A molecular dynamics study of lubrication rheology of polymer fluids," *Tribology Letters,* vol. 15, no. 3, pp. 293-299, 2003.

[17] X. Xu, S. A. Rice and A. R. Dinner, "Relation between ordering and shear thinning in colloidal suspensions," *Proceedings of the National Academy of Sciences,* vol. 110, no. 10, pp. 3771-3776, 2013.

[18] H. Farhat and B. C. Eu, "Monte Carlo method and the nonequilibrium structure and non-Newtonian viscosity of a sheared simple liquid," *The Journal of Chemical Physics,* vol. 110, no. 1, pp. 97-108, 1999.

[19] R. Laghaei, A. Eskandari Nasrabad and B. C. Eu, "Statistical-mechanical theory of rheology: Lennard-Jones fluids," *The Journal of Chemical Physics,* vol. 123, no. 23, p. 234507, 2005.

[20] K. Y. Volokh, "An investigation into the stability of a shear thinning fluid," *International Journal of Engineering Science,* vol. 47, no. 5-6, pp. 740-743, 2009.

[21] K. Y. Volokh, "Navier-Stokes model with viscous strength," *Comp. Model. Eng. Sci,* vol. 92, pp. 87-101, 2013.

[22] S. A. Orzag, "Numerical simulation of incompressible flows within simple boundaries, I. Garlekin (spectral) representation," *Stud. Appl. Math,* vol. 50, pp. 293-327, 1971.

[23] S. A. Orszag and L. C. Kells, "Transition to turbulence in plane Poiseuille and plane Couette flow," *Journal of Fluid Mechanics,* vol. 96, no. 1, pp. 159-205, 1980.

[24] V. A. Romanov, "Stability of plane-parallel Couette flow," *Functional Analysis and its Applications,* vol. 7, no. 2, pp. 137-146, 1973.

[25] A. Lundbladh and A. V. Johansson, "Direct simulation of turbulent spots in plane Couette flow," *Journal of Fluid Mechanics,* vol. 229, pp. 499-516, 1991.

[26] N. Tillmark and P. H. Alfredsson, "Experiments on transition in plane Couette flow," *Journal of Fluid Mechanics,* vol. 235, pp. 89-102, 1992.

[27] S. Grossmann, "The onset of shear flow turbulence," *Reviews of Modern Physics,* vol. 72, no. 2, p. 603, 2000.

[28] B. F. Farrell and P. J. Ioannou, "Stochastic forcing of the linearized Navier–Stokes equations," *Physics of Fluids A: Fluid Dynamics,* vol. 5, no. 11, pp. 2600-2609, 1993.

[29] S. C. Reddy and D. S. Henningson, "Energy growth in viscous channel flows," *Journal of Fluid Mechanics,* vol. 252, pp. 209-238, 1993.

[30] K. M. Butler and B. F. Farrell, "Three-dimensional optimal perturbations in viscous shear flow," *Physics of Fluids A: Fluid Dynamics,* vol. 4, no. 8, pp. 1637-1650, 1992.

[31] H. B. Squire, "On the stability for three-dimensional disturbances of viscous fluid flow between parallel walls," *Proceedings of the Royal Society of London. Series A, Containing Papers of a Mathematical and Physical Character,* vol. 142, no. 847, pp. 621-628, 1933.

[32] A. W. Lees and S. F. Edwards, "The computer study of transport processes under extreme conditions," *Journal of Physics C: Solid State Physics,* vol. 5, no. 15, p. 1921, 1972.

[33] W. Loose and S. Hess, "Rheology of dense model fluids via nonequilibrium molecular dynamics: Shear thinning and ordering transition," *Rheologica Acta,* vol. 28, no. 2, pp. 91-101, 1989.

[34] J. L. McWhirter, "The stability of planar Couette flow simulated by molecular dynamics," *The Journal of Chemical Physics,* vol. 118, no. 6, pp. 2824-2836, 2003.

[35] B. V. Raghavan and M. Ostoja-Starzewski, "Shear-thinning of molecular fluids in Couette flow," *Physics of Fluids,* vol. 29, no. 2, p. 023103, 2017.

[36] K. Kadau, T. C. Germann, N. G. Hadjiconstantinou, P. S. Lomdahl, G. Dimonte, B. L. Holian and B. J. Alder, "Nanohydrodynamics simulations: an atomistic view of the Rayleigh–Taylor instability," *Proceedings of the National Academy of Sciences,* vol. 101, no. 16, pp. 5851-5855, 2004.

[37] E. R. Smith, "A molecular dynamics simulation of the turbulent Couette minimal flow unit," *Physics of Fluids,* vol. 27, no. 11, p. 115105, 2015.

[38] R. Cerbino, Y. Sun, A. Donev and A. Vailati, "Dynamic scaling for the growth of non-equilibrium fluctuations during thermophoretic diffusion in microgravity," *Scientific Reports,* vol. 5, p. 14486, 2015.

[39] D. J. Evans, E. G. D. Cohen and G. P. Morriss, "Probability of second law violations in shearing steady states," *Physical Review Letters,* vol. 71, no. 15, p. 2401, 1993.

[40] D. J. Evans and D. J. Searles, "The fluctuation theorem," *Advances in Physics,* vol. 51, no. 7, pp. 1529-1585, 2002.

[41] O. Gonzalez and A. M. Stuart, *A First Course in Continuum Mechanics*, Cambridge University Press, 2008.

[42] H. Ziegler and C. Wehrli, "The derivation of constitutive relations from the free energy and the dissipation function," in *Advances in Applied Mechanics*, vol. 25, Elsevier, 1987, pp. 183-238.

[43] B. V. Raghavan, P. Karimi and M. Ostoja-Starzewski, "Stochastic characteristics and Second Law violations of atomic fluids in Couette flow," *Physica A: Statistical Mechanics and its Applications,* vol. 496, pp. 90-107, 2018.

[44] M. Ostoja-Starzewski and A. Malyarenko, "Continuum mechanics beyond the second law of thermodynamics," *Proceedings of the Royal Society A: Mathematical, Physical and Engineering Sciences,* vol. 470, no. 2171, p. 20140531, 2014.

[45] M. Ostoja-Starzewski and B. V. Raghavan, "Continuum mechanics versus violations of the second law of thermodynamics," *Journal of Thermal Stresses,* vol. 39, no. 6, pp. 734-749, 2016.

[46] D. M. Carberry, J. C. Reid, G. M. Wang, E. M. Sevick, D. J. Searles and D. J. Evans, "Fluctuations and irreversibility: An experimental demonstration of a second-law-like theorem using a colloidal particle held in an optical trap," *Physical Review Letters,* vol. 92, no. 14, p. 140601, 2004.

[47] G. M. Wang, E. M. Sevick, E. Mittag, D. J. Searles and D. J. Evans, "Experimental demonstration of violations of the second law of thermodynamics for small systems and short time scales," *Physical Review Letters,* vol. 89, no. 5, p. 050601, 2002.

[48] B. D. Todd and P. J. Daivis, "Homogeneous non-equilibrium molecular dynamics simulations of viscous flow: techniques and applications," *Molecular Simulation,* vol. 33, no. 3, pp. 189-229, 2007.

[49] W. G. Hoover, D. J. Evans, R. B. Hickman, A. J. C. Ladd, W. T. Ashurst and B. Moran, "Lennard-Jones triple-point bulk and shear viscosities. Green-Kubo theory, Hamiltonian mechanics, and nonequilibrium molecular dynamics," *Physical Review A,* vol. 22, no. 4, p. 1690, 1980.

[50] D. J. Evans and G. P. Morriss, "Nonlinear-response theory for steady planar Couette flow," *Physical Review A,* vol. 30, no. 3, p. 1528, 1984.

[51] D. J. Evans and O. P. Morriss, "Non-Newtonian molecular dynamics," *Computer Physics Reports,* vol. 1, no. 6, pp. 297-343, 1984.

[52] A. J. C. Ladd, "Equations of motion for non-equilibrium molecular dynamics simulations of viscous flow in molecular fluids," *Molecular Physics,* vol. 53, no. 2, pp. 459-463, 1984.

[53] S. Plimpton, "Fast parallel algorithms for short-range molecular dynamics," *Journal of Computational Physics,* vol. 117, no. 1, pp. 1-19, 1995.

[54] B. D. Todd and P. J. Daivis, Nonequilibrium molecular dynamics: theory, algorithms and applications, *Cambridge University Press*, 2017.

[55] J. W. Dufty, A. Santos, J. J. Brey and R. F. Rodriguez, "Model for nonequilibrium computer simulation methods," *Physical Review A,* vol. 33, no. 1, p. 459, 1986.

[56] R. Zwanzig, "Nonlinear shear viscosity of a gas," *The Journal of Chemical Physics,* vol. 71, no. 11, pp. 4416-4420, 1979.

[57] C. H. Kruger and W. G. Vincenti, *Introduction to Physical Gas Dynamics*, John Wlley & Sons, 1965.

[58] D. L. Morris, L. Hannon and A. L. Garcia, "Slip length in a dilute gas," *Physical Review A,* vol. 46, no. 8, p. 5279, 1992.

[59] S. K. Prabha, P. D. Sreehari, M. Gopal M and S. P. Sathian, "The effect of system boundaries on the mean free path for confined gases," *AIP Advances*, vol. 3, no. 10, p. 102107, 2013.

[60] W. T. Ashurst and W. G. Hoover, "Argon shear viscosity via a Lennard-Jones potential with equilibrium and nonequilibrium molecular dynamics," *Physical Review Letters,* vol. 31, no. 4, p. 206, 1973.

[61] I. Borzsak, P. T. Cummings and D. J. Evans, "Shear viscosity of a simple fluid over a wide range of strain rates," *Molecular Physics,* vol. 100, no. 16, pp. 2735-2738, 2002.

[62] G. P. Morriss and D. J. Evans, "Application of transient correlation functions to shear flow far from equilibrium," *Physical Review A,* vol. 35, no. 2, p. 792, 1987.

[63] M. Ostoja-Starzewski, "Continuum Physics with Violations of the Second Law of Thermodynamics," in *Mathematical Modelling in Solid Mechanics*, Springer, 2017, pp. 181-192.

[64] S. Adhikari, "Matrix variate distributions for probabilistic structural dynamics," *AIAA Journal,* vol. 45, no. 7, pp. 1748-1762, 2007.

[65] C. Courtney, B. Drinkwater, S. Neild and P. Wilcox, "Global crack detection using bispectral analysis," in *9th European NDT Conference ECNDT*, 2006.

[66] A. J. Hillis, S. A. Neild, B. W. Drinkwater and P. D. Wilcox, "Global crack detection using bispectral analysis," *Proceedings of the Royal Society A: Mathematical, Physical and Engineering Sciences,* vol. 462, no. 2069, pp. 1515-1530, 2006.

[67] I. Elishakoff, *Probabilistic Theory of Structures*, Courier Corporation, 1999.

[68] H. Ziegler, *An Introduction to Thermomechanics*, vol. 21, Elsevier, 2012.

[69] P. J. Schmid, D. S. Henningson and D. F. Jankowski, *Stability and transition in shear flows. Applied Mathematical Sciences, Vol. 142*, American Society of Mechanical Engineers Digital Collection, 2002.

[70] H.-S. Dou and B. C. Khoo, "Investigation of turbulent transition in plane Couette flows using energy gradient method," *Advances in applied mathematics and mechanics,* vol. 3, no. 2, pp. 165-180, 2011.

[71] X. Du and M. Ostoja-Starzewski, "On the size of representative volume element for Darcy law in random media," *Proceedings of the Royal Society A: Mathematical, Physical and Engineering Sciences,* vol. 462, no. 2074, pp. 2949-2963, 2006.

[72] A. C. Eringen, *Microcontinuum field theories: II*. Fluent media, vol. 2, Springer Science & Business Media, 2001.

[73] K. P. Travis and D. J. Evans, "Molecular spin in a fluid undergoing Poiseuille flow," *Physical Review E,* vol. 55, no. 2, p. 1566, 1997.

[74] V. Garzó and A. Santos, Kinetic theory of gases in shear flows: nonlinear transport, vol. 131, *Springer Science & Business Media*, 2013.